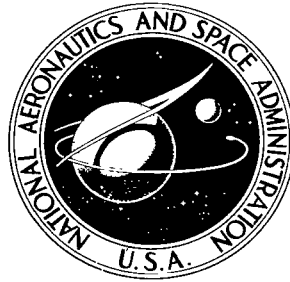


NASA TECHNICAL
REPORT



NASA TR R-331

e. 1

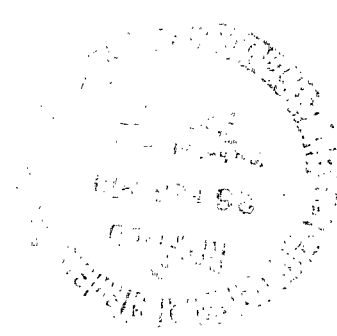
NASA TR R-331



LOAN COPY: RETURN TO
AFWL (WLOL)
KIRTLAND AFB, N MEX

RADIATION FROM SLOTS
ON CYLINDRICAL BODIES USING
GEOMETRICAL THEORY OF DIFFRACTION
AND CREEPING WAVE THEORY

by Constantine A. Balanis
Langley Research Center
Langley Station, Hampton, Va.





0068392

1. Report No. NASA TR R-331	2. Government Accession No.	3. Recipient's Catalog No.	
4. Title and Subtitle RADIATION FROM SLOTS ON CYLINDRICAL BODIES USING GEOMETRICAL THEORY OF DIFFRACTION AND CREEPING WAVE THEORY		5. Report Date February 1970	6. Performing Organization Code
7. Author(s) Constantine A. Balanis		8. Performing Organization Report No. L-6604	10. Work Unit No. 125-21-04-01-23
9. Performing Organization Name and Address NASA Langley Research Center Hampton, Va. 23365		11. Contract or Grant No.	13. Type of Report and Period Covered Technical Report
12. Sponsoring Agency Name and Address National Aeronautics and Space Administration Washington, D.C. 20546		14. Sponsoring Agency Code	
15. Supplementary Notes The material presented herein was offered as a dissertation in partial fulfillment of the requirements for the Degree of Doctor of Philosophy, The Ohio State University, Columbus, Ohio, June 1969.			
16. Abstract A hybrid solution employing wedge diffraction and creeping wave theories is used to compute the radiation patterns of axial and circumferential slots in the principal planes (equatorial and elevation) on conducting cylinders of finite and infinite lengths. The slots are excited by parallel-plate waveguides operating in the TEM and TE ₁₀ modes. For the equatorial-plane pattern, the total field in the lit region is obtained by the superposition of two fields, that is, the wedge-diffracted and the creeping-wave fields. The wedge-diffracted field is obtained by approximating the parallel-plate-cylinder geometry with two wedges, each formed by a wall of the waveguide and a tangent plane to the cylinder surface at the edge point. The creeping-wave contribution is obtained by the use of diffraction and propagation coefficients of waves traveling around conducting curved surfaces. The total field in the shadow region is obtained solely from the creeping-wave contribution. For the elevation-plane pattern, wedge diffraction techniques for the entire pattern are employed. The main advantages of the present technique are that it can be applied to geometries where modal solutions are not possible, in numerical ranges where the convergence properties of modal expansions are relatively poor, in parametric design problems since the contribution from each field is separated, and in the analysis of antennas with finite physical sizes.			
17. Key Words Suggested by Author(s) Diffraction Creeping waves Slot antennas		18. Distribution Statement Unclassified - Unlimited	
19. Security Classif. (of this report) Unclassified	20. Security Classif. (of this page) Unclassified	21. No. of Pages 77	22. Price* \$3.00

*For sale by the Clearinghouse for Federal Scientific and Technical Information
Springfield, Virginia 22151

RADIATION FROM SLOTS ON CYLINDRICAL BODIES
USING GEOMETRICAL THEORY OF DIFFRACTION
AND CREEPING WAVE THEORY*

By Constantine A. Balanis
Langley Research Center

SUMMARY

A hybrid solution employing wedge diffraction and creeping wave theories is used to compute the radiation patterns of axial and circumferential slots in the principal planes (equatorial and elevation) on conducting cylinders of finite and infinite lengths. The slots are excited by parallel-plate waveguides operating in the TEM and TE_{10} modes.

For the equatorial-plane pattern, the total field in the lit region is obtained by the superposition of two fields, that is, the wedge-diffracted and the creeping-wave fields. The wedge-diffracted field is obtained by approximating the parallel-plate—cylinder geometry with two wedges, each formed by a wall of the waveguide and a tangent plane to the cylinder surface at the edge point. The creeping-wave contribution is obtained by the use of diffraction and propagation coefficients of waves traveling around conducting curved surfaces. The total field in the shadow region is obtained solely from the creeping-wave contribution. For the elevation-plane pattern, wedge diffraction techniques for the entire pattern are employed.

The method is checked computationally by comparison with the modal solutions for axial and circumferential slots on right circular cylinders and experimentally for elliptical cylinders since modal solutions are not readily available. Experimental models are also used for the verification of the elevation plane pattern computations since boundary-value solutions are not available for finite length cylinders.

Computed results using this technique compare favorably with those obtained from existing modal expansion boundary-value solutions and experimental results. The main advantages of the present technique are that it can be applied to geometries where modal solutions are not possible, in numerical ranges where the convergence properties of modal expansions are relatively poor, in parametric design problems since the contribution from each field is separated, and in the analysis of antennas with finite physical sizes.

*The material presented herein was offered as a dissertation in partial fulfillment of the requirements for the Degree of Doctor of Philosophy, The Ohio State University, Columbus, Ohio, June 1969.

INTRODUCTION

Since the geometrical theory of diffraction has been introduced, it has been employed successfully in the solution of various types of diffraction problems. Previous work in applying the wedge diffraction and creeping wave theories, each one individually, to scattering and radiation antenna problems is discussed. No one has attempted a hybrid solution with both wedge diffraction and creeping wave theories used for the same scatterer. The work presented in this report is an attempt to formulate a hybrid solution employing both wedge diffraction and creeping wave theories on the same antenna. The antenna is a slotted, axially and circumferentially, conducting cylinder, with the slots being excited by parallel-plate waveguides operating in the TEM and TE_{10} modes.

The radiation properties of slot antennas on conducting cylinders have been studied extensively. (See refs. 1 to 5.) Such analyses have been restricted to geometries where modal expansion field functions are readily available and whose physical length is infinite. Moreover, the solutions obtained exhibit poor convergent properties for objects more than a few wavelengths in extent. However, many practical problems involve slot antennas mounted on finite-size conducting bodies whose geometrical shape does not conform to a coordinate system where the wave equation is separable. Wedge diffraction (refs. 6 to 9) and creeping wave theories are used in the analysis presented herein to compute the radiation patterns of axial and circumferential slots on conducting cylinders of finite and infinite lengths. The method employed is an extension of the geometrical theory of diffraction (refs. 10 and 11) and creeping wave theory (refs. 12 to 16).

The geometrical theory of diffraction and creeping wave theory are extensions of geometrical optics which account for diffraction. They introduce diffracted rays in addition to the usual rays of geometrical optics. These diffracted rays are produced by incident rays which hit edges, corners, vertices, or curved surfaces. Some of these diffracted rays enter the shadow regions and account for the field intensity there. The distribution of the incident energy among those diffracted rays is described by a diffraction coefficient. The diffraction of the incident rays is a local phenomenon, so the diffraction coefficient depends on the geometry of the edge or curved surface in the vicinity of the point of diffraction and on the polarization of the incident field.

A field is associated with each diffracted ray and the total field at a point is the sum of the fields of all rays at that point. The phase of the field on a ray is assumed to be proportional to the optical length of the ray from some reference point. Appropriate phase jumps must be added as a ray passes through a caustic (congruence of rays at a point or line). The amplitude is assumed to vary in accordance with the principle of conservation of energy in a narrow tube of rays. The initial value of the field on a diffracted ray is determined from the incident field with the aid of an appropriate diffraction

coefficient. These diffraction coefficients are determined from certain canonical problems.

The canonical problem, which yields the diffraction coefficient for an edge, is the diffraction of a linearly polarized plane wave by a two-dimensional, infinite wedge. The diffraction coefficient is found from Sommerfeld's asymptotic, high frequency solution to this problem. (See ref. 17.) Pauli (ref. 18) has obtained a practical formulation for the diffraction coefficient and Hutchins (ref. 19) has generalized it. He has obtained a series solution which is valid for the exterior and interior regions of a wedge. In addition, his solution is accurate for wedges of large included angles whereas the Pauli solution is not accurate. Oberhettinger (ref. 20) has obtained a similar series in which the leading term is identical to the Fresnel integral form for half-plane diffraction. The work of Hutchins tends to bridge the solutions of Pauli and Oberhettinger.

The primary task in applying the creeping wave theory is the determination of the diffraction, attenuation, and ray-path factors for a general body (and it is not yet always practical). Thus, it is necessary to evaluate these factors for canonical targets whose exact solutions are available, such as the cylinder and sphere. (See refs. 12 to 16 and 21 to 23.) In order to obtain a more general solution for these factors it is convenient to utilize experimental data to validate an empirical model for more general targets such as the prolate spheroid (refs. 24 to 26).

The attenuation and diffraction coefficients for a cylinder have been obtained by comparing the asymptotic series of the scattering boundary-value solution with that of the diffraction problem formulation (refs. 13 to 16). The ray paths along the surface of the cylinder are geodesics (great circles). The scattering by a sphere is, however, a most important problem. The classical solution of Mie using separation of variables and series techniques can be considered as the starting point. Senior and Goodrich (ref. 21) have obtained an asymptotic form to the Mie series solution for the sphere through the application of the Watson transformation. Hong (ref. 22) has derived attenuation and diffraction coefficients with higher-order correction terms. The formidable task of implementing this solution numerically has yet to be accomplished.

An approach to the general formulation of the creeping-wave paths on bodies of revolution has been developed by Kinber (ref. 27). Kinber has shown that the wave equation may be expanded in a set of ray coordinates in which the solution can be written in a form whose magnitude is dependent upon the cross section of the ray tube and whose phase is dependent only upon the propagation constant and path length traversed.

The empirical approach utilizes a simplified ray-path geometry to determine approximate attenuation and diffraction coefficients for a sphere. (See refs. 24 to 26.) This approach is of interest in that it lends itself for extension to more general targets,

and is a simplified creeping wave analysis. It uses a single nonconvergent (and non-divergent) ray path together with approximate diffraction and attenuation coefficients to construct an approximate solution for the scattered field due to creeping waves propagating in each direction along the ray path. The path chosen is the path traversed by the "major" ray (that is, the path corresponding to the E-plane of the sphere). This analysis suggests that an approximate picture of scattering by a sphere can be constructed by neglecting the creeping waves which have a radial magnetic field (that is, the "minor" creeping waves) and by considering only the creeping waves which have a radial electric field (that is, the "major" creeping waves) except for the H-plane scattered fields.

The prolate spheroid represents a body for which an exact closed-form solution is not available except on the axis of rotation. In order to find the ray-path geometries of the prolate spheroid for an arbitrary angle of incidence, the geodesic corresponding to the point of attachment and the tangent direction at that point must be calculated. The determination of the tangent direction of the creeping wave at the shadow boundary is not an easy task in general. It is therefore suggested that the simplified ray-path geometry (refs. 24 to 26) for the sphere can be applied to the prolate spheroid. In this case, the creeping-wave paths are elliptical; thus, the total attenuation must be expressed as an integral which is dependent upon the radius of curvature along the path. Also the radius of curvature at the points of attachment and reradiation must be computed in order to determine the diffraction coefficient. The specific solution for the prolate spheroid has been presented by Ryan (refs. 24 and 26) and Peters and Ryan (ref. 25).

Many other antenna problems have been treated using wedge diffraction techniques. Russo, Rudduck, and Peters (ref. 28) applied the geometrical theory of diffraction to calculate the total antenna pattern of a horn in the E-plane, including the backlobe region. Because the theoretical and experimental patterns are in excellent agreement, the method for treating diffraction by edges is valid. Obha (ref. 29) used the geometrical method of diffraction to calculate the radiation pattern and gain of a finite width corner reflector antenna. This method also yields good results for the computation of backscattering from an antenna having conducting plates finite in extent.

Extensive work of applying the wedge diffraction method to waveguides has been carried out by Rudduck and coworkers (refs. 6 to 9). The principal tool employed is diffraction by a conducting wedge; the resulting electromagnetic field may be treated as a superposition of the geometrical optics field and the diffracted field which behaves as a cylindrical wave radiating from the edge of the wedges. These techniques may be applied to any two-dimensional antenna or scattering body which may be constructed from a set of wedges; the radiation or scattering pattern may be obtained for any excitation which can be expressed in terms of plane or cylindrical waves by superposition of

the individual wedge diffractions. Some elementary examples include parallel-plate waveguides, walls of finite thickness, and polygonal cylinders.

A basic feature of this technique is that it does not require an assumption of the value of the total field or current on some surface, as do conventional methods of aperture integration which employ the approximation of physical optics. This feature thus allows more accurate treatment of problems than ordinarily obtained by approximate methods; it also provides knowledge of the fields in terms of the incident field, which results in the ability to analytically determine admittance and gain of antennas (ref. 6), radiation patterns (refs. 7 and 8), mutual coupling (refs. 30 and 31), and reflection coefficient (refs. 32 to 34).

The geometrical ray techniques of this method provide conceptual simplicity with which solutions may be formulated. This, together with superposition of wedges, allows structural aspects to be taken into account; for example, antennas mounted with and without ground planes, structures with thin or thick walls, and arbitrary waveguide truncations can be treated. In addition, the fields in all space can be determined; thus, back-lobe regions can be treated.

The essential feature of this approach is that it is applicable to all types of complicated problems, some of which are not tractable. The approach is to resolve a complicated problem into simpler ones, each of which will have a relatively simple solution. The basic building blocks will be rigorous solutions to such canonical diffraction problems as the wedge, cylinder, and sphere, which can be put together to solve more complicated problems.

The work outlined in this hybrid solution is for general conducting cylinders of arbitrary convex cross section. However, computations are restricted to circular cylinders for which boundary-value solutions exist for comparison and elliptical cylinders for which models and experimental data are available for comparison. The radiation patterns of interest for each case are the principal-plane patterns, equatorial plane and elevation plane in the usual spherical coordinate system.

The equatorial-plane pattern is obtained by the superposition of diffracted fields from a set of wedges and creeping-wave fields propagating around the surface of the cylinder. The set of wedges approximate the parallel-plate—cylinder geometry in the vicinity of the discontinuity formed by the waveguide and the cylinder. Each wedge is formed by a wall of the parallel-plate waveguide and the tangent plane to the cylinder surface at the edge point.

For the equatorial-plane pattern, two distinct regions can be identified: the lit and shadow regions. The shadow region encompasses the space occupied by the set of wedges and cylinder surface and the lit region the remaining space. The total field in

the lit region is obtained by the superposition of two fields – that is, the wedge-diffracted and creeping-wave fields. The total field in the shadow region is obtained solely from the creeping-wave contribution. For the elevation-plane pattern, wedge diffraction techniques for the entire pattern are employed.

The most interesting part of this hybrid solution is the coupling mechanism between the wedge-diffracted and creeping-wave fields. Creeping waves are launched by the tip of the wedges in a direction tangent to the cylinder surface at the edge point. Since the field must be continuous along the line separating the lit and shadow regions, the wedge-diffracted fields along the surface of each wedge will be used as the initial value of the creeping waves to preserve the continuity of the fields. The creeping waves continually radiate energy in a tangential direction as they propagate around the cylinder surface until they reach the opposite wall of the slot and again illuminate the wedges; this is a second-order field contribution and it is neglected. The loss of energy due to reradiation is accounted for by the use of an attenuation factor.

The method is checked computationally by comparison with the modal solutions for axial and circumferential slots on right circular cylinders and experimentally for elliptical cylinders since modal solutions are not readily available. Experimental models are used for the verification of the elevation-plane-pattern computations since boundary-value solutions are not available for finite-length cylinders.

Computed results from this technique compare favorably with those obtained from existing modal expansion boundary-value solutions and experimental results. The main advantages of the present technique are that it can be applied (1) to geometries where modal solutions are not possible, (2) in numerical ranges where the convergence properties of modal expansions are relatively poor, (3) in parametric design problems since the contribution from each field is separated, and (4) in the analysis of antennas with finite physical sizes.

SYMBOLS

No attempt has been made to define all the symbols used in this report in a single list; most symbols used in this analysis are defined by diagrams for the various geometries. The following symbols are used as main symbols with appropriate subscripts throughout the analysis:

D diffraction coefficient

E electromagnetic field

E_C	creeping-wave field
E_D	wedge-diffracted field
E_G	geometrical optics field
E_T	total field
R_D	diffracted ray
R_{RFL}	reflected ray
α	attenuation constant
k	phase constant
WA	wedge angle

Numerical subscripts indicate particular wedge.

Superscripts within parentheses indicate order of diffraction.

WEDGE DIFFRACTION

Wedge diffraction techniques are applied for the analysis of the radiation pattern of the parallel-plate waveguide shown in figure 1. This geometry has been treated by using the wedge diffraction concepts by Rudduck and his coworkers (refs. 6 to 9). Their solution is incorporated in the slotted-cylinder radiation-pattern analysis and is outlined in this section. A single-diffracted wave emanates from each wedge that is illuminated by an incident plane wave. The single-diffracted waves produced by one wedge illuminate the other with double-diffracted fields being produced. This process continues to higher orders of diffraction.

Single Diffraction

The principal method employed in the analysis of a parallel-plate waveguide is diffraction by a conducting wedge. The diffraction of a plane wave by a wedge was solved by Sommerfeld (ref. 17). Pauli (ref. 18) obtained a practical formulation of the solution for a finite angle conducting wedge which was later improved by Hutchins (ref. 19). (See the appendix.) The total electromagnetic field from the wedge may be treated as the

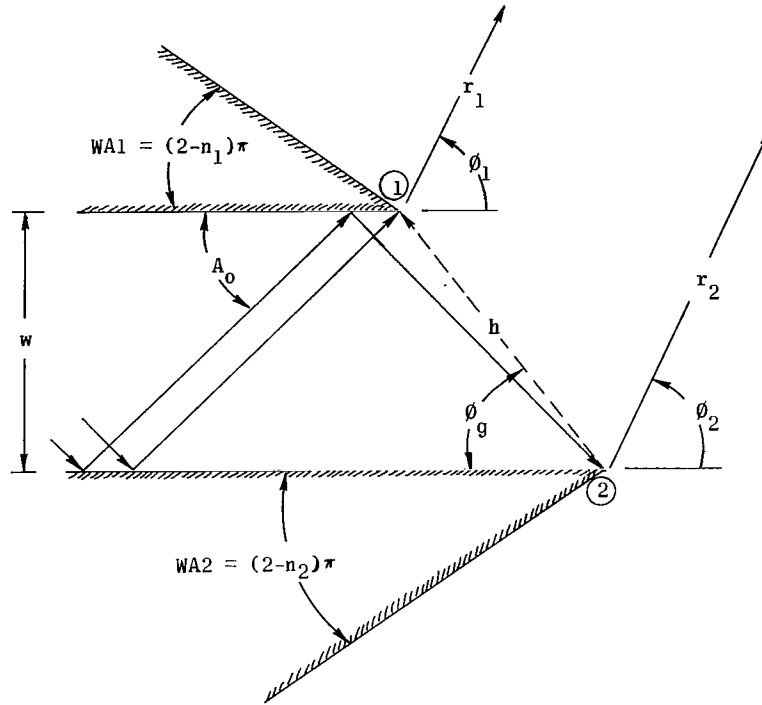


Figure 1.- Geometry of a parallel-plate waveguide aperture.

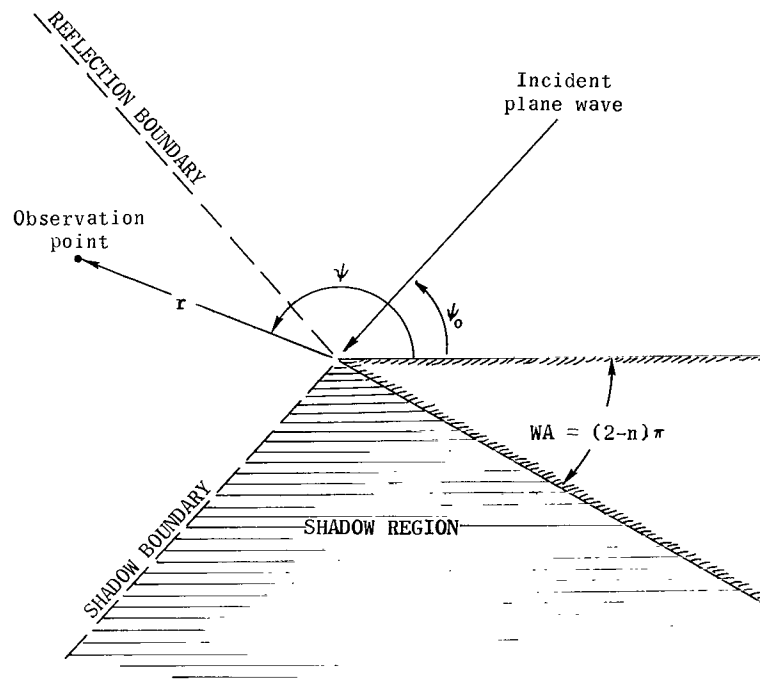


Figure 2.- Geometry for plane wave wedge diffraction with geometrical optics region.

superposition of the geometrical optics and the diffracted fields which behave as cylindrical waves radiating from the edge of the wedges.

The diffraction of a plane wave by a wedge is shown in figure 2. The solution to the plane-wave diffraction problem may be expressed in terms of scalar functions that represent the normal and parallel polarization components of the electromagnetic field to the plane of study in figure 2. The total field is defined as

$$\mathbf{E} = \mathbf{E}_G + \mathbf{E}_D \quad (1)$$

where \mathbf{E}_G is the geometrical optics field and \mathbf{E}_D is the diffracted field. The diffracted field is given by

$$\mathbf{E}_D = V_B(\mathbf{r}, \psi - \psi_0, n) \pm V_B(\mathbf{r}, \psi + \psi_0, n) \quad (2)$$

where the parameters r , ψ , ψ_0 , n are shown in figure 2 and $V_B(\mathbf{r}, \psi \pm \psi_0, n)$ is the diffraction function as defined in the appendix. The plus sign applies for the polarization of the electric field normal to the edge

$$\left(\frac{\partial \mathbf{E}}{\partial n} \right)_{\text{wedge}} = 0 \quad (3)$$

where n is the unit normal to the edge of the wedge. The minus sign applies for the polarization parallel to the edge

$$E_{\text{wedge}} = 0 \quad (4)$$

The geometrical optics field is defined in three regions. (See fig. 2.) For plane-wave incidence, the geometrical optics field is

$$\begin{aligned} \text{Geometrical optics field} &= \text{Incident geometrical field} \pm \text{Reflected geometrical field} && \text{(Regions)} \\ \mathbf{E}_G &= e^{jkr} \cos(\psi - \psi_0) && (\pi - \psi_0 < \psi < \pi + \psi_0) \end{aligned} \quad (5)$$

$$\mathbf{E}_G = e^{jkr} \cos(\psi - \psi_0) \pm e^{jkr} \cos(\psi + \psi_0) \quad (0 < \psi < \pi - \psi_0) \quad (6)$$

$$\mathbf{E}_G = 0 \quad (\pi + \psi_0 < \psi) \quad (7)$$

The time dependence $e^{j\omega t}$ is used throughout this analysis.

The diffracted wave E_D may be represented as a cylindrical wave radiating from the edge. (See the appendix.) In fact, at large distances from the edge and in regions removed from shadow boundaries, E_D has the radial dependence e^{-jkr}/\sqrt{r} . Because of this cylindrical nature, subsequent diffractions of a diffracted wave may be treated as the diffraction of a cylindrical wave by a wedge.

Diffraction by Pair of Wedges

The process of diffraction by a pair of wedges (parallel-plate waveguide) is now outlined. Two polarizations which must be distinguished are those corresponding to the TEM and TE_{10} waveguide modes shown in figure 3. In the TEM mode, the incident plane

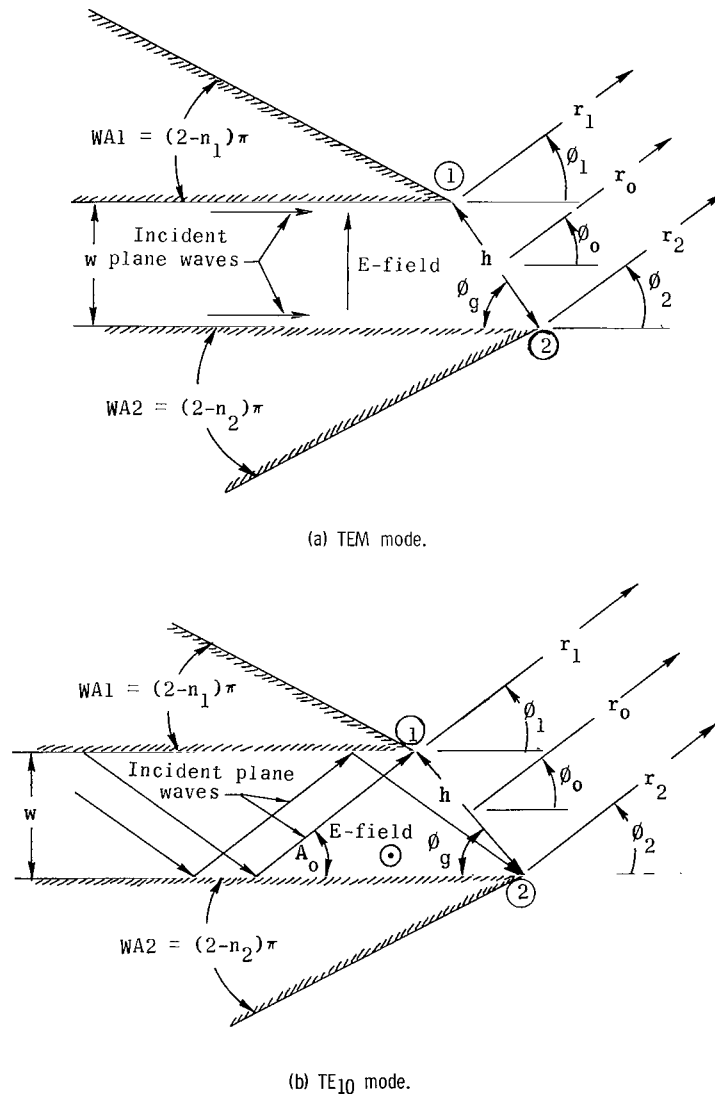


Figure 3.- TEM and TE_{10} modes in a parallel-plate waveguide aperture.

wave is parallel to the axis of the guide having a polarization perpendicular to the edge of each wedge. The TE_{10} waveguide mode may be represented by two TEM waves which reflect obliquely back and forth between the waveguide walls. (See ref. 35.) Thus, in the TE_{10} mode the incident plane waves have a polarization parallel to the edge of the wedges.

TEM mode.- In the TEM mode an incident plane wave propagates parallel to the axis of the guide walls as shown in figure 3(a). The far-zone singly diffracted fields from wedges 1 and 2 are given by

$$E_{D1}^{(1)}(r_1, \phi_1) = \frac{E_1 e^{-j\left(kr_1 + \frac{\pi}{4}\right)}}{\sqrt{2\pi kr_1}} \frac{\frac{1}{n_1} \sin \frac{\pi}{n_1}}{\cos \frac{\pi}{n_1} - \cos \frac{\pi + \phi_1}{n_1}} \quad (8)$$

$$E_{D2}^{(1)}(r_2, \phi_2) = \frac{E_2 e^{-j\left(kr_2 + \frac{\pi}{4}\right)}}{\sqrt{2\pi kr_2}} \frac{\frac{1}{n_2} \sin \frac{\pi}{n_2}}{\cos \frac{\pi}{n_2} - \cos \frac{\pi - \phi_2}{n_2}} \quad (9)$$

The superscripts denote the order of diffraction. If the phase of the incident waves with respect to edge ① is expressed as

$$E_1 = E = 1 \quad (10)$$

and

$$E_2 = E e^{-jkw \cot \phi_g} = e^{-jkw \cot \phi_g} \quad (11)$$

then equations (8) and (9) reduce to

$$E_{D1}^{(1)}(r_1, \phi_1) = \frac{e^{-j\left(kr_1 + \frac{\pi}{4}\right)}}{\sqrt{2\pi kr_1}} R_{D1}^{(1)}(\phi_1) \quad (12)$$

$$E_{D2}^{(1)}(r_2, \phi_2) = \frac{e^{-j\left(kr_2 + \frac{\pi}{4}\right)}}{\sqrt{2\pi kr_2}} R_{D2}^{(1)}(\phi_2) \quad (13)$$

where $R_{D1}^{(1)}(\phi_1)$ and $R_{D2}^{(1)}(\phi_2)$, the singly diffracted rays from wedges 1 and 2, are given by

$$R_{D1}^{(1)}(\phi_1) = \frac{\frac{1}{n_1} \sin \frac{\pi}{n_1}}{\cos \frac{\pi}{n_1} - \cos \frac{\pi + \phi_1}{n_1}} \quad (14)$$

$$R_{D2}^{(1)}(\phi_2) = \frac{e^{-jkw \cot \phi_g} \frac{1}{n_2} \sin \frac{\pi}{n_2}}{\cos \frac{\pi}{n_2} - \cos \frac{\pi - \phi_2}{n_2}} \quad (15)$$

Applying the far-field approximations

$$\left. \begin{aligned} r_1 &\approx r_o + \frac{h}{2} \cos(\phi_o + \phi_g) \\ r_2 &\approx r_o - \frac{h}{2} \cos(\phi_o + \phi_g) \end{aligned} \right\} \quad (16)$$

for phase terms and

$$r_1 \approx r_2 \approx r_o \quad (17)$$

for amplitude terms with

$$\phi_1 \approx \phi_2 \approx \phi_o \quad (18)$$

gives

$$E_{D1}^{(1)}(r_o, \phi_o) = \frac{e^{-j \left\{ k \left[r_o + \frac{h}{2} \cos(\phi_o + \phi_g) \right] + \frac{\pi}{4} \right\}}}{\sqrt{2\pi k r_o}} R_{D1}^{(1)}(\phi_o) \quad (19)$$

and

$$E_{D2}^{(1)}(r_o, \phi_o) = e^{-j \left\{ k \left[r_o + \frac{h}{2} \cos(\phi_o + \phi_g) \right] + \frac{\pi}{4} \right\}} \frac{R_{D2}^{(1)}(\phi_o) e^{jkh \cos(\phi_o + \phi_g)}}{\sqrt{2\pi k r_o}} \quad (20)$$

The singly diffracted rays may again be diffracted to produce doubly diffracted rays and so on to higher orders of diffraction as shown in figure 4. The singly diffracted ray $R_{D1}^{(1)}$ illuminating edge ② gives rise to the doubly diffracted ray $R_{D2}^{(2)}$; $R_{D2}^{(1)}$ causes $R_{D1}^{(2)}$ in a similar manner. Also, some of the singly diffracted rays from edge ① are reflected

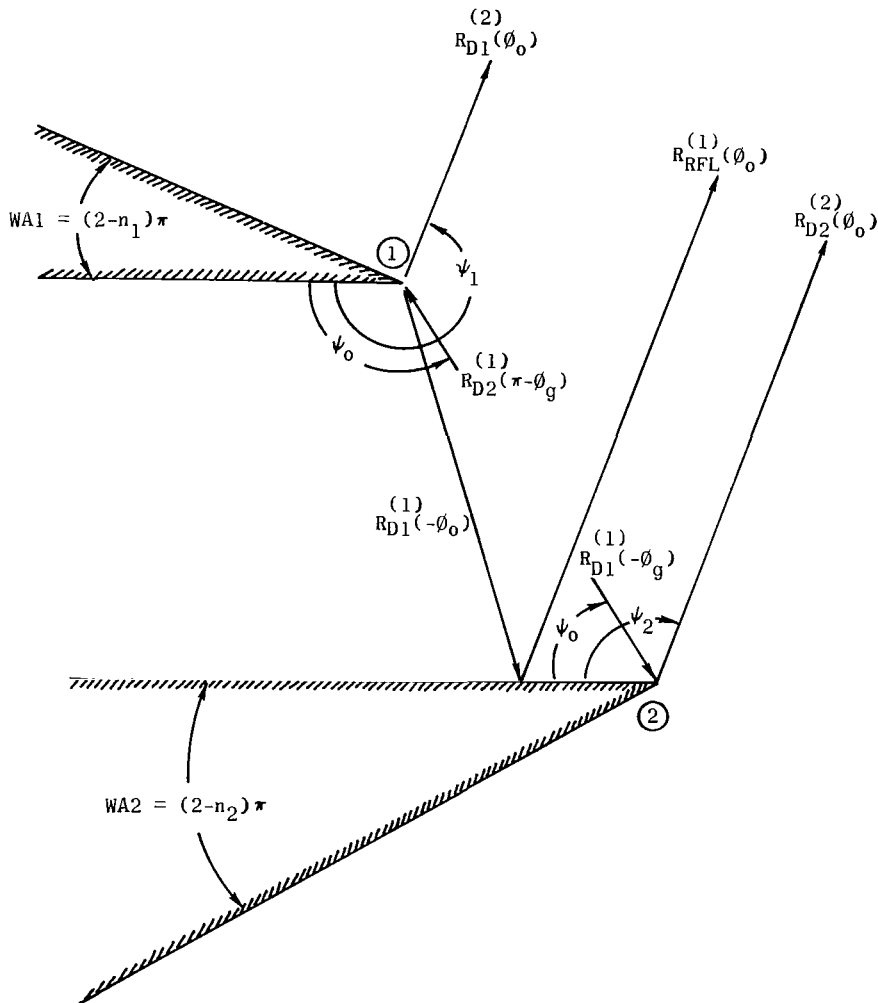


Figure 4.- Doubly diffracted and reflected rays of a general parallel-plate waveguide.

from wedge 2 and appear to radiate from the image of edge ①; these reflected rays are given as

$$R_{\text{RFL}}^{(1)}(\phi_o) = R_{\text{D1}}^{(1)}(-\phi_o) \quad \left(\phi_g < \phi_o < \frac{\pi}{2}\right) \quad (21)$$

The doubly diffracted ray from edge ② is expressed as

$$R_{\text{D2}}^{(2)}(\phi_o) = R_{\text{D1G}}^{(1)} \left[V_{\text{B}}(h, \pi - \phi_o - \phi_g, n_2) + V_{\text{B}}(h, \pi - \phi_o + \phi_g, n_2) \right] \quad (22)$$

where

$$R_{\text{D1G}}^{(1)} = R_{\text{D1}}^{(1)}(-\phi_g) \quad (23)$$

and from edge ① as

$$R_{\text{D1}}^{(2)}(\phi_o) = R_{\text{D2G}}^{(1)} \left[V_{\text{B}}(h, \phi_o + \phi_g, n_1) + V_{\text{B}}(h, 2\pi + \phi_o - \phi_g, n_1) \right] \quad (24)$$

where

$$R_{\text{D2G}}^{(1)} = R_{\text{D2}}^{(1)}(\pi - \phi_g) \quad (25)$$

An additional doubly diffracted ray by edge ① from the image source is given by

$$R_{\text{D1R}}^{(2)}(\phi_o) = R_{\text{D1P}}^{(1)} \left[V_{\text{B}}\left(2w, \frac{\pi}{2} + \phi_o, n_1\right) + V_{\text{B}}\left(2w, \frac{3\pi}{2} + \phi_o, n_1\right) \right] \quad (26)$$

where

$$R_{\text{D1P}}^{(1)} = R_{\text{D1}}^{(1)}\left(-\frac{\pi}{2}\right) \quad (27)$$

The total diffracted rays from edges ① and ②, by using single-double diffractions, are expressed as

$$R_{\text{D1}}(\phi_o) = R_{\text{D1}}^{(1)}(\phi_o) + R_{\text{D1}}^{(2)}(\phi_o) + R_{\text{D1R}}^{(2)}(\phi_o) \quad (28)$$

$$R_{D2}(\phi_o) = R_{D2}^{(1)}(\phi_o) + R_{D2}^{(2)}(\phi_o) \quad (29)$$

and the reflected ray from wedge 2 as

$$R_{RFL}(\phi_o) = R_{D1}(-\phi_o) \quad (30)$$

The total diffracted field from the aperture may be expressed as the superposition of the total diffracted rays from edges ① and ② plus the total rays from the image source to yield

$$E_D(r_o, \phi_o) = \frac{e^{-j \left\{ k \left[r_o + \frac{h}{2} \cos(\phi_o + \phi_g) \right] + \frac{\pi}{4} \right\}}}{\sqrt{2\pi k r_o}} \left[R_{D1}(\phi_o) + R_{D2}(\phi_o) e^{j k h \cos(\phi_o + \phi_g)} + R_{D1}(-\phi_o) e^{-j 2 k w \sin \phi_o} \right] \quad (31)$$

Each term in equation (31) contributes to the radiation pattern only in certain regions as follows:

Ray	Region
$R_{D1}(\phi_o)$	$-\phi_g < \phi_o < \pi - \text{WA1}$
$R_{D2}(\phi_o)$	$\pi + \text{WA2} < \phi_o < \pi - \phi_g$
$R_{D1}(-\phi_o)$	$+\phi_g < \phi_o < \frac{\pi}{2}$

There are subsequent diffractions which result in third- and higher-order diffractions from edges ① and ②. The total higher-order diffractions (that is, second and higher order) can be put in a closed form. (See ref. 6.) The total illumination of edge ② from edge ① can be expressed as

$$R_{1G} = R_1(-\phi_g) \quad (32)$$

where $R_1(\phi_o)$ is the total diffracted ray from edge ①. Consequently, the total higher-order diffractions from edge ② are given by

$$R_{D2}^{(h)}(\phi_o) = R_{1G} \left[\bar{V}_B(h, \pi - \phi_o - \phi_g, n_2) + V_B(h, \pi - \phi_o + \phi_g, n_2) \right] \quad (33)$$

and the total ray by

$$R_2(\phi_o) = R_{D2}^{(1)}(\phi_o) + R_{D2}^{(h)}(\phi_o) \quad (34)$$

The total higher-order illumination of edge ① is given by

$$R_{2G} = R_2(\pi - \phi_g) \quad (35)$$

and

$$R_{1P} = R_1\left(-\frac{\pi}{2}\right) \quad (36)$$

Thus, the total higher-order diffractions from edge ① are given by

$$\begin{aligned} R_{D1}^{(h)}(\phi_o) &= R_{2G} \left[\bar{V}_B(h, \phi_o + \phi_g, n_1) + V_B(h, 2\pi + \phi_o - \phi_g, n_1) \right] \\ &+ R_{1P} \left[\bar{V}_B\left(2w, \frac{\pi}{2} + \phi_o, n_1\right) + V_B\left(2w, \frac{3\pi}{2} + \phi_o, n_1\right) \right] \end{aligned} \quad (37)$$

and the total diffractions by

$$R_1(\phi_o) = R_{D1}^{(1)}(\phi_o) + R_{D1}^{(h)}(\phi_o) \quad (38)$$

The total diffracted field from the aperture can be expressed as the superposition of the total diffracted rays from edges ① and ② plus the total reflected ray as given by equation (31) where $R_{D1}(\phi_o)$, $R_{D2}(\phi_o)$, and $R_{D1}(-\phi_o)$ are replaced by $R_1(\phi_o)$, $R_2(\phi_o)$, and $R_1(-\phi_o)$, respectively.

The total diffracted waves from edges ① and ② are given in terms of the unknown illuminating rays R_{1G} , R_{2G} , and R_{1P} . These rays can be determined by the solution of three simultaneous linear equations formed by expressing each unknown ray in terms of equation (34) or equation (38) and are given as follows:

$$R_{1G} = R_{D1G}^{(1)} + R_{2G} V_{2G}(-\phi_g) + R_{1P} V_{1P}(-\phi_g) \quad (39)$$

$$R_{1P} = R_{D1P}^{(1)} + R_{2G} V_{2G} \left(-\frac{\pi}{2}\right) + R_{1P} V_{1P} \left(-\frac{\pi}{2}\right) \quad (40)$$

$$R_{2G} = R_{D2G}^{(1)} + R_{1G} V_{1G} (\pi - \phi_g) \quad (41)$$

where the quantities V_{1G} , V_{1P} , and V_{2G} are the unit-wave diffractions used in equations (33) and (37).

TE₁₀ mode.- The diffraction at the aperture of the parallel-plate waveguide for the TE₁₀ mode may be treated in a similar manner as the TEM mode. The TE₁₀ mode may be represented by two plane waves reflecting obliquely back and forth between the waveguide walls at an angle

$$A_o = \sin^{-1} \frac{\lambda}{2w} \quad (42)$$

as shown in figure 3(b). The wave has a polarization parallel to the edges of the wedges which form the waveguide walls. For this mode two cases must be distinguished as follows:

Case I: $A_o > \phi_g$

Case II: $A_o \leq \phi_g$

For case I, edge ② is not illuminated by the incident plane wave and no singly diffracted ray emanates. For case II, both edges are illuminated by the incident wave; hence, singly diffracted rays emanate from both edges.

Since the polarization is parallel to the edges of the guide for the TE₁₀ mode, the negative sign in the diffraction formula is chosen. The singly diffracted ray from edge ① is obtained from equation (2) as

$$R_{D1}^{(1)}(\phi_o) = \frac{1}{n_1} \sin \frac{\pi}{n_1} \left(\frac{1}{\cos \frac{\pi}{n_1} - \cos \frac{\pi + \phi_o - A_o}{n_1}} - \frac{1}{\cos \frac{\pi}{n_1} - \cos \frac{\pi + \phi_o + A_o}{n_1}} \right) \quad (43)$$

For case II ($A_o \leq \phi_g$), the singly diffracted ray from edge ② is given by

$$R_{D2}^{(1)}(\phi_o) = -\frac{1}{n_2} \sin \frac{\pi}{n_2} e^{-jkw(\sin A_o + \cot \phi_g \cos A_o)} \left(\frac{1}{\cos \frac{\pi}{n_2} - \cos \frac{\pi - \phi_o - A_o}{n_2}} - \frac{1}{\cos \frac{\pi}{n_2} - \cos \frac{\pi - \phi_o + A_o}{n_2}} \right) \quad (44)$$

where the exponential factor and minus sign represent the phase of the incident plane wave at edge ①. The reflected rays are given by

$$R_{RFL}^{(1)}(\phi_o) = -R_{D1}^{(1)}(-\phi_o) \quad \left(\phi_g < \phi_o < \frac{\pi}{2} \right) \quad (45)$$

where the preceding minus sign results from the reflection.

Multiple diffractions occur in the same manner as for the TEM mode but with the minus sign chosen in equations (22), (24), (26), (33), and (37). Thus the total higher-order diffracted waves from edges ① and ② for the TE₁₀ mode are given by

$$\begin{aligned} R_{D1}^{(h)}(\phi_o) = & R_{2G} \left[V_B(h, \phi_o + \phi_g, n_1) - V_B(h, 2\pi + \phi_o - \phi_g, n_1) \right] \\ & - R_{1P} \left[V_B\left(2w, \frac{\pi}{2} + \phi_o, n_1\right) - V_B\left(2w, \frac{3\pi}{2} + \phi_o, n_1\right) \right] \end{aligned} \quad (46)$$

and

$$R_{D2}^{(h)}(\phi_o) = R_{1G} \left[V_B(h, \pi - \phi_o - \phi_g, n_2) - V_B(h, \pi - \phi_o + \phi_g, n_2) \right] \quad (47)$$

The minus sign preceding R_{1P} results in the same manner as for the reflected rays of equation (45). The total wave from each edge is obtained by using the TE₁₀ mode rays in the same equations valid for the TEM mode, that is, equations (34) and (38) to (41). The unknown illuminating rays are determined in the same manner as for the TEM mode by using the formulations for $R_{D1}^{(1)}$, $R_{D2}^{(1)}$, $R_{D1}^{(h)}$, and $R_{D2}^{(h)}$ given for the TE₁₀ mode.

CREEPING-WAVE DIFFRACTION CONCEPT

When a wave is incident upon an opaque object which is large compared to the wavelength, a shadow is formed. However, some radiation penetrates into the shadow region due to diffracted rays as shown in figure 5. (See refs. 12 to 16.) These rays are produced by incident rays which are tangent to the surface of the body. Each tangent ray

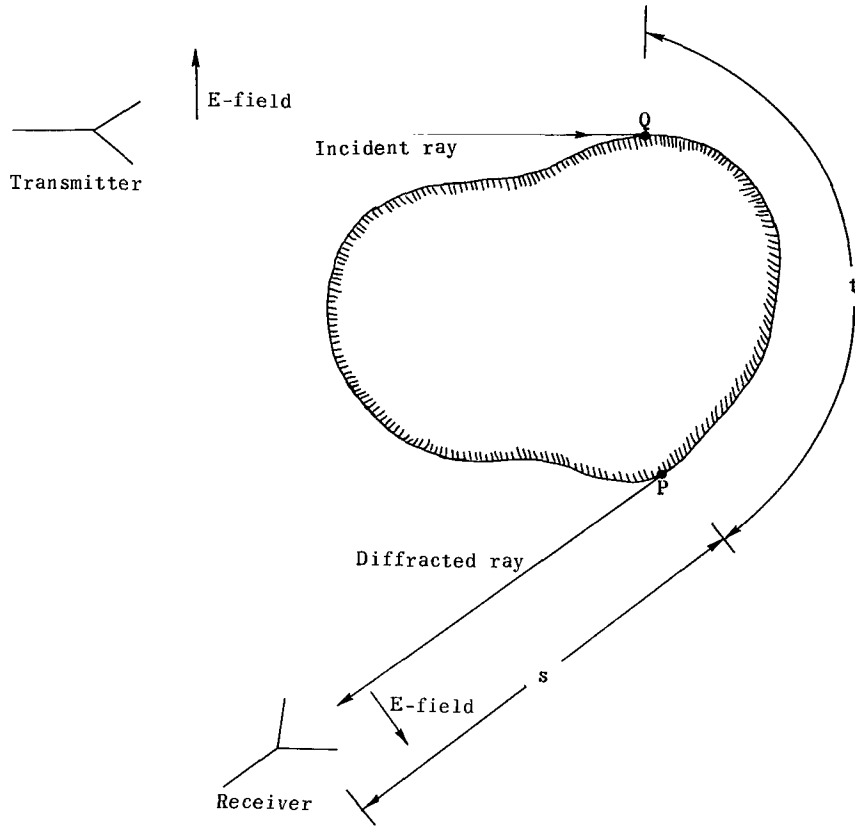


Figure 5.- General concept of creeping-wave diffraction.

splits at the point of tangency with one part continuing along the path of the incident ray and the other traveling along a geodesic on the surface of the body. At each following point, it splits again with one part traveling along the geodesic and the other reradiating along a tangent to the geodesic. From a single incident ray, infinitely many diffracted rays are produced, one of which is reradiated at each point of the geodesic. These waves traveling around the opaque body have been designated as creeping waves introduced first by Franz and Deppermann (ref. 12) for the interpretation of scalar diffraction by circular cylinders and spheres.

The scattered field caused by the creeping wave mechanism for a plane wave incident on a cylinder is given by (ref. 13)

$$E_C(s, \phi) = E_i(Q) \frac{e^{-jk(t+s)}}{\sqrt{s}} \sum_m D_{mh}(Q) D_{mh}(P) e^{-\int_0^t \alpha_{mh}(\rho) ds} \quad (48)$$

which for a right circular cylinder reduces to

$$E_C(s, \phi) = E_i(Q) \frac{e^{-jk(t+s)}}{\sqrt{s}} \sum_m D_{mh}^2 e^{-\alpha_{mh}t} \quad (49)$$

since the radius of curvature is constant. The diffraction coefficients and attenuation constant are given by

$$D_{mh}^2 = D_{mh}(Q) D_{mh}(P) = \text{Diffraction coefficients} \approx \frac{e^{-j\frac{\pi}{12}}}{\sqrt{k}} (k\rho)^{1/3} d_m \quad (50)$$

$$\alpha_{mh} = \text{Attenuation constant} \approx \frac{1}{2\rho} (k\rho)^{1/3} \left[\frac{3\pi}{4} (4m + N) \right]^{2/3} e^{j\frac{\pi}{6}} \quad (51)$$

where

- ρ radius of curvature of body
- k phase constant
- t path length along body
- s distance from point of detachment to observation point
- P point of detachment of creeping wave
- Q point of attachment of creeping wave

For a hard surface (E-field normal to the surface) $d_0 = 1.083$, $d_1 = 0.555$, and $N = 1$; for a soft surface (E-field parallel to the surface) $d_0 = 0.645$, $d_1 = 0.490$, and $N = 3$. The diffraction coefficients and attenuation constants are obtained by comparing the asymptotic series expansion for large values of $k\rho$ of the canonical boundary-value problem with equation (48). (See refs. 13 and 14.)

Rays diffracted by the edges of a slotted cylinder (shown in fig. 6) which are tangent to the surface of the cylinder behave in a similar manner. At each apex point additional diffracted rays are introduced, each of which will travel along the surface of the cylinder and will reradiate tangentially. The creeping-wave field for a slotted conducting cylinder can be expressed as

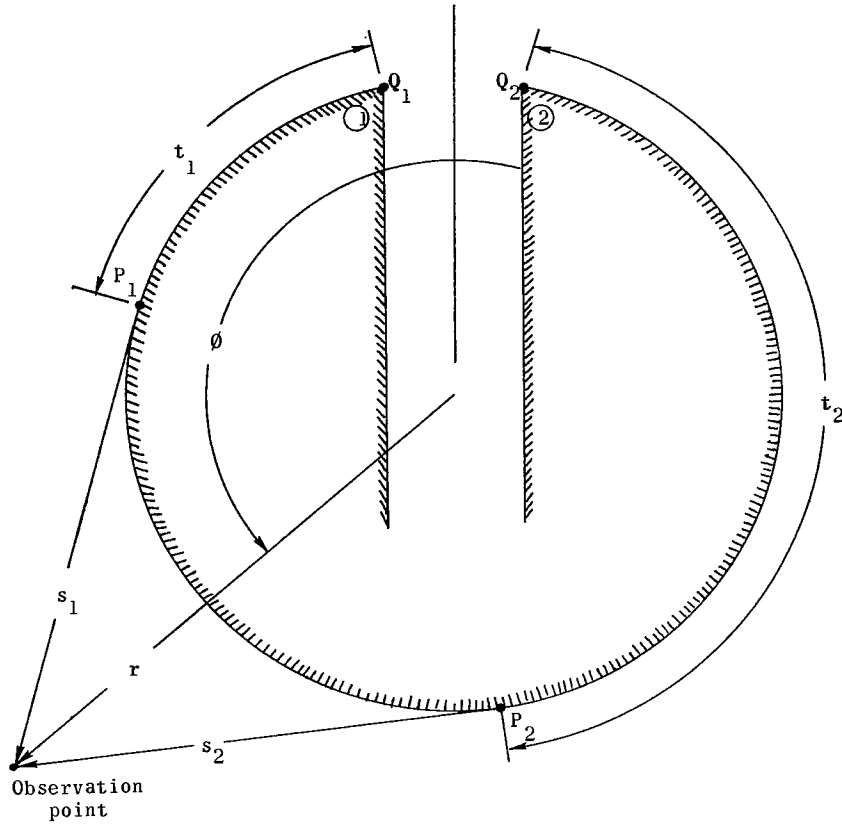


Figure 6.- Slotted-cylinder creeping-wave fields.

$$\begin{aligned}
 E_C(s, \phi) = & E_i(Q_1) \frac{e^{-jk(t_1+s_1)}}{\sqrt{s_1}} \sum_m D_{mh}(Q_1) D_{mh}(P_1) e^{-\int_0^{t_1} \alpha_{mh}(\rho) ds} \\
 & + E_i(Q_2) \frac{e^{-jk(t_2+s_2)}}{\sqrt{s_2}} \sum_n D_{nh}(Q_2) D_{nh}(P_2) e^{-\int_0^{t_2} \alpha_{nh}(\rho) ds}
 \end{aligned} \tag{52}$$

If only the lowest-order creeping-wave mode is considered, equation (52) reduces to

$$\begin{aligned}
 E_C(s, \phi) = & E_i(Q_1) D_{oh}(Q_1) D_{oh}(P_1) \frac{e^{-jk(t_1+s_1)}}{\sqrt{s_1}} e^{-\int_0^{t_1} \alpha_{oh}(\rho) ds} \\
 & + E_i(Q_2) D_{oh}(Q_2) D_{oh}(P_2) \frac{e^{-jk(t_2+s_2)}}{\sqrt{s_2}} e^{-\int_0^{t_2} \alpha_{oh}(\rho) ds}
 \end{aligned} \tag{53}$$

and for a circular cylinder simplifies to

$$\begin{aligned} E_C(r, \phi) = & E_i(Q_1) D_{oh}^2(Q_1) \frac{e^{-jk(t_1+r)}}{\sqrt{r}} e^{-\alpha_{oh}t_1} \\ & + E_i(Q_2) D_{oh}^2(Q_2) \frac{e^{-jk(t_2+r)}}{\sqrt{r}} e^{-\alpha_{oh}t_2} \end{aligned} \quad (54)$$

since the local radius of curvature is the same at P_1 , P_2 , Q_1 , and Q_2 . The far-zone edge diffracted fields are equated to the creeping-wave fields at the shadow boundary to assure continuity of the fields across the boundary between the lit and shadow regions. For the geometry of figure 7, the angular variation of the wedge-diffracted fields along the shadow boundaries is given by

$$R_A = \frac{\sqrt{r}}{e^{-jkr}} E_D \left[r, + \left(\frac{\pi}{2} + \zeta \right) \right] \quad (55)$$

$$R_B = \frac{\sqrt{r}}{e^{-jkr}} E_D \left[r, - \left(\frac{\pi}{2} + \zeta \right) \right] \quad (56)$$

In other words, the angular variation of the wedge-diffracted fields along the shadow boundary is used as the initial value of the angular variations of the creeping waves. Thus, R_A and R_B serve as the coupling mechanisms between wedge-diffracted and creeping waves which assure field continuity along the shadow boundaries. The creeping-wave field for a circular cylinder can then be expressed as

$$E_C(r, \phi) = R_A \frac{e^{-jk(t_1+r)}}{\sqrt{r}} e^{-\alpha_{oh}t_1} + R_B \frac{e^{-jk(t_2+r)}}{\sqrt{r}} e^{-\alpha_{oh}t_2} \quad (57)$$

where

$$R_A = E_i(Q_1) D_{oh}^2(Q_1) = \frac{\sqrt{r}}{e^{-jkr}} E_D \left[r, + \left(\frac{\pi}{2} + \zeta \right) \right] \quad (58)$$

and

$$R_B = E_i(Q_2) D_{oh}^2(Q_2) = \frac{\sqrt{r}}{e^{-jkr}} E_D \left[r, - \left(\frac{\pi}{2} + \zeta \right) \right] \quad (59)$$

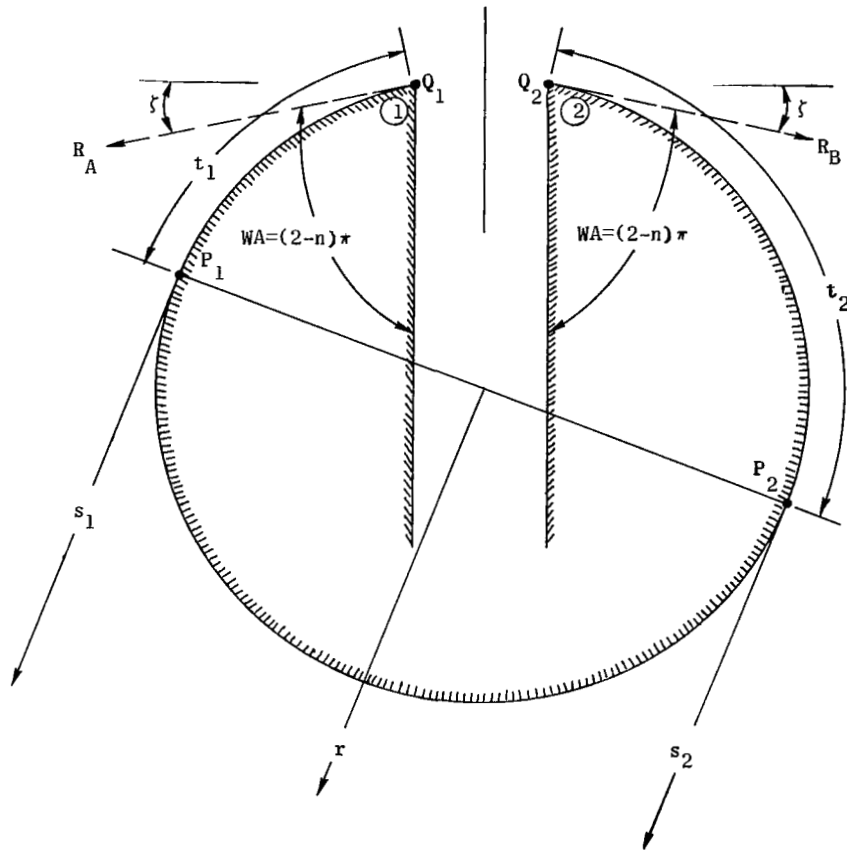


Figure 7.- Far-zone creeping-wave field coordinates.

For a noncircular cylinder the diffraction coefficient D_{oh} is a function of the radius of curvature; therefore, the creeping-wave field must be multiplied by $D_{oh}(P)/D_{oh}(Q)$ to give

$$\begin{aligned}
 E_C(s, \phi) = & R_A \frac{D_{oh}(P_1)}{D_{oh}(Q_1)} \frac{e^{-jk(t_1+s_1)}}{\sqrt{s_1}} e^{-\int_0^{t_1} \alpha_{oh}(\rho) ds} \\
 & + R_B \frac{D_{oh}(P_2)}{D_{oh}(Q_2)} \frac{e^{-jk(t_2+s_2)}}{\sqrt{s_2}} e^{-\int_0^{t_2} \alpha_{oh}(\rho) ds}
 \end{aligned} \tag{60}$$

The wedge approximation of the parallel-plate—cylinder geometry does alter the physical boundaries of the antenna structure and the diffraction mechanism of the fields, especially in the penumbra region. For the wedge approximation, the fields in the $\phi = \pm(\frac{\pi}{2} + \zeta)$ directions travel along the boundaries of the wedges. However, in the

actual antenna structure some of the energy is trapped on the surface of the cylinder and travels along the curved surface reradiating in a tangential direction. Thus the wedge-diffracted and creeping-wave fields in the transition region (penumbra) will not satisfy the field boundary conditions. However, computations carried out by using such a model compare favorably with existing boundary-value solutions and experimental data. Therefore, such a model would be a valid approximation of the structure as far as the diffraction mechanism of the fields is concerned and equations (55) and (56) would serve as the coupling mechanisms between wedge-diffracted and creeping-wave fields.

CIRCULAR CYLINDER RADIATION

The wedge diffraction and creeping wave techniques are first applied for the calculation of the equatorial radiation patterns of axial and circumferential slots on circular conducting cylinders of infinite length. Boundary-value solutions for slots on circular cylinders with common feeds exist and are used for comparison. Once the method is verified, it is employed for pattern calculations of slots whose field distribution is such that modal solutions do not exist and to bodies whose geometric shape does not conform to a coordinate system where the wave equation is separable. In addition, the elevation-plane pattern for finite-length cylinders is analyzed. It should be pointed out that no boundary-value solutions for finite-length cylinders exist, and experimental results are used for comparison. The diffraction contributions from the edges of the cylinder and the effect of the finite-width aperture to the overall pattern are observed. Pattern calculations for more complex geometries such as an elliptical cylinder are carried out in the section "Elliptical Cylinder Radiation."

Equatorial-Plane Pattern of Axial Slots Operating in TEM Mode

The two-dimensional diffraction geometry for an axial slot mounted on a circular cylinder and operating in the TEM mode is shown in figure 8. The junctions formed by the walls of the parallel-plate waveguide and the planes tangent to the surface of the cylinder at the edge points are represented by a pair of infinite wedges of finite included angle, $WA = (2 - n)\pi$. Two regions, lit and shadow, are formed by the imaginary sides of the finite wedges as shown in figure 8.

For $\phi_g = 90^\circ$ of figure 3(a), $R_{D1}(-\phi_0) = 0$, $R_{D1R}(\phi_0) = 0$, $h = w$, $n_1 = n_2 = n$, then equation (31) for the wedge-diffracted field reduces to

$$E_D(r_0, \phi_0) = \frac{e^{-j \left[k \left(r_0 - \frac{w}{2} \sin \phi_0 \right) + \frac{\pi}{4} \right]}}{\sqrt{2\pi k r_0}} \left[R_1(\phi_0) + R_2(\phi_0) e^{-jk w \sin \phi_0} \right] \quad (61)$$

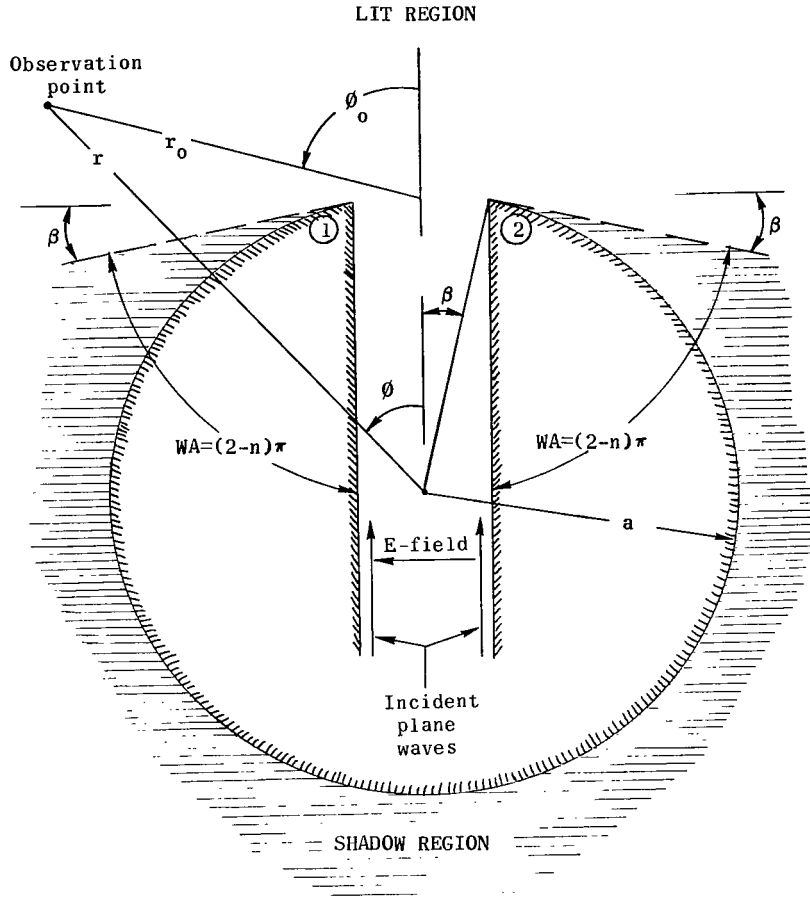


Figure 8.- Lit and shadow regions for circular cylinder.

A shift of coordinates from the aperture to the center of the cylinder is convenient, so that common coordinates will be used for wedge-diffracted and creeping-wave fields. If the far-field approximations

$$r_0 \approx r - a \cos \phi \cos \beta \quad (62)$$

for phase terms and

$$r_0 \approx r \quad (63)$$

for amplitude terms with

$$\phi_0 \approx \phi \quad (64)$$

are assumed, the total wedge-diffracted field is expressed as

$$E_D(r, \phi) = \frac{1}{\sqrt{2\pi k}} \frac{e^{-jkr}}{\sqrt{r}} e^{j \left[k \left(\frac{w}{2} \sin \phi + a \cos \phi \cos \beta \right) - \frac{\pi}{4} \right]} \left[R_1(\phi) + R_2(\phi) e^{-jkw \sin \phi} \right] \quad (65)$$

The creeping-wave contribution as expressed by equation (57) is given by

$$E_C(r, \phi) = R_A \frac{e^{-jkr}}{\sqrt{r}} e^{-t_1(\alpha_{oh} + jk)} + R_B \frac{e^{-jkr}}{\sqrt{r}} e^{-t_2(\alpha_{oh} + jk)} \quad (66)$$

The wedge-diffracted and creeping-wave fields, the e^{-jkr}/\sqrt{r} factor being suppressed, are given by

$$E_D(\phi) = \frac{1}{\sqrt{2\pi k}} e^{j \left[k \left(\frac{w}{2} \sin \phi + a \cos \phi \cos \beta \right) - \frac{\pi}{4} \right]} \left[R_1(\phi) + R_2(\phi) e^{-jkw \sin \phi} \right] \quad (67)$$

and

$$E_C(\phi) = R_A e^{-t_1(\alpha_{oh} + jk)} + R_B e^{-t_2(\alpha_{oh} + jk)} \quad (68)$$

In general, the total field is equal to the sum of the two fields

$$E_T(\phi) = E_D(\phi) + E_C(\phi) \quad (69)$$

However, wedge-diffracted and creeping-wave fields do not exist in all regions. To find the total field in each region, the appropriate wedge-diffracted and creeping-wave fields must be considered as they are tabulated in table I.

Radiation patterns computed by using the boundary-value solution of Wait (ref. 3) and the fields from table I in their respective regions for the diffracted-field solution are shown in figures 9 and 10. The second- and higher-order diffractions are approximated by wedge diffractions resulting from uniform cylindrical waves. Diffracted waves resemble cylindrical waves if they are observed sufficiently far away from any shadow boundary that results from their source. The doubly diffracted waves can be adequately treated as uniform cylindrical waves for guide widths down to about $\lambda/5$. However, third- and higher-order diffractions are not very accurate when $\phi_g = 90^\circ$ since they are viewed at the shadow boundary formed by their source (ref. 32) and the solution is more accurate for wider slots.

TABLE I.- WEDGE-DIFFRACTED AND CREEPING-WAVE FIELDS FOR EQUATORIAL-PLANE PATTERN OF CIRCULAR CYLINDER IN DIFFERENT REGIONS

	Wedge-diffracted field, $E_D(\phi)$	Creepling-wave field, $E_C(\phi)$	t_1	t_2
Region I $0 < \phi \leq \frac{\pi}{2} - \beta$	$e^{\frac{j \left[k \left(\frac{w}{2} \sin \phi + a \cos \phi \cos \beta \right) - \frac{\pi}{4} \right]}{\sqrt{2\pi k}} (R_1 + R_2 e^{-jk w \sin \phi})}$	$R_A e^{-t_1(\alpha_{oh} + jk)} + R_B e^{-t_2(\alpha_{oh} + jk)}$	$a \left(\phi + \frac{3\pi}{2} - \beta \right)$	$a \left(-\phi + \frac{3\pi}{2} - \beta \right)$
Region II $\frac{\pi}{2} - \beta < \phi \leq \frac{\pi}{2}$	$e^{\frac{j \left[k \left(\frac{w}{2} \sin \phi + a \cos \phi \cos \beta \right) - \frac{\pi}{4} \right]}{\sqrt{2\pi k}} (R_1 + R_2 e^{-jk w \sin \phi})}$	$R_B e^{-t_2(\alpha_{oh} + jk)}$	-----	$a \left(-\phi + \frac{3\pi}{2} - \beta \right)$
Region III $\frac{\pi}{2} < \phi \leq \frac{\pi}{2} + \beta$	$e^{\frac{j \left[k \left(\frac{w}{2} \sin \phi + a \cos \phi \cos \beta \right) - \frac{\pi}{4} \right]}{\sqrt{2\pi k}} (R_1)}$	$R_B e^{-t_2(\alpha_{oh} + jk)}$	-----	$a \left(-\phi + \frac{3\pi}{2} - \beta \right)$
Region IV $\frac{\pi}{2} + \beta < \phi \leq \pi$	0	$R_A e^{-t_1(\alpha_{oh} + jk)} + R_B e^{-t_2(\alpha_{oh} + jk)}$	$a \left(\phi - \frac{\pi}{2} - \beta \right)$	$a \left(-\phi + \frac{3\pi}{2} - \beta \right)$

The solutions which consider only first- and second-order diffractions have a discontinuity in the $\phi = \pm 90^\circ$ directions because higher-order diffractions are neglected. The discontinuity and variation from the boundary-value solution in the $\phi = \pm 90^\circ$ directions are greater for smaller guide widths. The solution which takes into account higher-order diffractions eliminates the discontinuity, but it is not very accurate in the geometrical shadow boundary region (penumbra) since the assumption of uniform cylindrical waves is not satisfied for third- and higher-order diffractions.

This analysis is more accurate for large ka cylinders since the decaying exponents of the surface waves are derived from asymptotic series for large ka . When this approach is used, the computations for large ka cylinders do not require any additional details from those of small ka . In contrast, the boundary-value-solution computations for large ka cylinders are not very convenient since Bessel functions of large order and argument are not readily available. Also, the convergence of the radiation pattern function becomes poor for large ka , and higher-order terms must be included (about $2ka$ terms). From an economic point of view, large ka value computations using the boundary-value solution require considerably more computer time compared with the corresponding diffracted-field solution (about a factor of 50) since higher-order terms must be included for convergence.

As the value of ka increases, the field in the shadow region $-\left(\frac{\pi}{2} + \beta\right) > \phi > \left(\frac{\pi}{2} + \beta\right)$ decreases and the ripples start to appear at larger angles. It is noted that the period of the ripples is approximately $180^\circ/ka$. A field plot (voltage against angle) for the cylinder

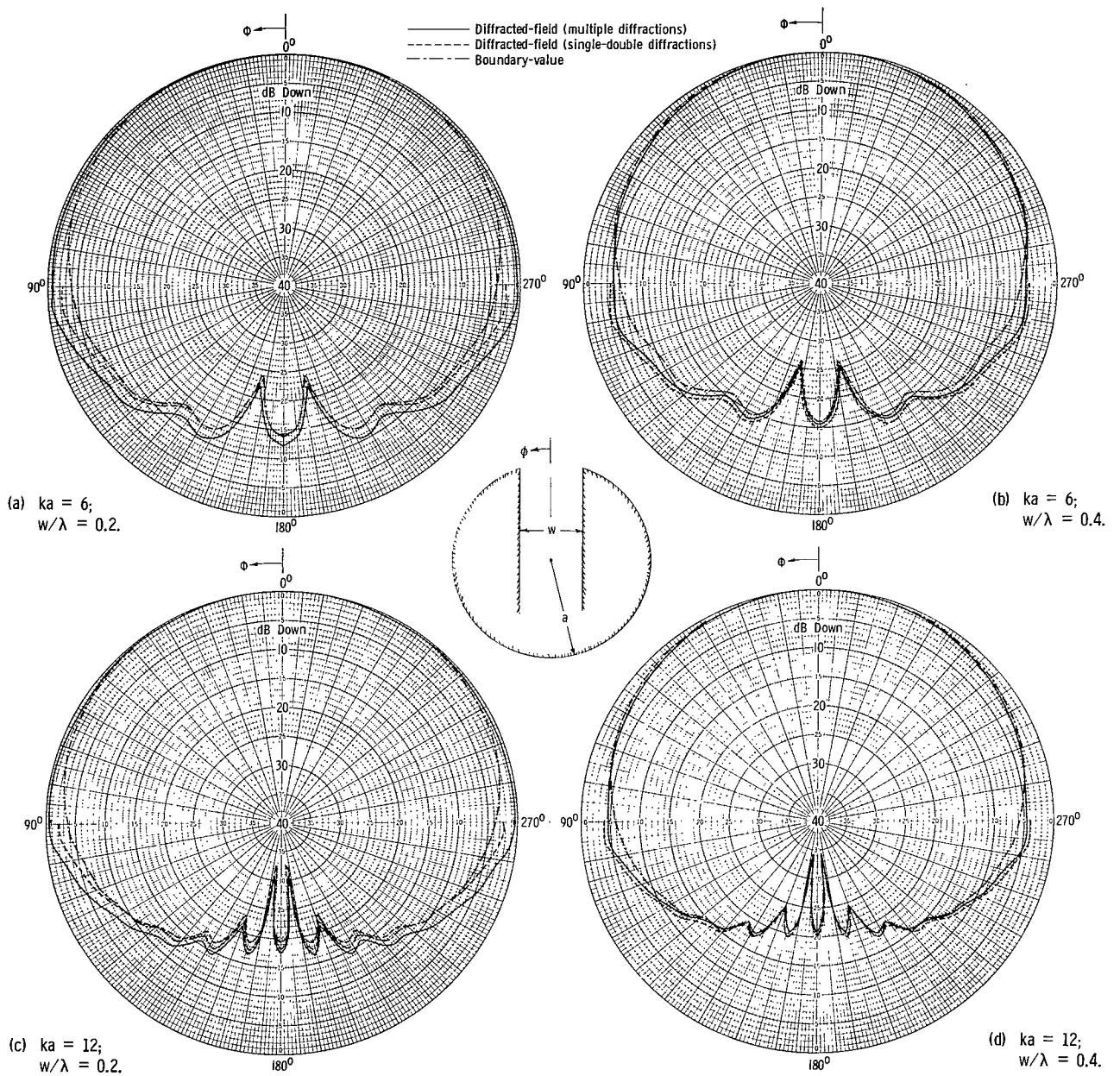


Figure 9.- Radiation patterns of axial infinite slot on smaller circular conducting cylinder using finite wedges (TEM mode).

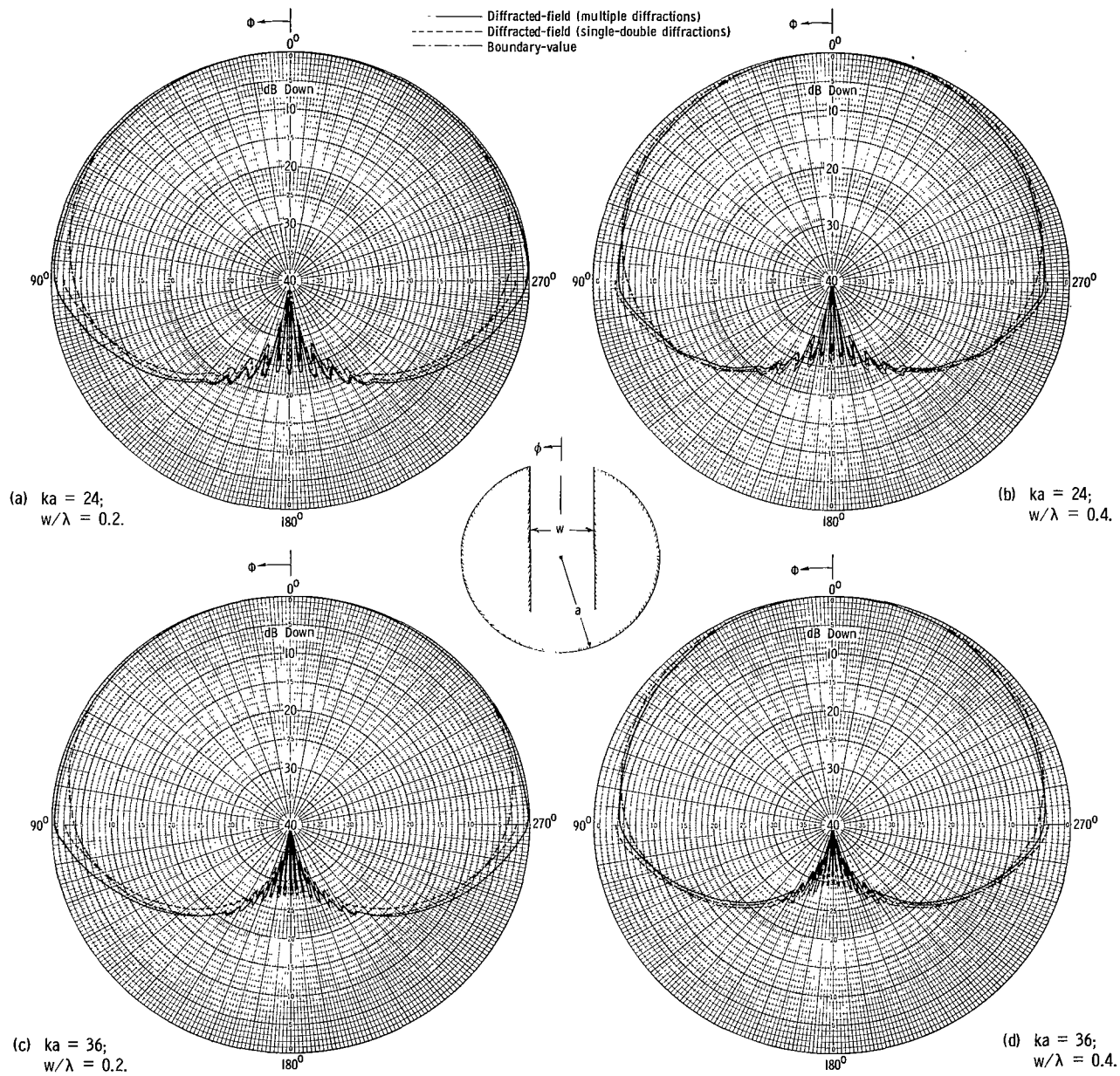


Figure 10.- Radiation patterns of axial infinite slot on larger circular conducting cylinder using finite wedges (TEM mode).

with $ka = 12$ and $w/\lambda = 0.2$ is shown in figure 11. The variations between the boundary-value and wedge-diffracted solutions and the field discontinuity along the $\phi = \pm 90^\circ$ directions are more noticeable on a linear scale. The agreement would be significantly improved for larger cylinders with wider plate separations as shown for the cylinder with $ka = 36$ and $w/\lambda = 0.4$ in figure 12.

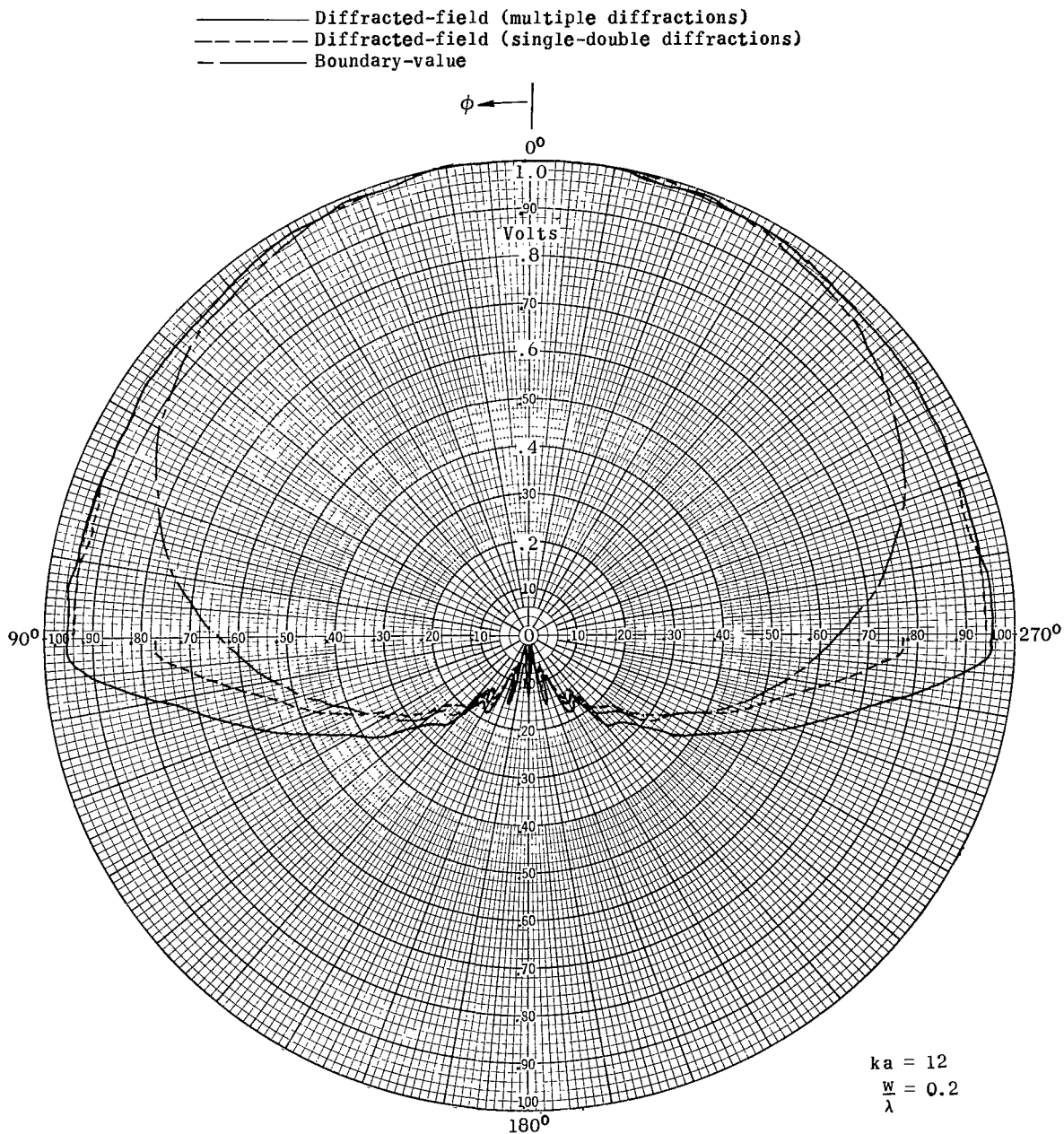


Figure 11.- Field plot of axial infinite slot on circular conducting cylinder ($ka = 12$, $w/\lambda = 0.2$) using finite wedges (TEM mode).

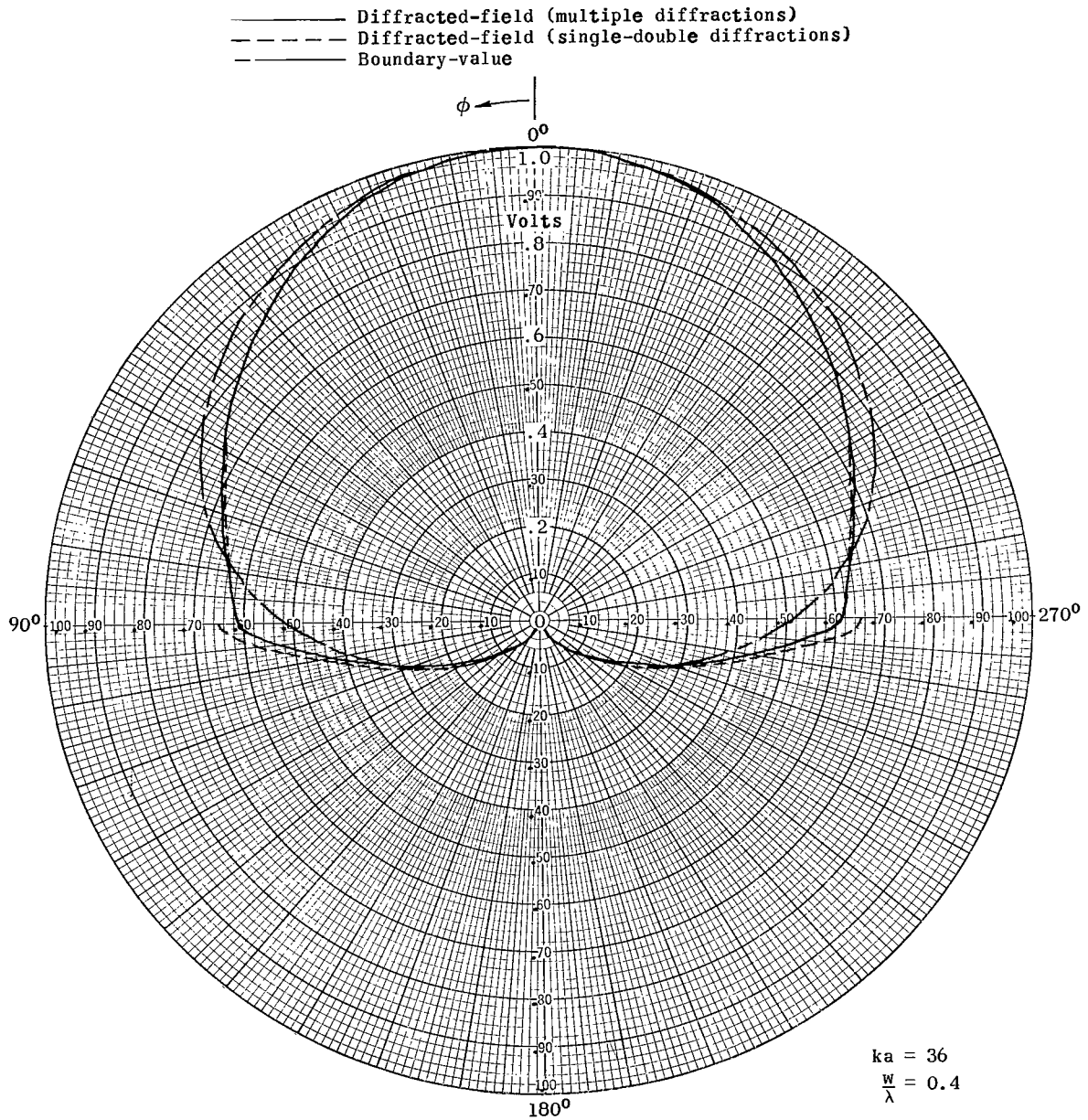


Figure 12.- Field plot of axial infinite slot on circular conducting cylinder ($ka = 36$, $w/\lambda = 0.4$) using finite wedges (TEM mode).

Up to now, the parallel-plate—cylinder geometry has been approximated by a set of wedges of finite included angle ($n \neq 2$) each formed by a wall of the parallel plate and a tangent plane to the cylinder surface at the edge point. For the far field, it would be the presence of the conducting wall for the wedge geometry of figure 3 that would force the field to be zero at $\phi = \pi - WA$. However, there is no such conducting wall in the far

field of the geometry of figure 6 and it is only the edge that needs to be considered. Sommerfeld (ref. 17) points out that patterns on precise diffraction photographs exhibit almost no dependence on the material and shape of the diffraction edge, and a glass surface with radius of curvature of several meters yields essentially the same diffraction fringes as the edge of a razor. Another possible approximation of the parallel-plate—cylinder geometry will be a half-plane (wedge with $n = 2$) instead of a finite wedge ($n \neq 2$). This approximation becomes necessary for the TE_{10} mode because the wedge-diffracted field along the artificial wedge surface separating the lit and shadow regions for the finite-wedge approximation is zero. Thus, no creeping waves will be traveling around the cylinder surface for the TE_{10} mode and no fields in the shadow region. Since this is not true, the half-plane approximation becomes necessary.

However, to verify the validity of the approximations – finite wedge ($n \neq 2$) and half-plane ($n = 2$) – both models are used for the computation of patterns for TEM and TE_{10} mode slots and compared with boundary-value solutions and experimental results.

It was found, by comparison, that another approximation for the TEM mode slot on a circular cylinder was to replace the edge ① geometry by a half-plane ($n = 2$) for the first-order diffraction and by a finite wedge ($n \neq 2$) for second- and higher-order diffractions for the 0° to 180° pattern measured in the counterclockwise direction. The edge ② geometry was replaced by a finite wedge for all orders of diffraction. For the 180° to 360° pattern, the approximations of edge ① geometry are valid for edge ② and vice versa.

The computed results using these approximations are shown in figures 13 and 14 where they are compared with the boundary-value solution. These approximations result in better accuracies for smaller guide widths around the penumbra region than the finite-wedge approximation used for figures 9 and 10. However, the finite-wedge approximation gives better results in the lit region as it should since the fields in the lit region are more strongly dependent on the geometry of the edge of the wedge, whereas the far fields in the penumbra region would be dependent on the fields on the walls of the wedge. It is then concluded that both approximations are valid and a combination of the wedge approximations dependent on the location of the observation point would yield optimum results. As a first order of approximation, either one of the suggested models may be used. A field plot for the cylinder with $ka = 12$ and $w/\lambda = 0.2$ cylinder is shown in figure 15. The accuracy of this approximation of the penumbra region is better seen in this plot when compared with the one in figure 11.

As was pointed out earlier, many models for the parallel-plate—cylinder geometry would give good results as a first-order approximation. Another suggested model for

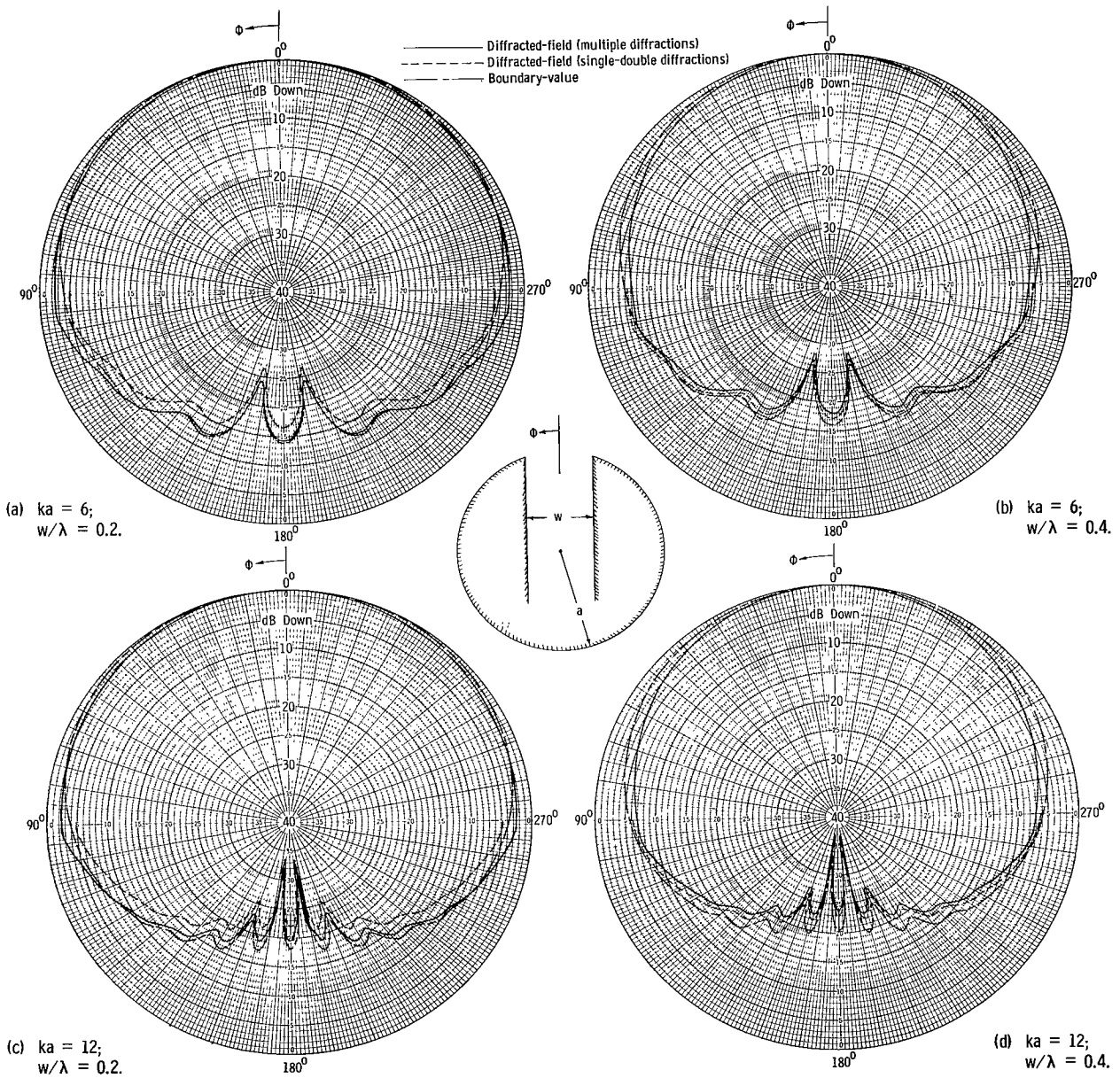


Figure 13.- Radiation patterns of axial infinite slot on smaller circular conducting cylinder using half-plane and finite wedges (TEM mode).

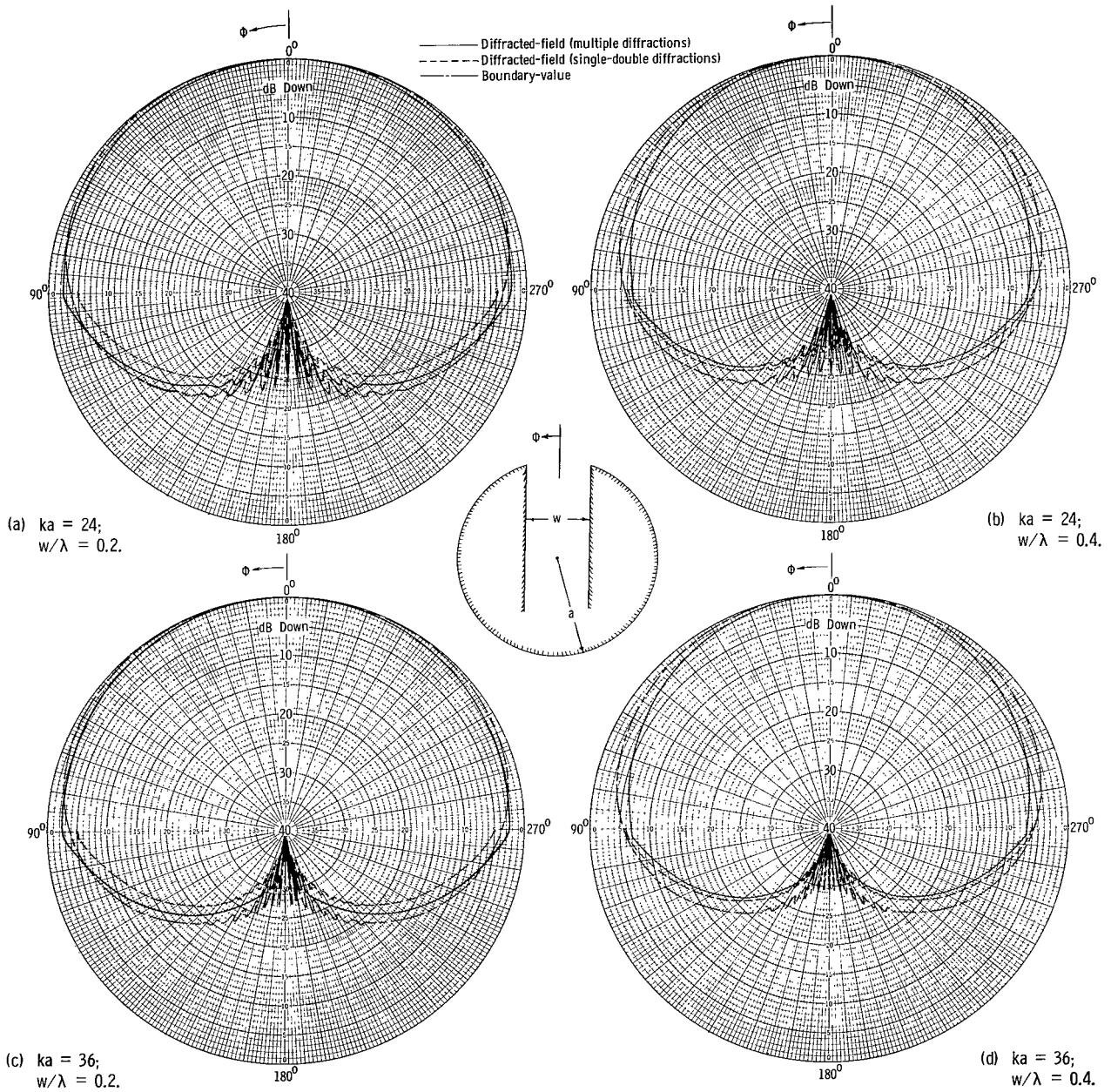


Figure 14.- Radiation patterns of axial infinite slot on larger circular conducting cylinder using half-plane and finite wedges (TEM mode).

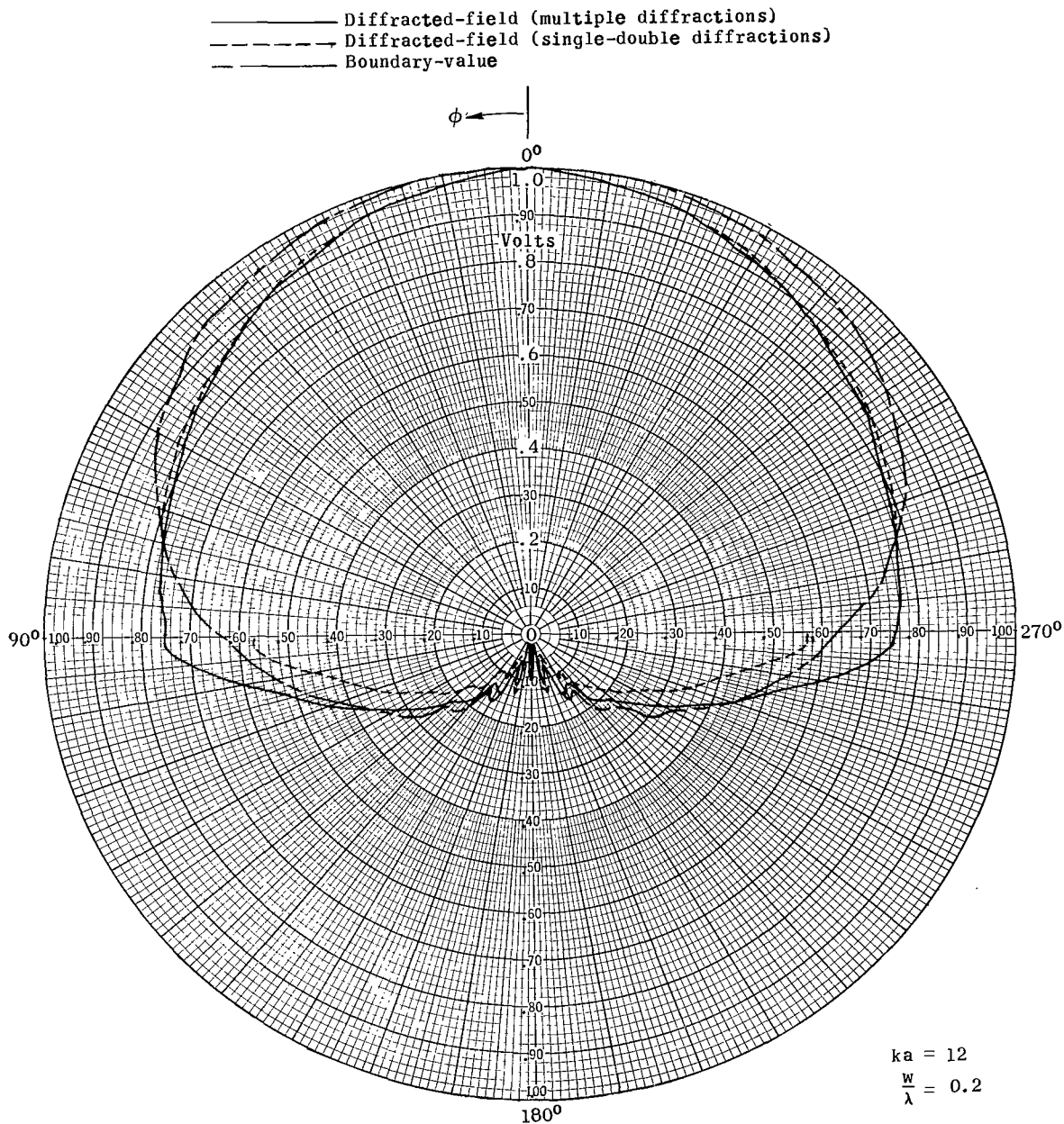


Figure 15.- Field plot of axial infinite slot on circular conducting cylinder using half-plane and finite wedges (TEM mode).

the parallel-plate—cylinder geometry would be a set of half-planes ($n = 2$ for all orders of diffractions). Computed results using such a model are shown in figure 16 where reasonable agreement between the boundary-value and diffracted solutions is indicated.

Sometimes it may be desirable to have the maximum radiation oriented at a given angle other than the zero-degree direction described previously. One way of accomplishing this would be to have the feed of the waveguide mounted in a slanted position.

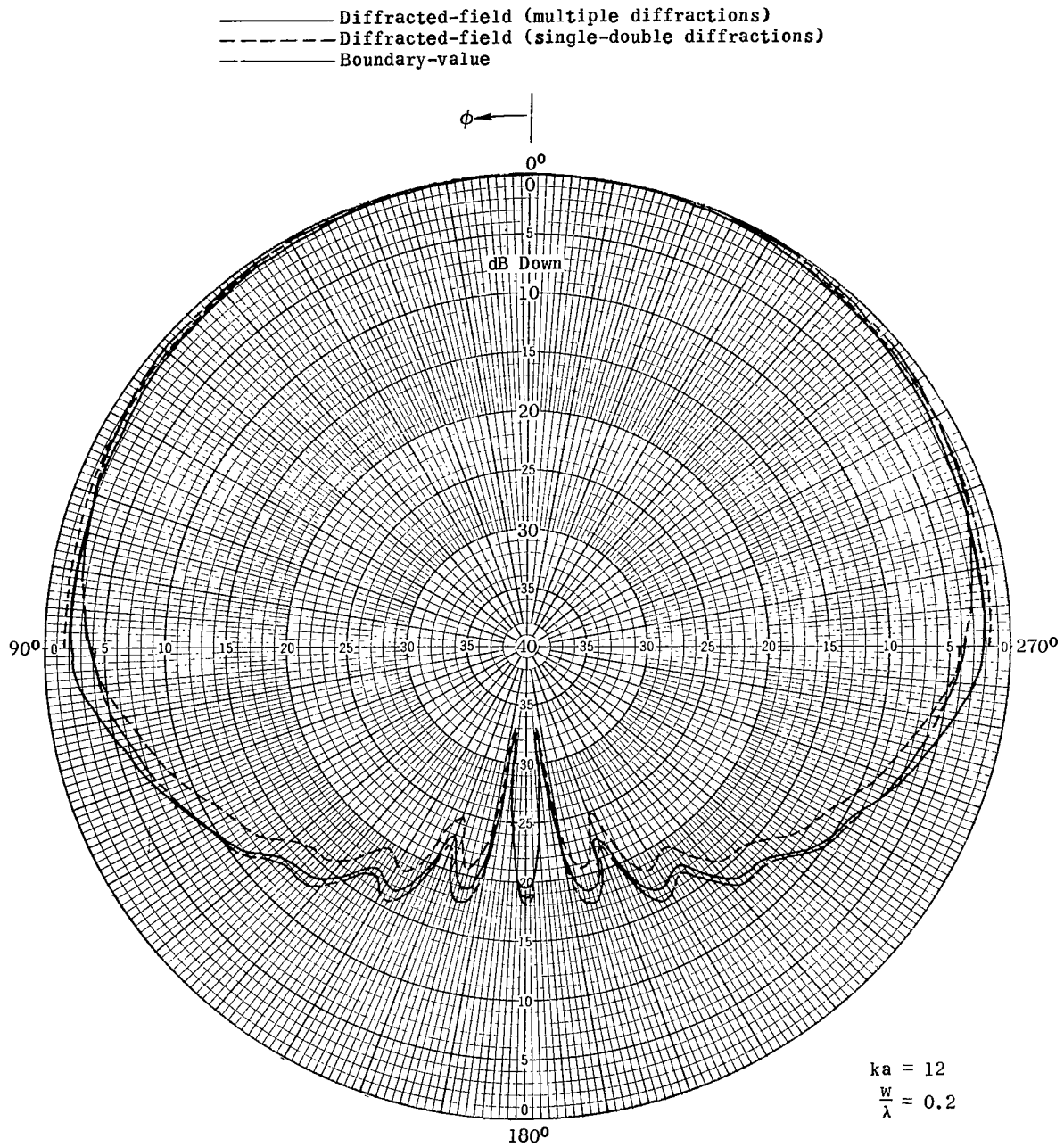


Figure 16.- Radiation pattern of axial infinite slot on circular conducting cylinder using half-planes (TEM mode).

TEM mode propagation along the parallel plate is assumed but the aperture-field distribution will not be uniform in this case. Propagation of this mode in a guide mounted on a cylinder in a slanted position has no boundary-value solution. However, the technique of diffracted fields can be used to obtain the radiation pattern. The two-dimensional

geometry of this mode is shown in figure 17. The modified equation for the diffracted field is given by

$$E_D(\phi) = \frac{1}{\sqrt{2\pi k}} e^{j \left\{ k \left[a \cos \phi \cos \beta - \frac{h}{2} \cos(\phi + \epsilon + \phi_g) \right] - \frac{\pi}{4} \right\}} \left[R_1(\phi) + R_2(\phi) e^{jkh \cos(\phi + \epsilon + \phi_g)} + R_1(-\phi) e^{-j2kw \sin(\phi + \epsilon)} \right] \quad (70)$$

where

$$\phi_g = \frac{\pi}{2} - \epsilon \quad (71)$$

$$h = \frac{w}{\sin \phi_g} \quad (72)$$

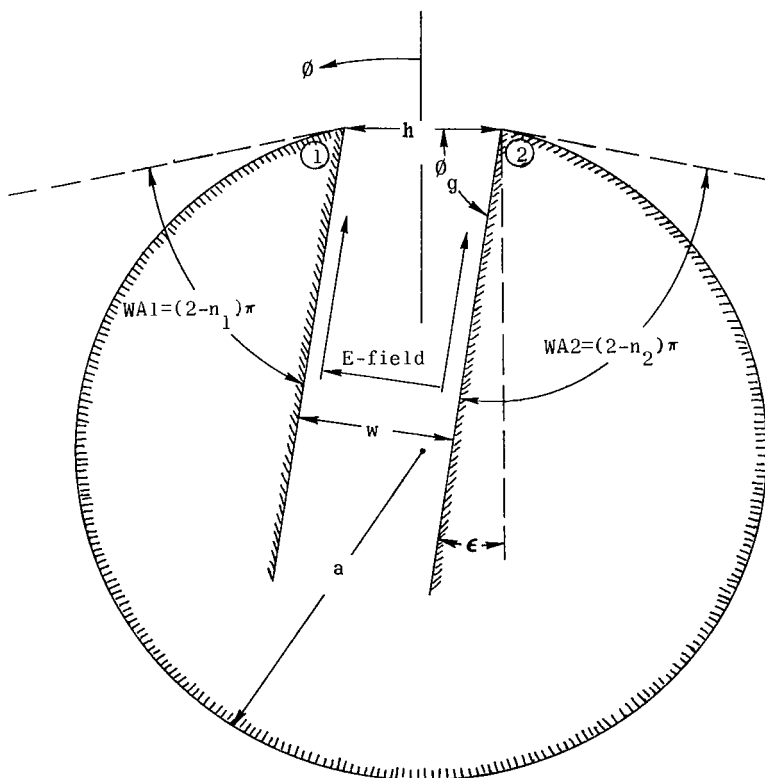


Figure 17.- Slanted feed parallel-plate waveguide geometry.

and the regions where the appropriate wedge-diffracted fields are applicable are given in the following table:

Ray	Region
$R_1(\phi)$	$\frac{\pi}{2} + \beta > \phi > -\frac{\pi}{2}$
$R_2(\phi)$	$\frac{\pi}{2} > \phi > -\left(\frac{\pi}{2} + \beta\right)$
$R_1(-\phi)$	$\frac{\pi}{2} - \epsilon > \phi > (\phi_g - \epsilon)$

The creeping-wave field is the same as that given by equation (68) applicable in the regions given in table I.

The computed radiation patterns for this mode of operation are shown in figure 18 and a field plot for one cylinder in figure 19. The maximum radiation for the cases investigated is oriented at an angle $\phi = -\epsilon/2$. This agrees with the physical reasoning by observing the reflection mechanism of the rays from edge ① by the side of wedge 2. It can then be concluded that by slanting the feed waveguide at a given angle, it will orient the maximum radiation in a direction other than $\phi = 0^\circ$. The discontinuities observed in the solution which considers only single-double diffractions occur because third- and higher-order diffractions which are neglected become significant.

Equatorial-Plane Pattern of Circumferential Slots

Operating in TE_{10} Mode

The TE_{10} mode propagation in a parallel-plate guide can be represented by two plane TEM waves reflecting obliquely back and forth between the waveguide walls with the electric field parallel to the edge of the walls. The approximation of the parallel-plate—cylinder geometry by a set of wedges each formed by a waveguide wall and a tangent plane to the cylinder surface at the edge point will not satisfy the tangential electric-field boundary conditions. In order to overcome this obstacle, the half-plane approximation is used as a model. The boundary-value solution for a circumferential slot operating in the TE_{10} mode and mounted on a circular cylinder exists and is used for comparison.

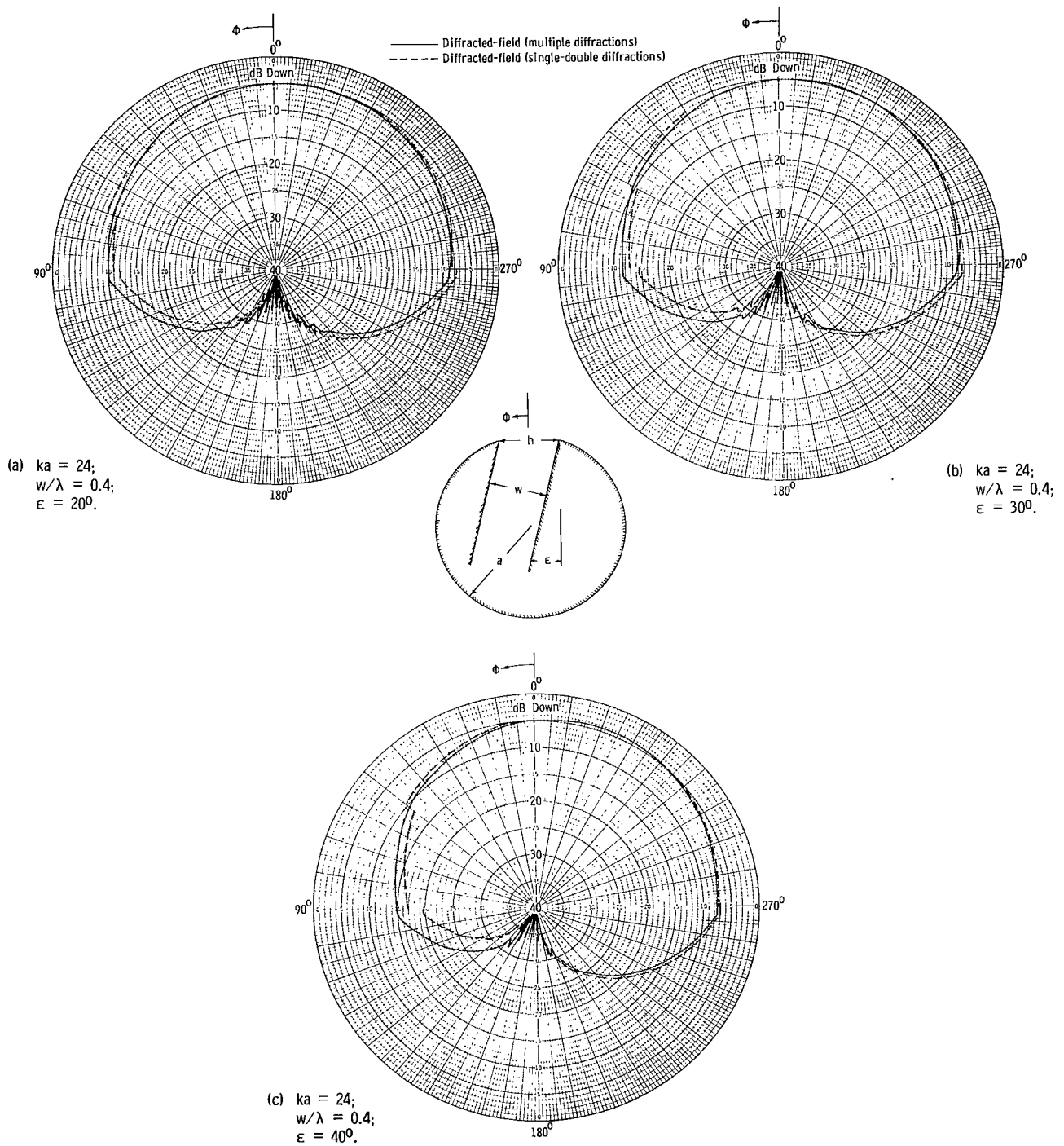


Figure 18.- Radiation patterns of axial infinite slot on circular conducting cylinder with slanted feed (TEM mode).

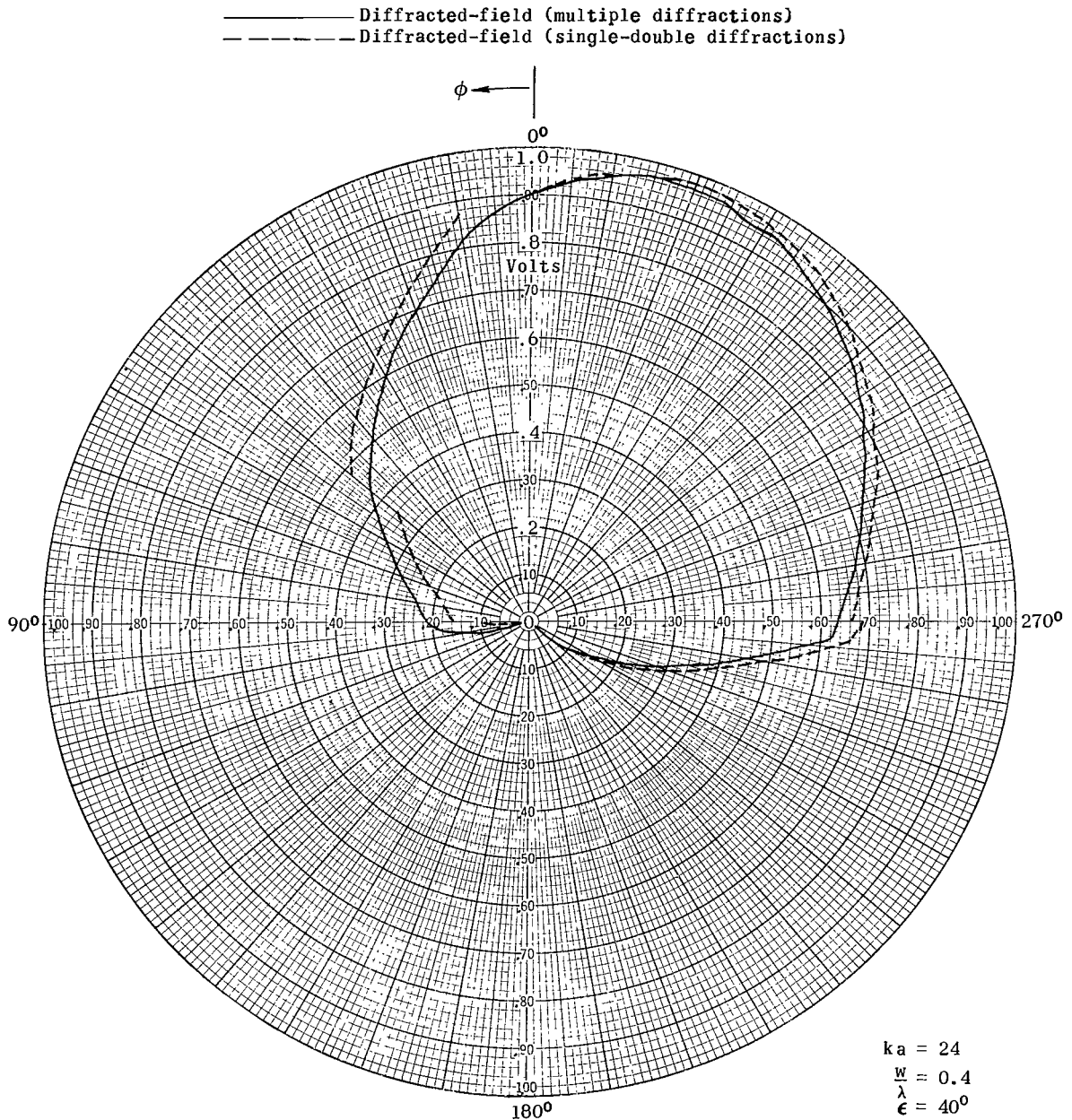


Figure 19.- Field plot of axial infinite slot on circular conducting cylinder with slanted feed (TEM mode).

The two-dimensional diffraction geometry is shown in figure 20. It was found by comparison with the boundary-value solution that one approximation was to replace the edge ① geometry by a half-plane ($n = 2$) for the first-order diffraction and by a finite wedge ($n \neq 2$) for second- and higher-order diffractions for the 0° to 180° pattern measured in the counterclockwise direction. The edge ② geometry was replaced by a

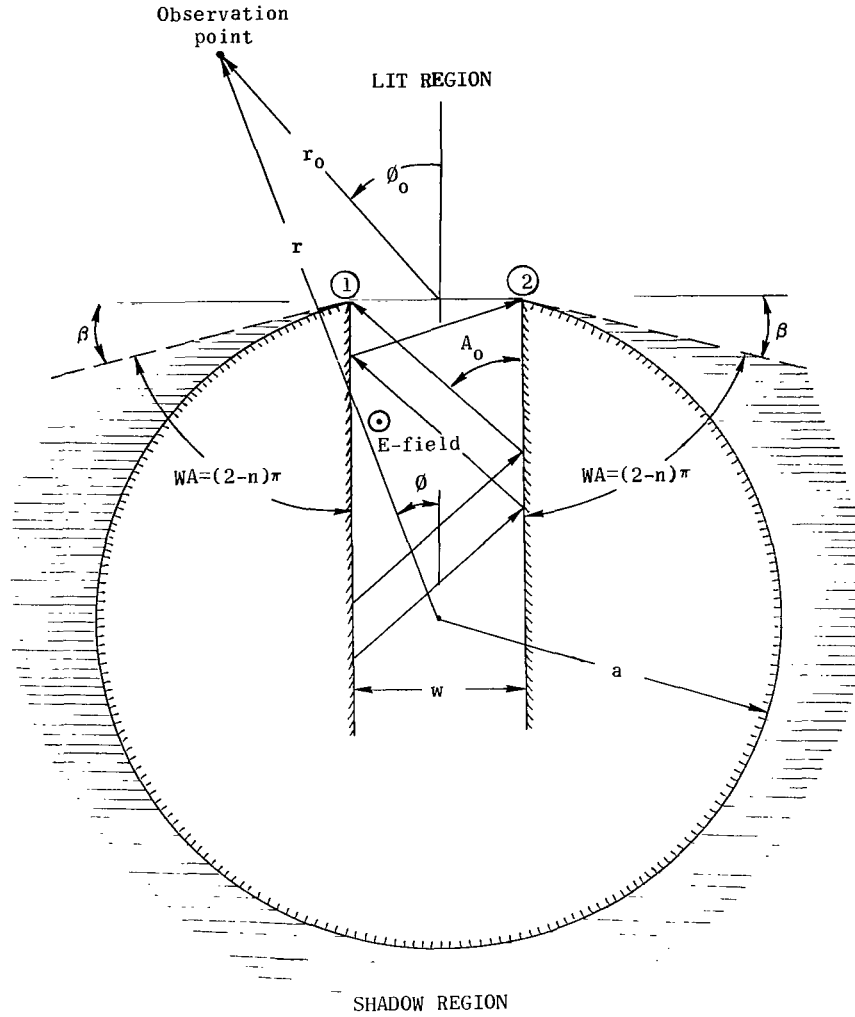


Figure 20.- Diffraction geometry for a TE₁₀ mode circumferential slot.

finite wedge for all orders of diffraction. For the 180° to 360° pattern, the approximations of edge ① are valid for edge ② and vice versa.

The wedge-diffracted field is given by

$$E_D(\phi) = \frac{1}{\sqrt{2\pi k}} e^{j \left[k \left(\frac{w}{2} \sin \phi + a \cos \phi \cos \beta \right) - \frac{\pi}{4} \right]} \left(R_1 + R_2 e^{-jkw \sin \phi} \right) \quad (73)$$

$$R_1 = R_{D1}^{(1)} + R_{D1}^{(h)} \quad (74)$$

$$R_2 = R_{D2}^{(1)} + R_{D2}^{(h)} \quad (75)$$

where $R_{D1}^{(1)}$, $R_{D1}^{(h)}$, $R_{D2}^{(1)}$, and $R_{D2}^{(h)}$ are given by equations (43), (46), (44), and (47) with $\phi_g = 90^\circ$, $R_{D1}(-\phi) = 0$, and $R_{1P} = 0$. The creeping-wave contribution is given by

$$E_C(\phi) = R_A e^{-t_1(\alpha_{OS} + jk)} + R_B e^{-t_2(\alpha_{OS} + jk)} \quad (76)$$

where

$$R_A = E_D \left[+ \left(\frac{\pi}{2} + \beta \right) \right] \quad (77)$$

$$R_B = E_D \left[- \left(\frac{\pi}{2} + \beta \right) \right] \quad (78)$$

as given by equation (73) and

$$\alpha_{OS} = \frac{1}{2a} (ka)^{1/3} \left(\frac{9\pi}{4} \right)^{2/3} e^{j\frac{\pi}{6}} \quad (79)$$

The regions where the appropriate wedge-diffracted and creeping-wave fields are applicable are identical to those shown in table I for the TEM mode.

The computed results using this approximation are shown in figure 21 along with the boundary-value solution. It is noted that the solution which includes higher-order diffractions gives the best results. A noticeable discontinuity is present at the shadow boundary when higher-order diffractions are neglected.

Another approximation of the parallel-plate—cylinder geometry would be a set of half-planes ($n = 2$ for all orders of diffraction) as was true for the TEM mode. Computed results using this model are shown in figure 22. A good agreement is indicated. The discontinuity in the $\phi = \pm 90^\circ$ directions for the single-double diffractions is again present since higher-order diffractions are neglected.

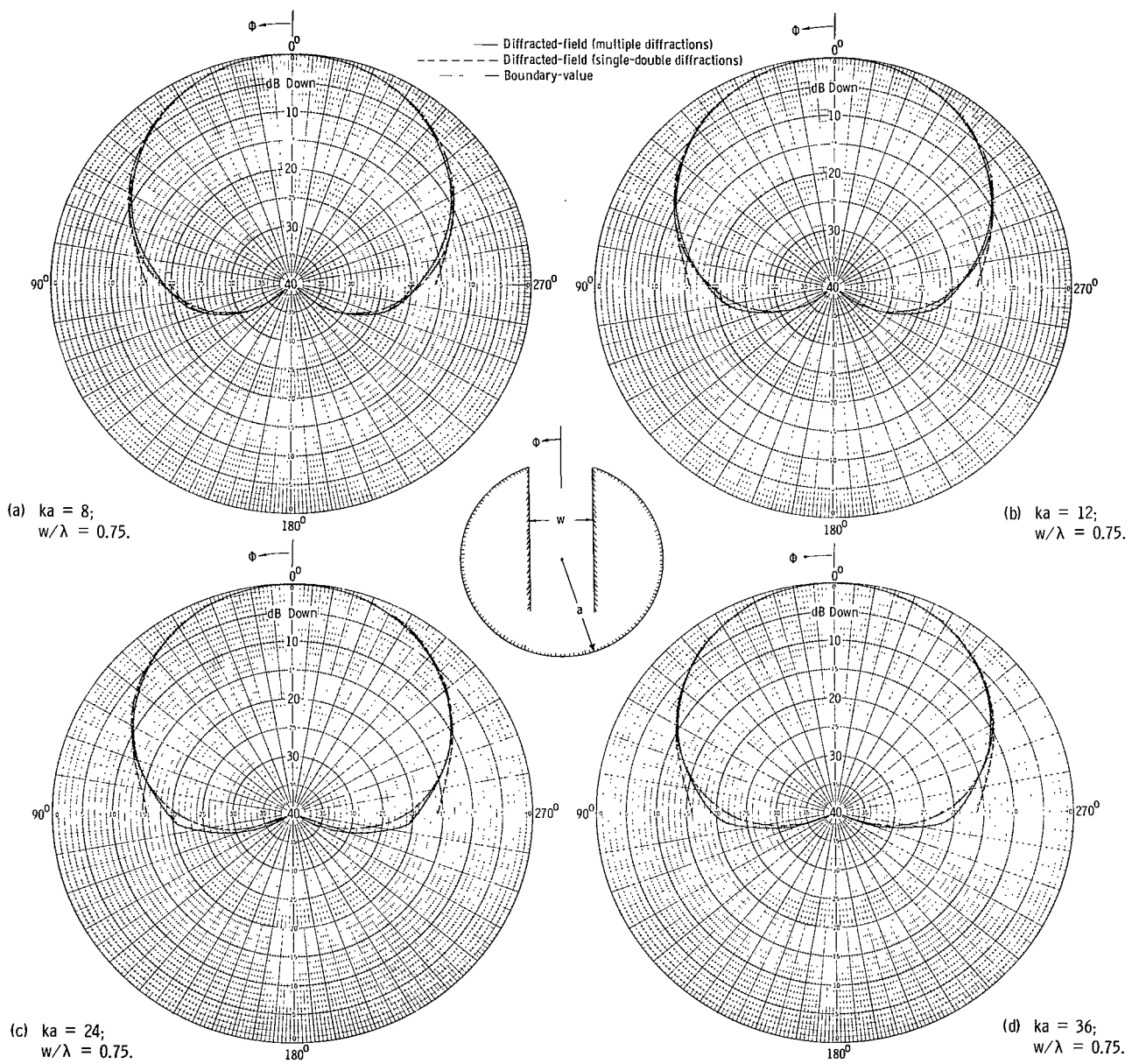


Figure 21.- Radiation patterns of circumferential slot on circular conducting cylinder using half-plane and finite wedges (TE_{10} mode).

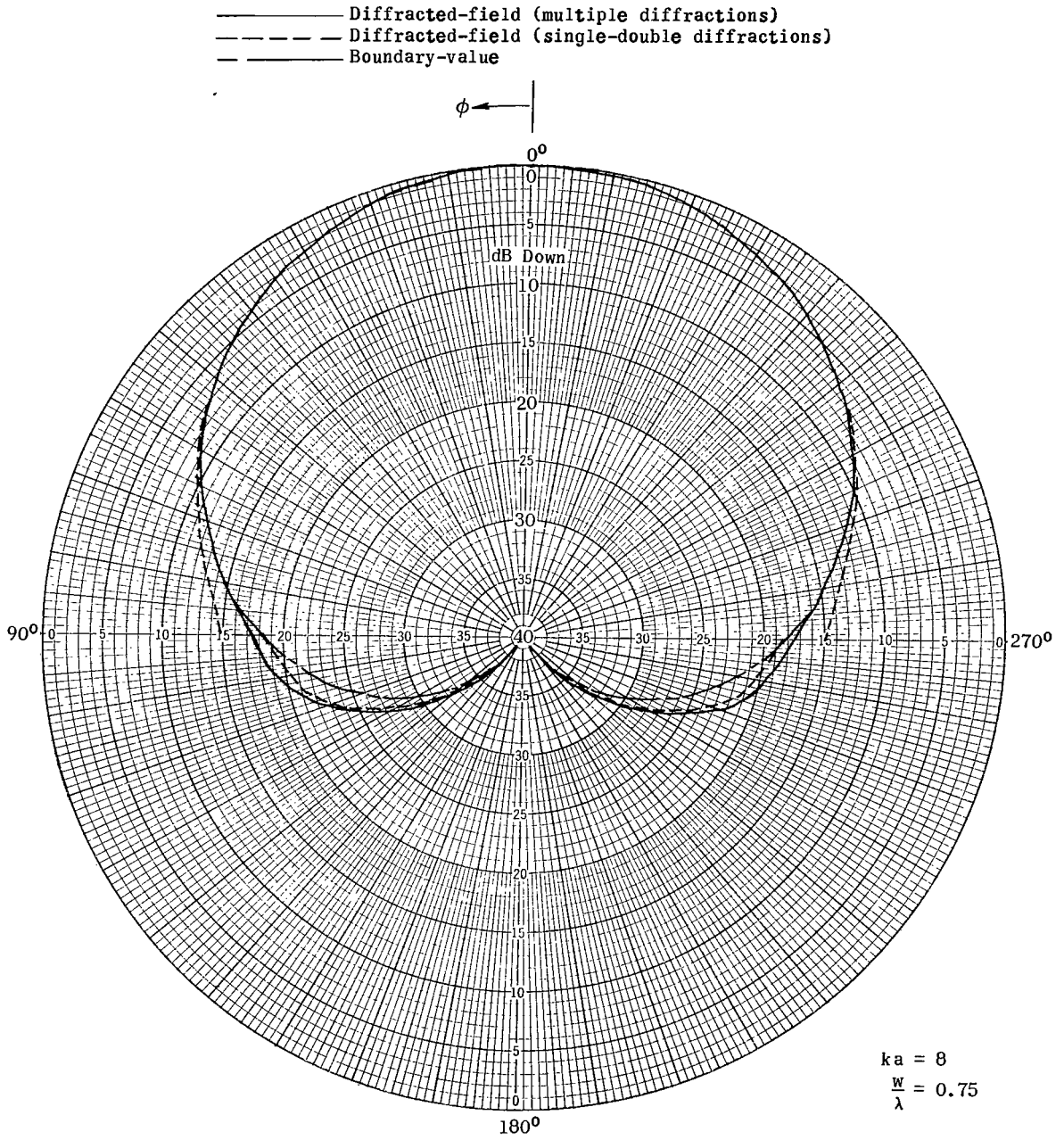


Figure 22.- Radiation pattern of circumferential slot on circular conducting cylinder using half-planes (TE_{10} mode).

Elevation-Plane Pattern of Circumferential Slots on Finite-Length Cylinders Operating in TEM Mode

The elevation-plane pattern $(F(\theta))_{\phi=0}$ for a finite-length conducting cylinder can be computed by using wedge-diffraction techniques. The diffracted fields from the ends of the cylinder and their contribution to the overall radiation pattern can be readily computed. Although boundary-value solutions for circular conducting cylinders of infinite length exist (refs. 1 and 2), no solution which takes into account finite length is available. To check the validity of the technique, experimental results were used for comparison.

The two-dimensional geometry of a slotted cylinder operating in the TEM mode is shown in figure 23. The diffracted field for the TEM mode from edges ① and ② is given by

$$E_D(r_o, \theta_o) = e^{-j\left(kr_o + \frac{\pi}{4}\right)} \frac{R_D(\theta_o)}{\sqrt{2\pi kr_o}} \quad (80)$$

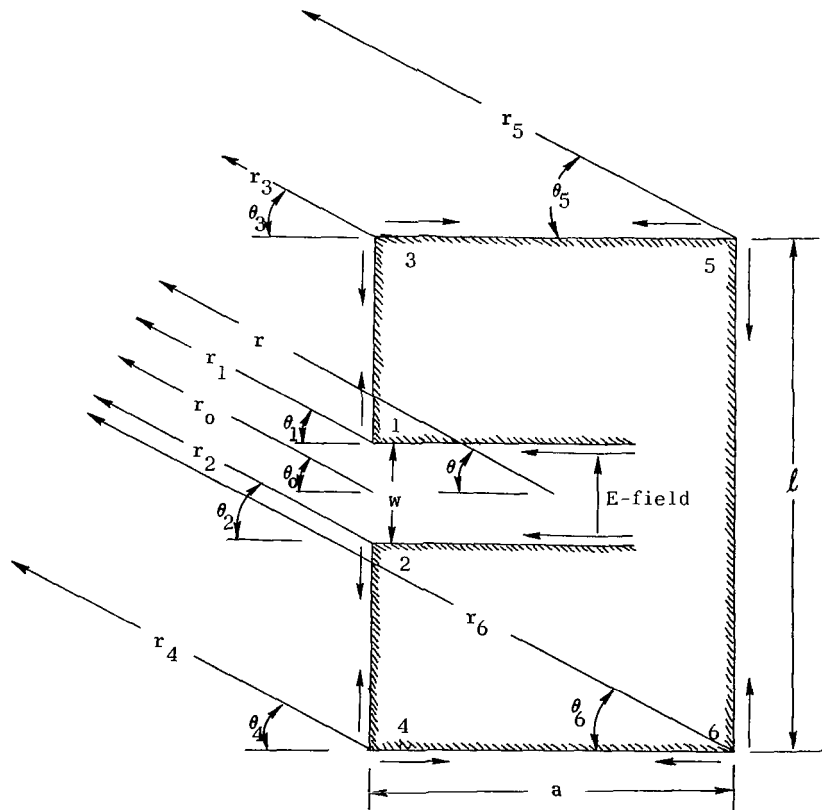


Figure 23.- Diffraction mechanism geometry for elevation-plane pattern.

where

$$\mathbf{R}_D(\theta_0) = e^{j\frac{kw}{2}\sin\theta_0} \left[\mathbf{R}_1(\theta_0) + \mathbf{R}_2(\theta_0)e^{-jkw\sin\theta_0} \right] \quad (81)$$

and $\mathbf{R}_1(\theta_0)$ and $\mathbf{R}_2(\theta_0)$ are given by equations (38) and (34). Diffractions from the aperture in the $\theta_0 = \pm\pi/2$ directions will be diffracted by wedges 3 and 4 which in turn will be diffracted by wedges 1, 2, 5, and 6. This process continues to higher-orders of diffraction.

The reciprocity principle (see appendix) is applied to calculate the singly diffracted field by wedge 3; this leads to

$$\mathbf{E}_{D3}^{(1)}(r_3, \theta_3) = \frac{e^{-j\left(kr_3 + \frac{\pi}{4}\right)}}{\sqrt{2\pi kr_3}} \mathbf{R}_{D3}^{(1)}(\theta_3) \quad (82)$$

where

$$\mathbf{R}_{D3}^{(1)}(\theta_3) = \mathbf{R}_1\left(\frac{\pi}{2}\right) \left[\mathbf{V}_B\left(\frac{l-w}{2}, \frac{\pi}{2} + \theta_3, n_3\right) \right] \quad (83)$$

The singly diffracted ray from wedge 3 in the direction of wedge 5 ($\theta_3 = 180^\circ$) will be diffracted again and its contribution is

$$\mathbf{E}_{D5}^{(1)}(r_5, \theta_5) = \frac{e^{-j\left(kr_5 + \frac{\pi}{4}\right)}}{\sqrt{2\pi kr_5}} \mathbf{R}_{D5}^{(1)}(\theta_5) \quad (84)$$

where

$$\mathbf{R}_{D5}^{(1)}(\theta_5) = \mathbf{R}_{D3}^{(1)}(\pi) \left[\mathbf{V}_B(a, \theta_5, n_5) \right] \quad (85)$$

Diffractions from wedge 5 in the directions of wedge 3 ($\theta_5 = 0^\circ$) and wedge 6 ($\theta_5 = 270^\circ$) will cause additional diffractions. If the length of the cylinder is assumed to be several wavelengths, the diffractions by wedge 6 are negligible. However, the second-order diffractions from wedge 3 are given by

$$\mathbf{E}_{D3}^{(2)}(r_3, \theta_3) = \frac{e^{-j\left(kr_3 + \frac{\pi}{4}\right)}}{\sqrt{2\pi kr_3}} \mathbf{R}_{D3}^{(2)}(\theta_3) \quad (86)$$

where

$$R_{D3}^{(2)}(\theta_3) = R_{D5}^{(1)}(\theta_5=0) \left[\bar{V}_B(a, \pi - \theta_3, n_3) \right] \quad (87)$$

The same procedure used to calculate the fields diffracted by wedges 3 and 5 can be applied to calculate the fields diffracted from wedges 4 and 6 being initiated by the aperture diffractions in the $\theta_0 = -\pi/2$ direction.

The first-order diffracted fields from wedges 4 and 6 are given by

$$E_{D4}^{(1)}(r_4, \theta_4) = \frac{e^{-j\left(kr_4 + \frac{\pi}{4}\right)}}{\sqrt{2\pi kr_4}} R_{D4}^{(1)}(\theta_4) \quad (88)$$

where

$$R_{D4}^{(1)}(\theta_4) = R_2\left(-\frac{\pi}{2}\right) \left[\bar{V}_B\left(\frac{l-w}{2}, \frac{\pi}{2} - \theta_4, n_4\right) \right] \quad (89)$$

and

$$E_{D6}^{(1)}(r_6, \theta_6) = \frac{e^{-j\left(kr_6 + \frac{\pi}{4}\right)}}{\sqrt{2\pi kr_6}} R_{D6}^{(1)}(\theta_6) \quad (90)$$

where

$$R_{D6}^{(1)}(\theta_6) = R_{D4}^{(1)}(-\pi) \left[\bar{V}_B(a, 2\pi - \theta_6, n_6) \right] \quad (91)$$

and the second-order diffracted field from wedge 4 by

$$E_{D4}^{(2)}(r_4, \theta_4) = \frac{e^{-j\left(kr_4 + \frac{\pi}{4}\right)}}{\sqrt{2\pi kr_4}} R_{D4}^{(2)}(\theta_4) \quad (92)$$

where

$$R_{D4}^{(2)}(\theta_4) = R_{D6}^{(1)}(2\pi) \left[\bar{V}_B(a, \pi + \theta_4, n_4) \right] \quad (93)$$

Equations (80) to (93) were all based upon the validity of the reciprocity principle as outlined in the appendix.

Shifting the coordinates from the individual edges to the center of the cylinder and assuming the far-field approximations

$$\left. \begin{aligned} r_0 &\approx r - \frac{a}{2} \cos \theta \\ r_3 &\approx r - d \cos (\gamma - \theta) \\ r_4 &\approx r + d \cos (\pi - \gamma - \theta) \\ r_5 &\approx r - d \cos (\pi - \gamma - \theta) \\ r_6 &\approx r + d \cos (\gamma - \theta) \end{aligned} \right\} \quad (94)$$

for phase terms and

$$r_0 \approx r_3 \approx r_4 \approx r_5 \approx r_6 \approx r \quad (95)$$

for amplitude terms with

$$\theta_0 \approx \theta_3 \approx \theta_4 \approx \theta_5 \approx \theta_6 \approx \theta \quad (96)$$

where

$$d = \left[\left(\frac{a}{2} \right)^2 + \left(\frac{l}{2} \right)^2 \right]^{1/2} \quad (97)$$

$$\gamma = \tan^{-1} \frac{l}{a} \quad (98)$$

the diffracted fields, with the $e^{-j\left(kr + \frac{\pi}{4}\right) / \sqrt{2\pi kr}}$ factor being suppressed, are shown in table II.

It should be pointed out that additional diffractions by each wedge are present and can very conveniently be accounted for. However, for cylinders with several wavelength

radius and length such diffractions have secondary effects and can be neglected. It is apparent from figure 23 that the two-dimensional geometry used for the formulation of the elevation-plane pattern of a finite-length slotted cylinder is identical to the cross-section configuration of a slotted finite-width ground plane.

The computed results using the fields from table II are shown in figure 24 where they are compared with experimental data. Very good agreement between theory and experiment is indicated. The ripples in the

$-\frac{\pi}{2} < \theta < \frac{\pi}{2}$ region are present because of the diffraction contribution from the edges of the cylinder, and they become negligible as the length becomes large. The experimental results were obtained from slotted ground plane models since it was deduced that their two-dimensional geometry is identical to that of a slotted cylinder.

The beamwidth of the main lobe is decreased as the aperture width is increased. The smoothest pattern and the lowest back lobes are obtained for the aperture whose width is exactly 1 wavelength since complete cancellation of the fields diffracted from wedges 1 and 2 in the $\theta = \pm\frac{\pi}{2}$ directions occurs. The ripples in the $-90^\circ < \theta < 90^\circ$ region which are much in evidence in figures 24(a) and (b) do not appear in figures 24(c) and (d) because the fields in the $\theta = \pm\frac{\pi}{2}$ directions are very weak and any diffractions from the edges are negligible. Additional lobes appear as the aperture width is larger than 1 wavelength.

Another formulation for the diffractions from wedges 1 and 2 would be to use continuous double diffractions. (See ref. 36.) In this case, doubly diffracted rays from wedge 2, $R_{D2}^{(2)}(\theta)$, are neglected in the $0^\circ < \theta < 90^\circ$ region while doubly diffracted rays from wedge 1, $R_{D1}^{(2)}(\theta)$, are neglected in the $-90^\circ < \theta < 0^\circ$ region. Computed results using the above formulation are shown in figure 25 where they are compared with experimental results. Again, very good agreement between theory and experiment is indicated.

TABLE II.- WEDGE-DIFFRACTED FIELDS FOR ELEVATION-PLANE PATTERN OF FINITE-LENGTH CYLINDER IN DIFFERENT REGIONS

Diffraction wedge	Wedge-diffracted field	Region
1 and 2	$E_D(\theta) = e^{j\frac{ka}{2}\cos\theta} [R_D(\theta)]$	$-\frac{\pi}{2} < \theta < \frac{\pi}{2}$
3	$E_{D3}^{(1,2)}(\theta) = e^{jk d \cos(\gamma-\theta)} [R_{D3}^{(1)}(\theta) + R_{D3}^{(2)}(\theta)]$	$-\frac{\pi}{2} < \theta < \pi$
4	$E_{D4}^{(1,2)}(\theta) = e^{-jk d \cos(\pi-\gamma-\theta)} [R_{D4}^{(1)}(\theta) + R_{D4}^{(2)}(\theta)]$	$-\pi < \theta < \frac{\pi}{2}$
5	$E_{D5}^{(1)}(\theta) = e^{jk d \cos(\pi-\gamma-\theta)} [R_{D5}^{(1)}(\theta)]$	$0 < \theta < \frac{3\pi}{2}$
6	$E_{D6}^{(1)}(\theta) = e^{-jk d \cos(\gamma-\theta)} [R_{D6}^{(1)}(\theta)]$	$-\frac{3\pi}{2} < \theta < 0$

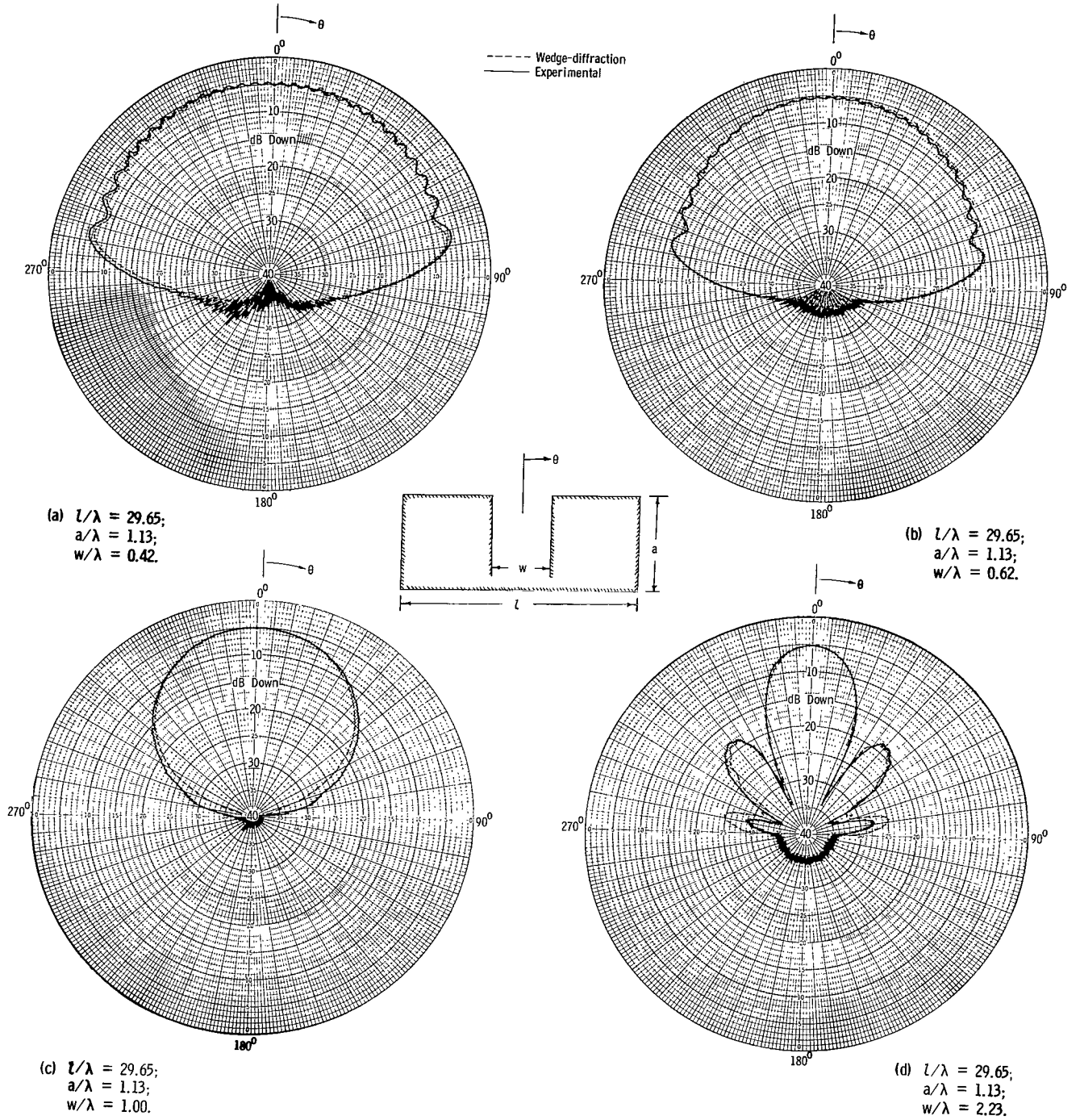


Figure 24.- Elevation-plane patterns of finite-length cylinder (TEM mode).

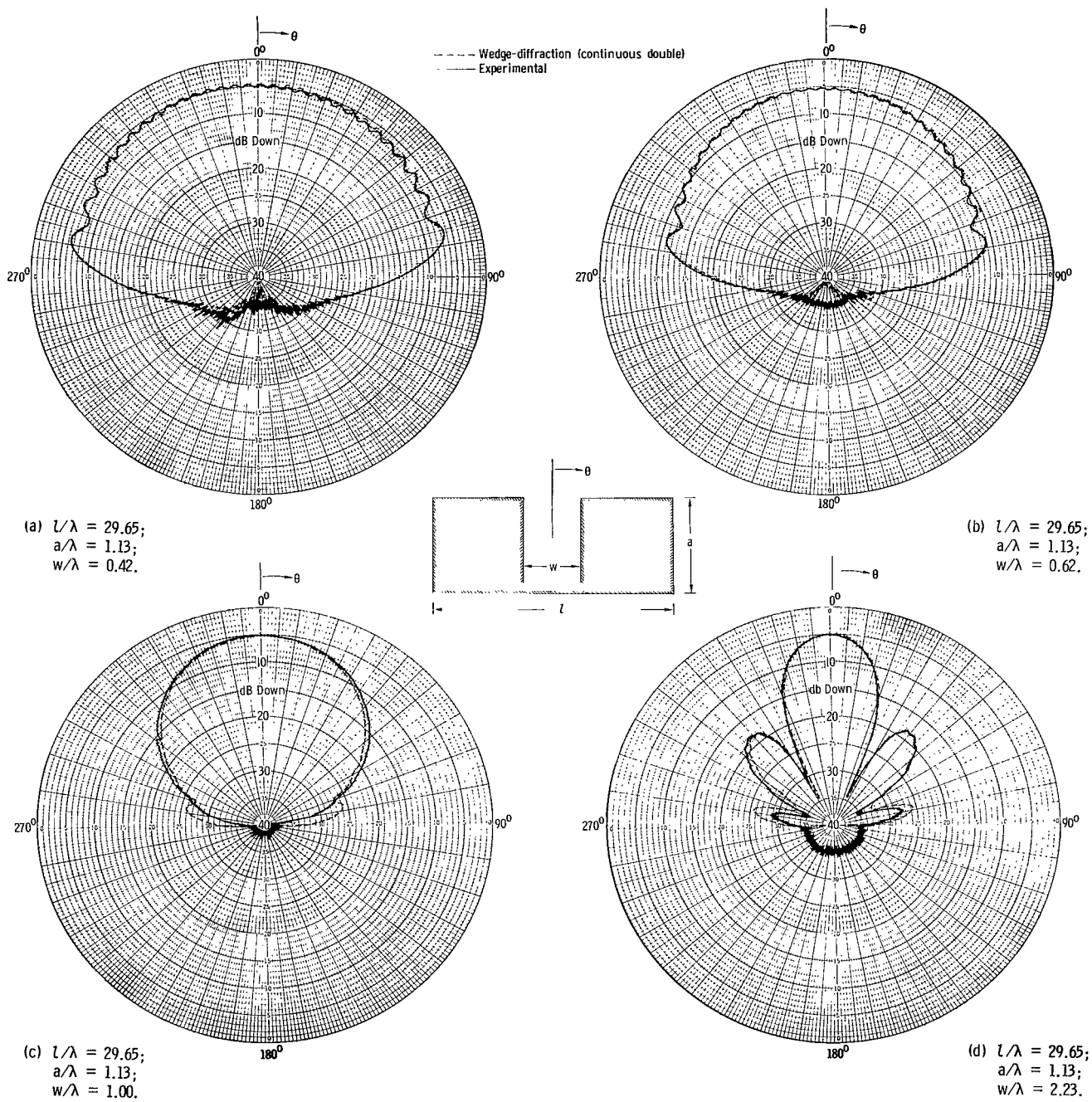


Figure 25.- Elevation-plane patterns of finite-length cylinder using continuous double diffractions (TEM mode).

ELLIPTICAL CYLINDER RADIATION

Flush-mounted antennas are commonly used on space vehicles, missiles, and aircraft. However, their radiation properties usually cannot be predicted analytically because the geometric shape of the body to which they are mounted does not conform to a coordinate system where the wave equation is separable. The method used to analyze the radiation properties of axial slots on circular conducting cylinders can be applied to cylindrical-shaped bodies of arbitrary convex cross section. One geometry of wide interest is an elliptical cylinder which can be used as an approximate model for the wings of an aircraft or the fins of a missile.

The far-field radiation produced by a slot of arbitrary shape on the surface of an elliptical cylinder of infinite length using modal solutions has been carried out by Wait (ref. 5). Computations using the modal solution are numerically convenient only for very thin-shaped elliptical cylinders, and as the size increases (larger ka and kb) higher-order terms must also be included for convergence. However, the analysis using wedge diffraction and creeping wave theory can be used for computations of any size and shape of an elliptical cylinder. As the physical dimensions increase, the accuracy of the obtained data increases because diffraction coefficients D_{mh} and decay constants α_{mh} used in the analysis are derived from asymptotic series of canonical boundary-value problems for $\lambda \rightarrow 0$.

Equatorial-Plane Pattern of Axial Slots Operating in TEM Mode

The two-dimensional geometry for an axial slot mounted on an elliptical cylinder is similar to that for a slot on the circular cylinder and is shown in figure 26 for the TEM mode. The junctions formed by the walls of the parallel-plate waveguide and the planes tangent to the surface of the cylinder at the edge points are approximated by a pair of infinite wedges of finite included angle $WA = (2 - n)\pi$. The wedge-diffracted field is given by equation (61) and is repeated here as follows:

$$E_D(r_0, \phi_0) = \frac{e^{-j\left[k\left(r_0 - \frac{w}{2}\sin\phi\right) + \frac{\pi}{4}\right]}}{\sqrt{2\pi kr_0}} \left[R_1(\phi_0) + R_2(\phi_0)e^{-jkw\sin\phi_0} \right]$$

With the use of the far-field approximations

$$r_0 \approx r - \tau_0 \cos\phi \cos\beta \tag{99}$$

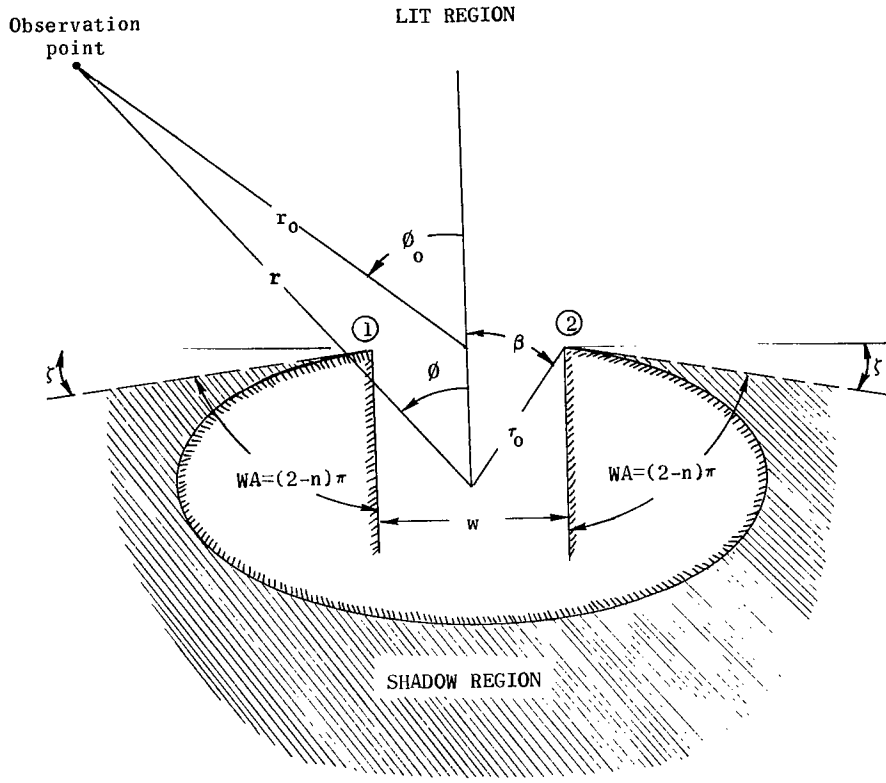


Figure 26.- Lit and shadow regions for elliptical cylinder.

for phase terms and

$$r_0 \approx r \quad (100)$$

for amplitude terms with

$$\phi_0 \approx \phi \quad (101)$$

this equation (eq. (61)) reduces to

$$E_D(r, \phi) = \frac{1}{\sqrt{2\pi k}} \frac{e^{-jkr}}{\sqrt{r}} e^{j \left[k \left(\frac{w}{2} \sin \phi + \tau_0 \cos \phi \cos \beta \right) - \frac{\pi}{4} \right]} \left[R_1(\phi) + R_2(\phi) e^{-jkw \sin \phi} \right] \quad (102)$$

where

$$\tau_0 = \sqrt{x_0^2 + y_0^2} \quad (103)$$

$$x_o = \pm \frac{w}{2} \quad (104)$$

$$y_o = \frac{b}{2a} \sqrt{4a^2 - w^2} \quad (105)$$

with $R_1(\phi)$ and $R_2(\phi)$ as defined by equations (38) and (34).

The creeping-wave field is given by equation (60) and is repeated here as follows:

$$\begin{aligned} E_C(s, \phi) = & R_A \frac{D_{oh}(P_1)}{D_{oh}(Q_1)} \frac{e^{-jk(t_1+s_1)}}{\sqrt{s_1}} e^{-\int_0^{t_1} \alpha_{oh}(\rho) ds} \\ & + R_B \frac{D_{oh}(P_2)}{D_{oh}(Q_2)} \frac{e^{-jk(t_2+s_2)}}{\sqrt{s_2}} e^{-\int_0^{t_2} \alpha_{oh}(\rho) ds} \end{aligned}$$

From the geometry of figure 27, the following far-field approximations may be obtained:

$$\tau_1 \approx \tau_2 \approx \tau \quad (106)$$

$$\delta_2 \approx \pi - \delta_1 \quad (107)$$

and

$$\left. \begin{aligned} s_1 &\approx r - \tau \cos \delta_1 \\ s_2 &\approx r + \tau \cos \delta_1 \end{aligned} \right\} \quad (108)$$

for phase terms and

$$s_1 \approx s_2 \approx r \quad (109)$$

for amplitude terms. Equation (60) then reduces to

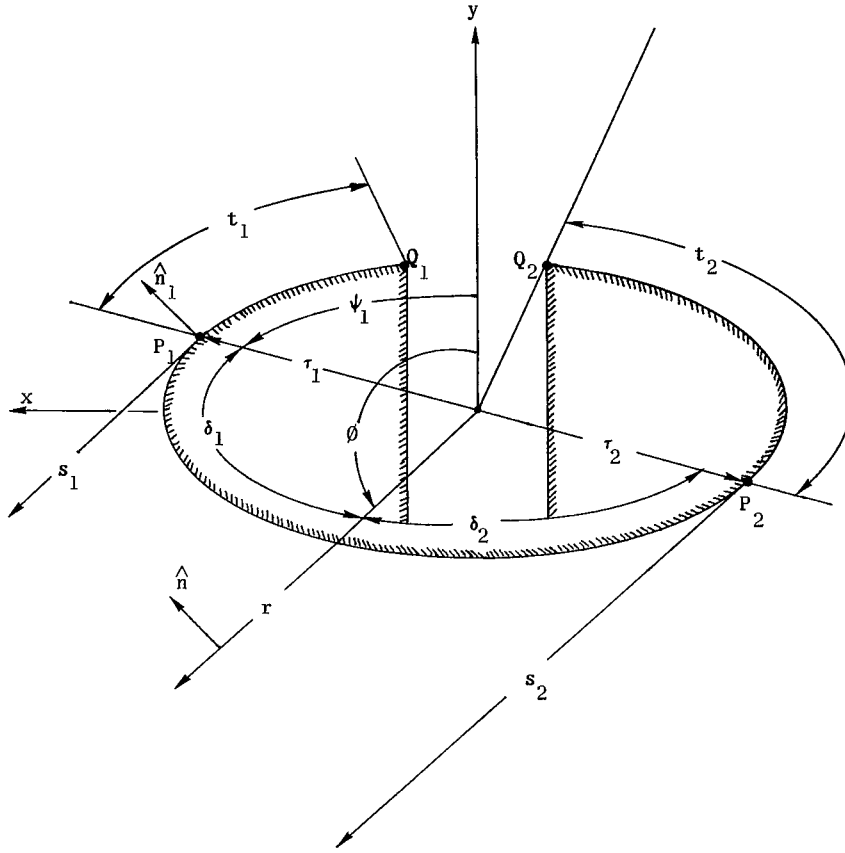


Figure 27.- Far-zone creeping-wave field coordinates.

$$E_C(r, \phi) = P_A \frac{e^{-jkr}}{\sqrt{r}} e^{-jkt_1} e^{-\int_0^{t_1} \alpha_{oh}(\rho) ds} + P_B \frac{e^{-jkr}}{\sqrt{r}} e^{-jkt_2} e^{-\int_0^{t_2} \alpha_{oh}(\rho) ds} \quad (110)$$

where

$$P_A = R_A \frac{D_{oh}(P_1)}{D_{oh}(Q_1)} e^{jk\tau \cos \delta_1} \quad (111)$$

$$P_B = R_B \frac{D_{oh}(P_2)}{D_{oh}(Q_2)} e^{-jk\tau \cos \delta_1} \quad (112)$$

$$R_A = \frac{\sqrt{r}}{e^{-jkr}} E_D \left[r, +\left(\frac{\pi}{2} + \zeta\right) \right] = E_i(Q_1) \left[D_{oh}(Q_1) \right]^2 \quad (113)$$

$$R_B = \frac{\sqrt{r}}{e^{-jkr}} E_D \left[r, -\left(\frac{\pi}{2} + \zeta\right) \right] = E_i(Q_2) \left[D_{oh}(Q_2) \right]^2 \quad (114)$$

with E_D being obtained from equation (102).

Expressions for the radius of curvature and differential arc length for an ellipse can be obtained by applying the basic geometric definitions of each

$$ds = \sqrt{(dx)^2 + (dy)^2} \quad (115)$$

$$\rho = \frac{[1 + (y')^2]^{3/2}}{|y''|} \quad (116)$$

$$x = \tau \sin \phi \quad (117)$$

$$y = \tau \cos \phi \quad (118)$$

Using equations (115), (117), and (118) leads to

$$dx = \tau \cos \phi d\phi + \sin \phi d\tau \quad (119)$$

$$dy = -\tau \sin \phi d\phi + \cos \phi d\tau \quad (120)$$

$$ds = \left[\tau^2 (d\phi)^2 + (d\tau)^2 \right]^{1/2} \quad (121)$$

$$y' = -\left(\frac{b}{a}\right)^2 \frac{\sin \phi}{\cos \phi} \quad (122)$$

$$y'' = \frac{b}{a^5} \frac{(a^2 \cos^2 \phi + b^2 \sin^2 \phi)^{3/2}}{\cos^3 \phi} \quad (123)$$

Substituting equations (117) and (118) into the equation for an ellipse in rectangular coordinates

$$\frac{x^2}{a^2} + \frac{y^2}{b^2} = 1 \quad (124)$$

leads to

$$\tau = \frac{ab}{(a^2 \cos^2 \phi + b^2 \sin^2 \phi)^{1/2}} \quad (125)$$

$$d\tau = \frac{ab(a^2 - b^2) \sin \phi \cos \phi}{(a^2 \cos^2 \phi + b^2 \sin^2 \phi)^{3/2}} d\phi \quad (126)$$

Substitution of equations (122) and (123) into equation (116) and of equations (125) and (126) into equation (121) yields

$$\rho = \frac{1}{ab} \left(\frac{a^4 \cos^2 \phi + b^4 \sin^2 \phi}{a^2 \cos^2 \phi + b^2 \sin^2 \phi} \right)^{3/2} \quad (127)$$

$$ds = ab \frac{(a^4 \cos^2 \phi + b^4 \sin^2 \phi)^{1/2}}{(a^2 \cos^2 \phi + b^2 \sin^2 \phi)^{3/2}} d\phi \quad (128)$$

The arc length and complex attenuation factor of the creeping wave on the elliptic surface can then be expressed as

$$t = \int_{\phi_{11}}^{\phi_{12}} ds = ab \int_{\phi_{11}}^{\phi_{12}} \frac{(a^4 \cos^2 \phi + b^4 \sin^2 \phi)^{1/2}}{(a^2 \cos^2 \phi + b^2 \sin^2 \phi)^{3/2}} d\phi \quad (129)$$

$$\int_0^t \alpha_{oh}(\rho) ds = \frac{(k)^{1/3}}{2} \left(\frac{3\pi ab}{4} \right)^{2/3} e^{j\frac{\pi}{6}} \int_{\phi_{11}}^{\phi_{12}} \frac{ab d\phi}{\left[(a^4 \cos^2 \phi + b^4 \sin^2 \phi)(a^2 \cos^2 \phi + b^2 \sin^2 \phi) \right]^{1/2}} \quad (130)$$

where

ϕ_{11} trapping point angle of creeping wave

ϕ_{12} exit point angle of creeping wave

The points of trapping, Q_1 and Q_2 , are given by equations (104) and (105). To determine the points of reradiation, P_1 and P_2 , of each creeping wave on the surface of the elliptical cylinder, the vector cross product will be utilized (ref. 24). As shown in figure 27 for the observation angle ϕ with far-field observations being assumed

$$\hat{n} \times \hat{n}_1 = 0 \quad (131)$$

where

$$\hat{n} = -\hat{x} \cos \phi + \hat{y} \sin \phi = \text{Unit vector perpendicular to line from origin of cylinder to observation point} \quad (132)$$

$$\hat{n}_1 = \frac{\hat{x} \frac{x}{a^2} + \hat{y} \frac{y}{b^2}}{\left[\left(\frac{x}{a^2} \right)^2 + \left(\frac{y}{b^2} \right)^2 \right]^{1/2}} = \text{Unit vector normal to cylinder surface at point of tangency} \quad (133)$$

Applying equation (131) and using the equation for an ellipse in rectangular coordinates

$$\frac{x^2}{a^2} + \frac{y^2}{b^2} = 1$$

lead to, for reradiation point P_1 ,

$$\left. \begin{aligned} x_1(P_1) &= \frac{-a^2 \cos \phi}{(a^2 \cos^2 \phi + b^2 \sin^2 \phi)^{1/2}} \\ y_1(P_1) &= \frac{b^2 \sin \phi}{(a^2 \cos^2 \phi + b^2 \sin^2 \phi)^{1/2}} \\ \psi_1 &= \tan^{-1} \frac{x_1(P_1)}{y_1(P_1)} \end{aligned} \right\} \quad (134)$$

and, for reradiation point P_2 ,

$$\left. \begin{aligned} x_2(P_2) &= \frac{a^2 \cos \phi}{(a^2 \cos^2 \phi + b^2 \sin^2 \phi)^{1/2}} \\ y_2(P_2) &= \frac{-b^2 \sin \phi}{(a^2 \cos^2 \phi + b^2 \sin^2 \phi)^{1/2}} \end{aligned} \right\} \quad (135)$$

The angles β and ζ are given by

$$\beta = \tan^{-1} \left(\frac{a}{b} \frac{w}{\sqrt{4a^2 - w^2}} \right) \quad (136)$$

$$\zeta = \tan^{-1} \left(\frac{b}{a} \frac{w}{\sqrt{4a^2 - w^2}} \right) \quad (137)$$

The wedge-diffracted and creeping-wave fields, with the $e^{-jkr/\sqrt{r}}$ factor being suppressed, are given by

$$E_D(\phi) = \frac{1}{\sqrt{2\pi k}} e^{j \left[k \left(\frac{w}{2} \sin \phi + \tau_0 \cos \phi \cos \beta \right) - \frac{\pi}{4} \right]} \left(R_1 + R_2 e^{-jkw \sin \phi} \right) \quad (138)$$

$$E_C(\phi) = P_A e^{-jkt_1} e^{-\int_0^{t_1} \alpha_{oh}(\rho) ds} + P_B e^{-jkt_2} e^{-\int_0^{t_2} \alpha_{oh}(\rho) ds} \quad (139)$$

$$t_1 = \int_{\phi_{11}}^{\phi_{12}} ds \quad (140)$$

$$t_2 = \int_{\phi_{21}}^{\phi_{22}} ds \quad (141)$$

In general, the total field is given by

$$E_T(\phi) = E_D(\phi) + E_C(\phi) \quad (142)$$

where the appropriate fields must be considered in each region as shown in table III.

TABLE III - WEDGE-DIFFRACTED AND CREEPING-WAVE FIELDS FOR EQUATORIAL-PLANE PATTERN OF ELLIPTICAL CYLINDER IN DIFFERENT REGIONS

	Wedge-diffracted field, $E_D(\phi)$	Creepling-wave field, $E_C(\phi)$	ϕ_{11} ϕ_{12}	ϕ_{21} ϕ_{22}
Region I $0 < \phi \leq \frac{\pi}{2} - \zeta$	$\frac{j \left[k \left(\frac{w}{2} \sin \phi + \tau_0 \cos \phi \cos \beta \right) - \frac{\pi}{4} \right]}{\sqrt{2\pi k}} (R_1 + R_2 e^{-jkw \sin \phi})$	$P_A e^{-jkt_1} e^{-\int_0^{t_1} \alpha_{oh}(\rho) ds} + P_B e^{-jkt_2} e^{-\int_0^{t_2} \alpha_{oh}(\rho) ds}$	$\phi_{11} = \beta$ $\phi_{12} = 2\pi + \psi_1$	$\phi_{21} = -(\pi - \psi_1)$ $\phi_{22} = -\beta$
Region II $\frac{\pi}{2} - \zeta < \phi \leq \frac{\pi}{2}$	$\frac{j \left[k \left(\frac{w}{2} \sin \phi + \tau_0 \cos \phi \cos \beta \right) - \frac{\pi}{4} \right]}{\sqrt{2\pi k}} (R_1 + R_2 e^{-jkw \sin \phi})$	$P_B e^{-jkt_2} e^{-\int_0^{t_2} \alpha_{oh}(\rho) ds}$	-----	$\phi_{21} = -(\pi - \psi_1)$ $\phi_{22} = -\beta$
Region III $\frac{\pi}{2} < \phi \leq \frac{\pi}{2} + \zeta$	$\frac{j \left[k \left(\frac{w}{2} \sin \phi + \tau_0 \cos \phi \cos \beta \right) - \frac{\pi}{4} \right]}{\sqrt{2\pi k}} (R_1)$	$P_B e^{-jkt_2} e^{-\int_0^{t_2} \alpha_{oh}(\rho) ds}$	-----	$\phi_{21} = -(\pi - \psi_1)$ $\phi_{22} = -\beta$
Region IV $\frac{\pi}{2} + \zeta < \phi \leq \pi$	0	$P_A e^{-jkt_1} e^{-\int_0^{t_1} \alpha_{oh}(\rho) ds} + P_B e^{-jkt_2} e^{-\int_0^{t_2} \alpha_{oh}(\rho) ds}$	$\phi_{11} = \beta$ $\phi_{12} = \psi_1$	$\phi_{21} = -(\pi - \psi_1)$ $\phi_{22} = -\beta$

Radiation patterns computed by using the fields from table III in their respective regions are shown in figures 28 to 30. Experimental models were constructed and the obtained data were used for comparison since boundary-value solutions are numerically convenient only for very thin elliptical cylinder. Harrington (ref. 4) points out that the equatorial radiation pattern ($\theta = 90^\circ$ plane) for a circular cylinder with finite axial slot is identical to that for a circular cylinder with an infinite axial slot. It is assumed that such a relation holds for an elliptical cylinder, and the experimental results were obtained by using finite axial slots. The experimental models were also of finite length of about 30 wavelengths; diffractions from the edges of the cylinders should then be negligible. Dimension construction accuracies were within $\pm\lambda/25$ and surface irregularities within $\pm\lambda/50$. All measurements were performed at a frequency of about 10 GHz.

The agreement between computed and experimental patterns is good particularly in the forward hemisphere. Errors of the order of 2 to 3 dB are obtained in the penumbra region and they indicate that further improvement could be made on the approximations of the parallel-plate—cylinder geometry by a wedge and on those implicit in equations (113) and (114). The use of the half-plane wall for certain diffraction processes would yield improved results near the penumbra region as has been discussed previously for the circular cylinder. In general, the errors in the shadow region are of the same order of magnitude, and they are quite acceptable for determining possible interference and noise that might be introduced from other systems through these back lobes.

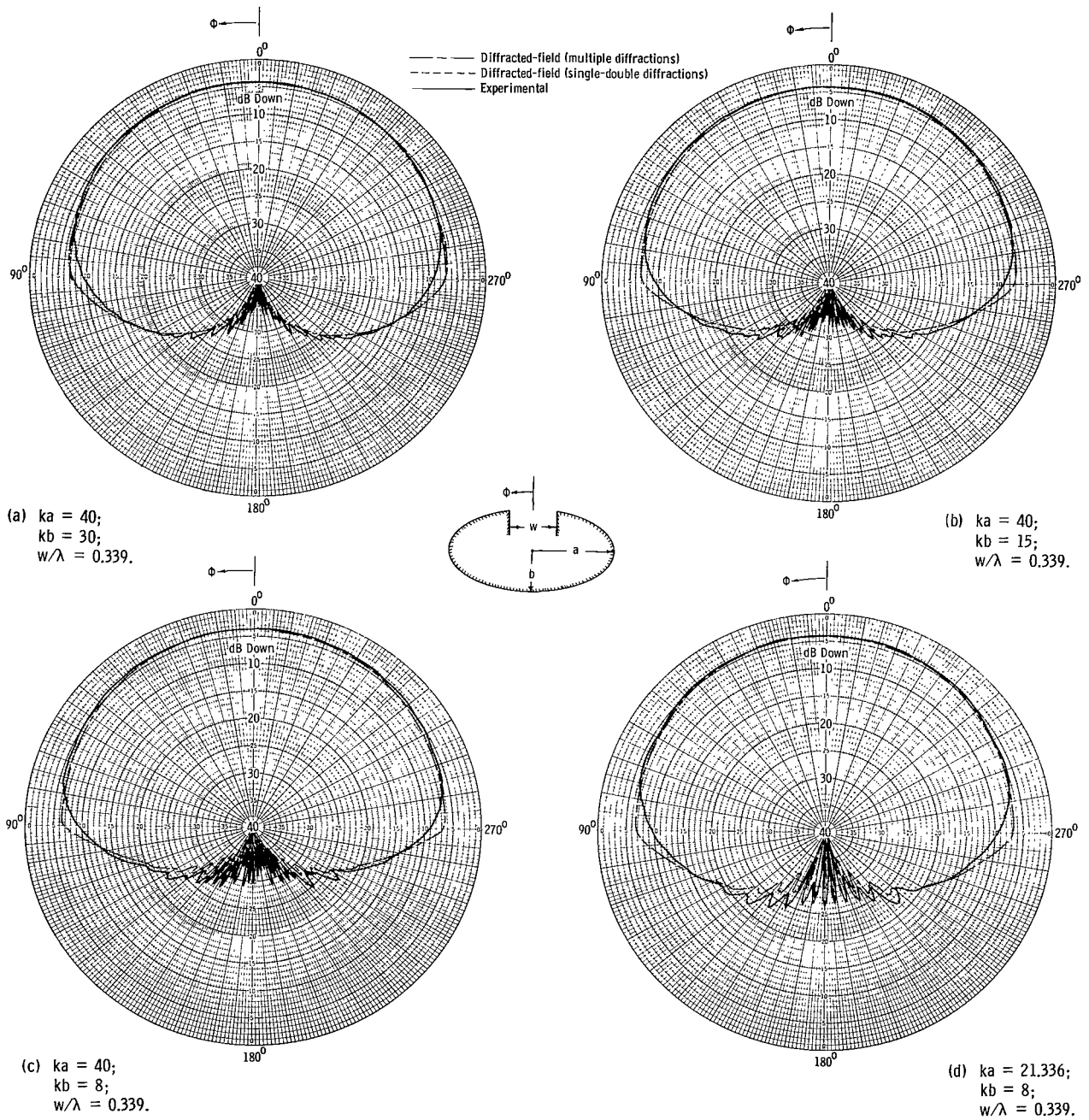


Figure 28.- Radiation patterns of axial infinite slot on elliptical conducting cylinder using finite wedges (TEM mode).

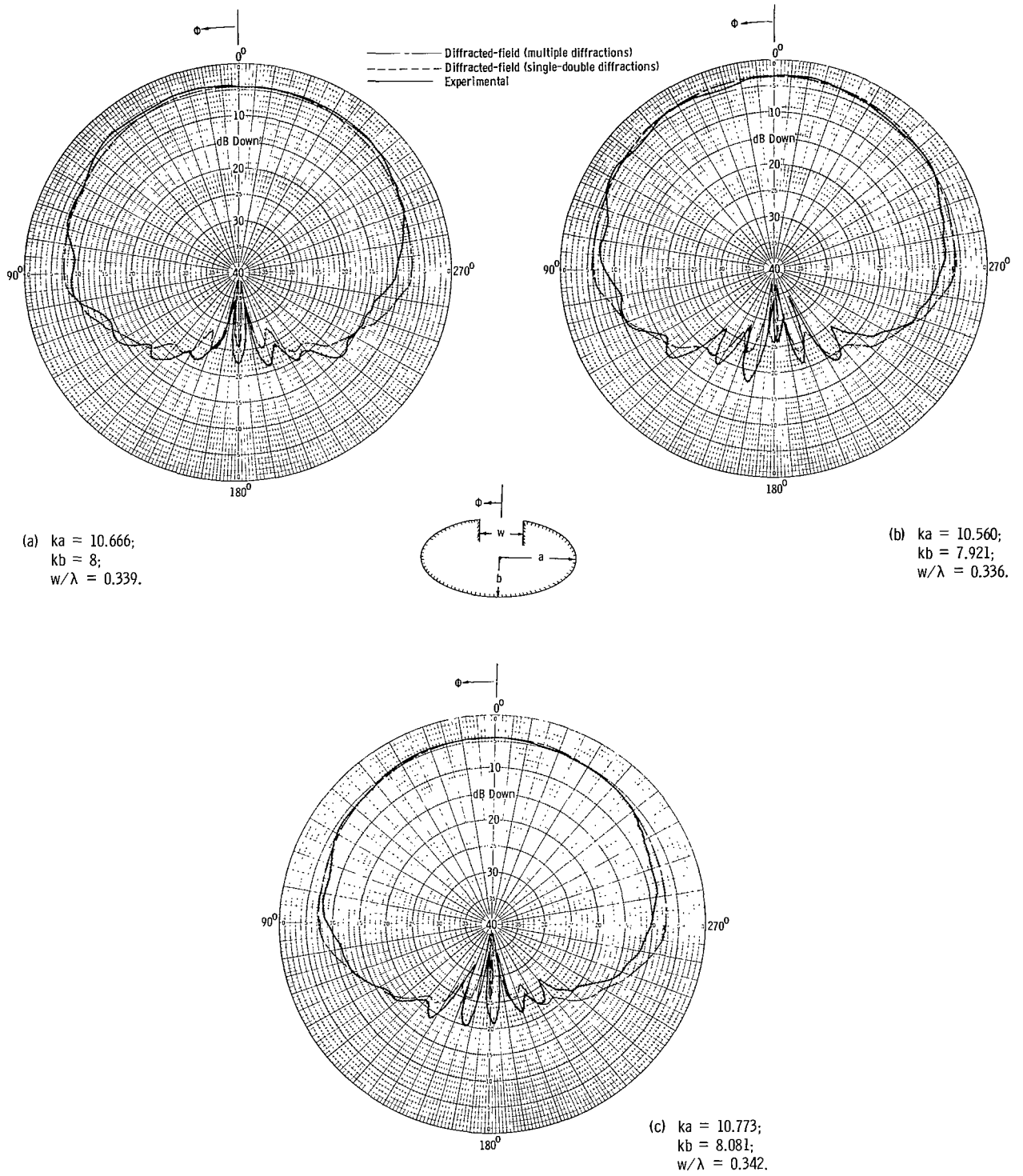


Figure 29.- Comparison of radiation patterns for smaller size elliptical cylinder (TEM mode).

For elliptical cylinders with constant major axis but decreasing minor axis (thinner shape ellipse), the rate of attenuation of the creeping waves, whose main contribution is in the shadow region, is larger. However, the lit-region radiation, whose primary source is the wedge-diffracted fields, is essentially unaffected as shown in figures 28(a) to (c). The creeping-wave fields are strongly influenced by the radius of curvature which is rapidly changing whereas the wedge-diffracted fields depend on the included angle of the wedges WA which remains essentially constant.

For the small elliptical cylinder ($ka = 10.666$, $kb = 8$) of figure 29(a), slightly larger variations and asymmetries between experiment and theory are noted. For ± 1.0 percent changes in frequency (figs. 29(b) and (c)), the variations and asymmetries are even greater and it is believed that the physical construction tolerances of the elliptical cross section are critical for the measurements on this size body. For a thin elliptical cylinder the radius of curvature of the surface near the major axis is small and any diffractions from that region would not be very accurate since the asymptotic series assumption of large physical dimensions is not well satisfied.

In figure 30, the experimental pattern of a thin elliptical cylinder ($ka = 40$, $kb = 8$) is compared with a theoretical curve of a finite-size ground plane obtained by using wedge diffraction techniques. A good agreement is noted in the $90^\circ < \phi < -90^\circ$ region. However, in the $90^\circ > \phi > -90^\circ$ region the ripples predicted by the computed curve of the ground plane do not appear in the experimental curve for the thin elliptical cylinder. The surface of the cylinder is smooth and has no sharp edges to contribute diffractions in the lit region for the ripples to appear. The fact that edge-diffracted fields do disturb the pattern is interesting to the antenna designer who would certainly prefer the smooth pattern. Cylindrical caps on the sides of the ground plane would reduce the ripples and smooth the pattern.

To check the validity of the half-plane ($n = 2$) approximation for the parallel-plate—cylinder geometry instead of a finite wedge ($n \neq 2$), equations (138) and (139) were used with modified n 's and the computed results were compared with experimental results. It was found by comparison, like for the circular cylinder, that the best approximation was to replace the edge ① geometry by a half-plane ($n = 2$) for the first-order diffraction and by a finite wedge ($n \neq 2$) for second- and higher-order diffractions for the 0° to 180° pattern measured in the counterclockwise direction. The edge ② geometry was replaced by a finite wedge for all orders of diffraction. For the 180° to 360° pattern, the approximations of edge ① geometry are valid for edge ② and vice versa.

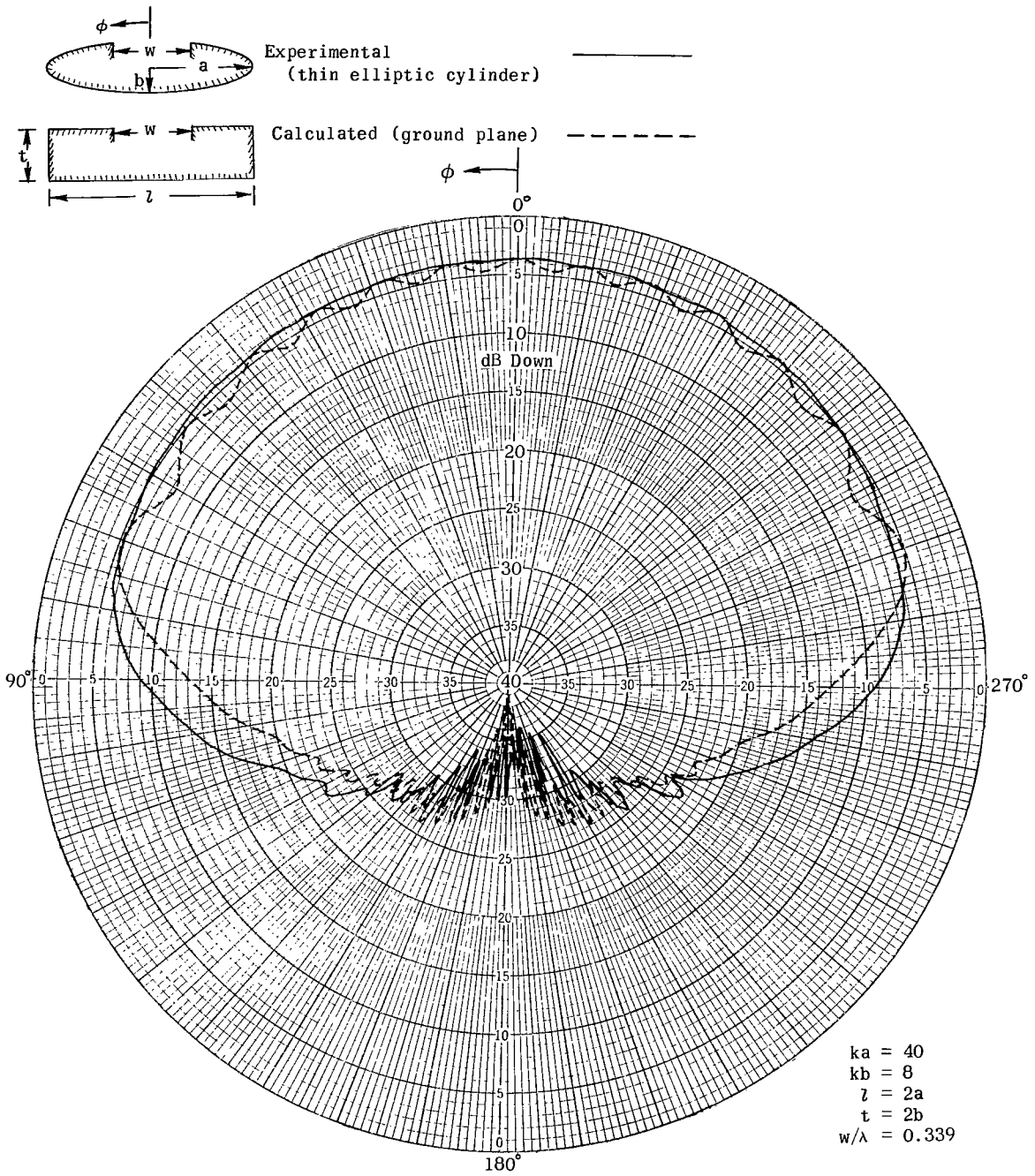


Figure 30.- Radiation pattern of a thin elliptical cylinder and a finite-size ground plane (TEM mode).

The computed results using the half-plane and finite-wedge approximation are shown in figure 31, where they are compared with the experimental curves. It is seen that these approximations result in better accuracies in the penumbra region than the finite wedge approximation but larger variations exist in all other regions. As concluded previously, the solution used then depends on the region of space of interest. It should be noted that computed results for single-double diffractions and multiple diffractions shown in figures 28, 29, and 31 are almost the same, and it is rather difficult to distinguish any variations between the two.

Equatorial-Plane Pattern of Circumferential Slots Operating in TE₁₀ Mode

As was explained previously, the TE₁₀ mode is represented by two plane TEM mode waves reflecting obliquely back and forth between the waveguide walls with the electric field being parallel to the edge of the walls. The finite-wedge approximation for the parallel-plate—cylinder geometry will not satisfy the boundary conditions and the half-plane approximation will be used.

For a circumferential slot operating in the TE₁₀ mode and mounted on a circular cylinder it was found that the best approximation was to replace edge ① by a half-plane ($n = 2$) for the first-order diffraction and by a finite wedge ($n \neq 2$) for the second- and higher-order diffractions for the 0° to 180° pattern measured in the counterclockwise direction. The edge ② geometry was replaced by a finite wedge for all orders of diffraction. For the 180° to 360° pattern, the approximations of edge ① geometry are valid for edge ② and vice versa.

This approximation is also used for the elliptical cylinder. The wedge-diffracted field is given by equations (73) to (75) with n modified as explained previously. The creeping-wave field is given by

$$E_C(\phi) = P_A e^{-jkt_1} e^{-\int_0^{t_1} \alpha_{os}(\rho) ds} + P_B e^{-jkt_2} e^{-\int_0^{t_2} \alpha_{os}(\rho) ds} \quad (143)$$

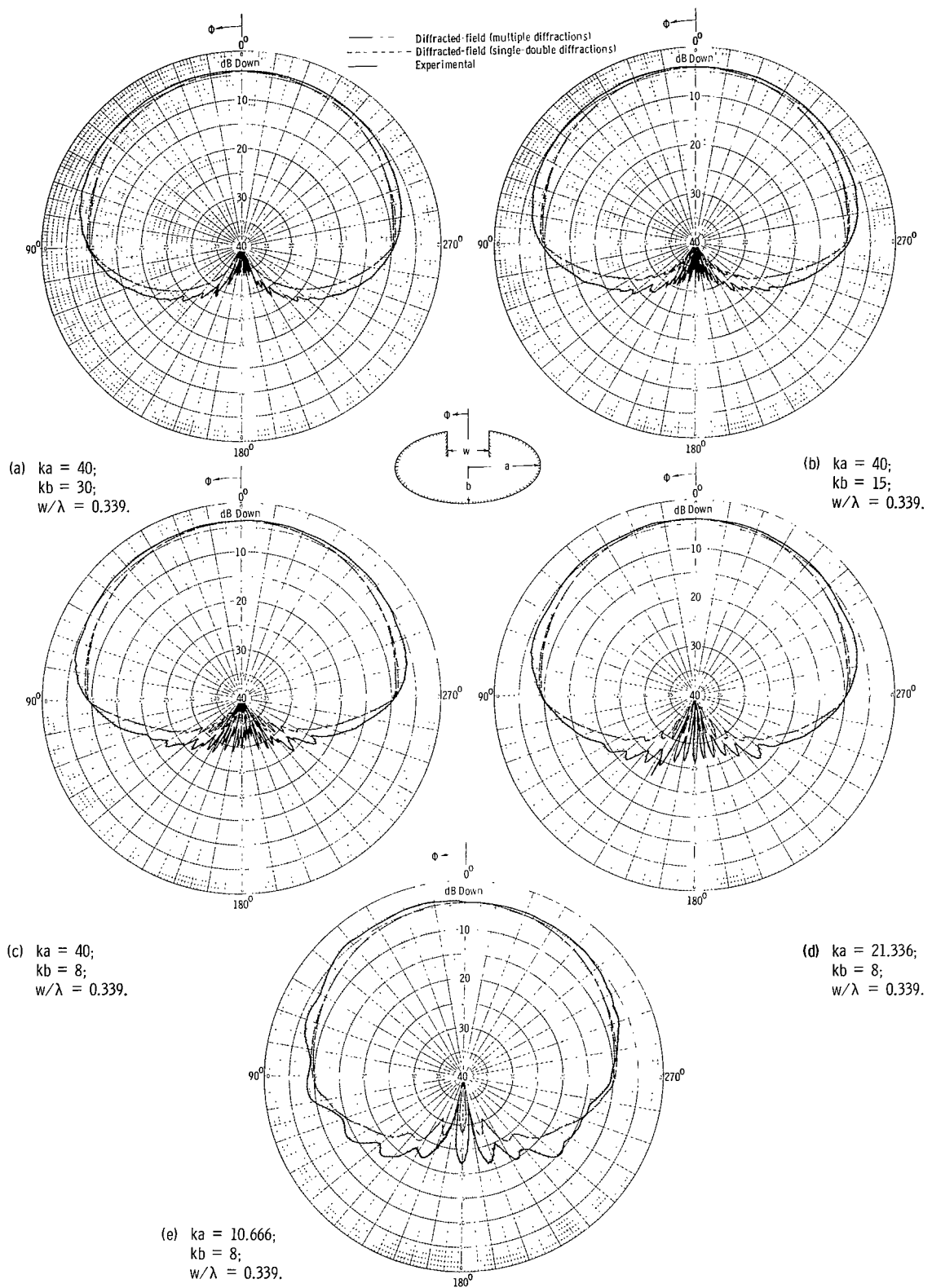


Figure 31.- Radiation patterns of axial slot on elliptical conducting cylinder using half-plane and finite wedges (TEM model).

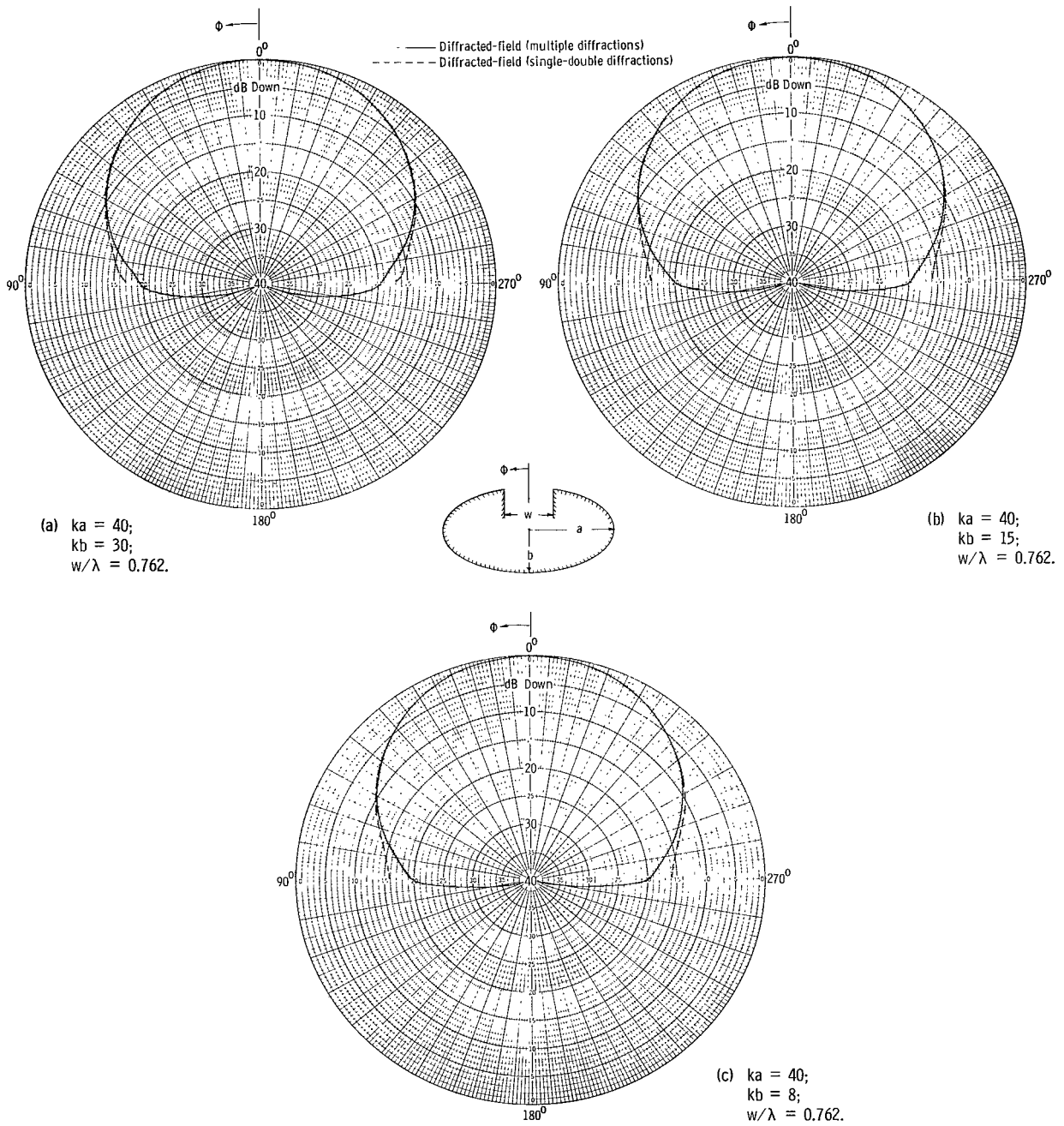


Figure 32.- Radiation patterns of circumferential slot on elliptical conducting cylinder using half-plane and finite wedges (TE_{10} mode).

where

$$\int_0^t \alpha_{os}(\rho) ds = \frac{k^{1/3}}{2} \left(\frac{9\pi ab}{4} \right)^{2/3} e^{j\frac{\pi}{6}} \int_{\phi_{11}}^{\phi_{12}} \frac{ab d\phi}{\left[(a^4 \cos^2 \phi + b^4 \sin^2 \phi)(a^2 \cos^2 \phi + b^2 \sin^2 \phi) \right]^{1/2}} \quad (144)$$

The regions where the appropriate wedge-diffracted and creeping-wave fields are applicable are identical to those shown in table III for the TEM mode.

The computed results for the TE₁₀ mode slot on an elliptical cylinder are shown in figure 32. As for the circular cylinder, the single-double diffraction solution has a discontinuity in the $\phi = \pm 90^\circ$ directions because higher-order diffractions are neglected. The thin-walled guide approximation ($n = 2$ for all orders of diffraction) could also be used as was demonstrated for the circular cylinder. Good results would also be obtained in this case.

CONCLUDING REMARKS

Wedge diffraction and creeping wave theories have been used to analyze the radiation properties of slots on cylindrical bodies. By using this technique, the computed patterns for circular and elliptical cylinders have been favorably compared with existing modal solutions and experimental results.

The concept of a hybrid solution utilizing wedge diffraction and creeping wave theories has been established in solving aperture antenna problems on cylindrical bodies that have not been considered previously from this point of view. The first attempt was to apply this technique to a circular cylinder with a known boundary-value solution for comparison of the results. It was then extended to a more complicated geometry such as the elliptical cylinder where the computations using the boundary-value solution are not very convenient but where experimental data are available. Radiation properties of finite-size cylinders were also analyzed and the contribution to the overall pattern from the edges was taken into account.

Once a good understanding of the radiation mechanism is established, the technique can now be extended to other more complex geometries to include slots on spheres, prolate spheroids, and ogives. Problems involving dipoles on the surface of such geometric shapes should also be considered. Experimental data and modern computational

methods such as the point-matching boundary-value technique should be used in combination with the geometrical theory of diffraction to obtain improved values and gain better understanding of the radiation mechanisms involved.

Langley Research Center,
National Aeronautics and Space Administration,
Langley Station, Hampton, Va., November 13, 1969.

APPENDIX

DIFFRACTION BY A PERFECTLY CONDUCTING WEDGE

Consider a two-dimensional wedge and a line source to be situated in space as shown in figure 33. The faces of the wedge are formed by two semi-infinite intersecting planes. The infinitely long line source is parallel to the edge of the wedge, and its position is described by the coordinate (r_0, ψ_0) . The typical field point is denoted by (r, ψ) . The line source is assumed to have unit strength and time dependence of the form $e^{j\omega t}$. The Green's function for this radiating system can be written as (ref. 19)

$$G = \frac{1}{n} \sum_{m=0}^{\infty} \epsilon_m \frac{J_m(kr)}{n} \frac{H_m^{(2)}(kr_0)}{n} \left[\cos \frac{m}{n}(\psi - \psi_0) \pm \cos \frac{m}{n}(\psi + \psi_0) \right] \quad (145)$$

if $r_0 > r$. For the case $r_0 < r$, r and r_0 are interchanged. In this expression ϵ_m is the Neumann number which is equal to 1 if m is 0; otherwise it is equal to 2. The plus sign between the two cosine terms is used if the boundary condition is of the homogeneous Neumann type $\left(\frac{\partial G}{\partial \psi} = 0\right)$ on both faces of the wedge. For the homogeneous Dirichlet boundary condition ($G = 0$ on both faces of the wedge), the minus sign is used.

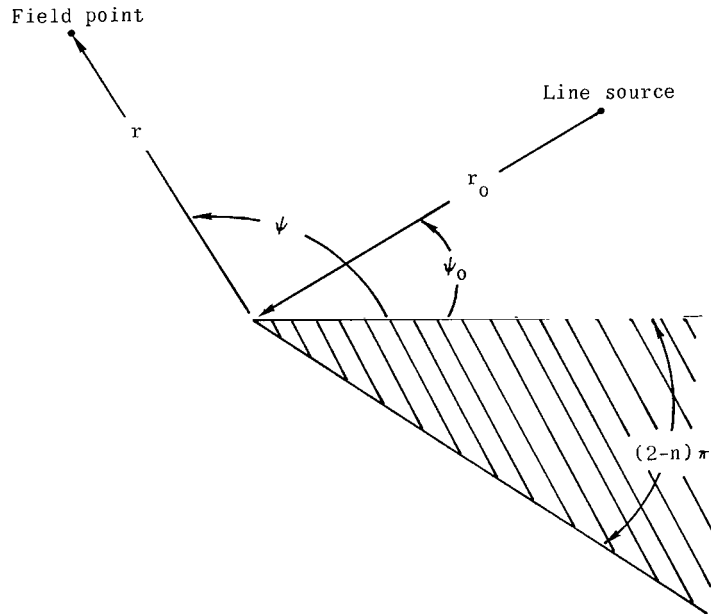


Figure 33.- Line source and diffracting wedge.

APPENDIX

This convergent series is an exact solution to the time harmonic, inhomogeneous wave equation for the problem of a radiating line source and wedge embedded in a linear, isotropic, homogeneous, lossless medium.

Many times it is necessary to determine the total radiation field when the line source is far removed from the vertex of the wedge. In such cases, equation (145) can be simplified by replacing the Hankel function by the first term of its asymptotic expansion, that is, by the relation

$$H_{\frac{m}{n}}^{(2)}(kr_0) \sim \sqrt{\frac{2}{\pi kr_0}} e^{-j\left(kr_0 - \frac{\pi}{4} - \frac{m}{n} \frac{\pi}{2}\right)} \quad (146)$$

This substitution reduces G to the form

$$\begin{aligned} G &= \sqrt{\frac{2}{\pi kr_0}} e^{-j\left(kr_0 - \frac{\pi}{4}\right)} \frac{1}{n} \sum_{m=0}^{\infty} \epsilon_m J_{\frac{m}{n}}(kr) e^{+j\frac{m}{n} \frac{\pi}{2}} \left[\cos \frac{m}{n}(\psi - \psi_0) \pm \cos \frac{m}{n}(\psi + \psi_0) \right] \\ &= \sqrt{\frac{2}{\pi kr_0}} e^{-j\left(kr_0 - \frac{\pi}{4}\right)} E \end{aligned} \quad (147)$$

where

$$E = E_D + E_G = \frac{1}{n} \sum_{m=0}^{\infty} \epsilon_m J_{\frac{m}{n}}(kr) e^{j\frac{m}{n} \frac{\pi}{2}} \left[\cos \frac{m}{n}(\psi - \psi_0) \pm \cos \frac{m}{n}(\psi + \psi_0) \right] \quad (148)$$

with E_D and E_G being the total diffracted and geometrical optics fields, respectively, and E , the series form of the Green's function describing the total field created by the diffraction of a plane wave by a wedge.

An asymptotic expansion for E in inverse powers of kr is very useful for computational purposes, because of the slow convergence of equation (148) for large values of kr . In order to derive an asymptotic expression for E by the standard method of steepest descents, it must first be transformed into an integral or integrals of the form

$$\int_c F(z) e^{kr f(z)} dz \quad (149)$$

APPENDIX

and then evaluated for large kr by means of the method of steepest descents. Such a procedure leads to the expression for the diffracted field for a plane wave incident on a wedge of included angle $(2 - n)\pi$ shown in figure 34 to be (ref. 19)

$$E_D(r, \psi, \psi_0, n) = V_B(r, \psi - \psi_0, n) \pm V_B(r, \psi + \psi_0, n) \quad (150)$$

where the plus sign applies for the polarization of the electric field perpendicular to the edge

$$\left(\frac{\partial E}{\partial n}\right)_{\text{wedge}} = 0$$

and the minus sign applies for polarization parallel to the edge

$$E_{\text{wedge}} = 0$$

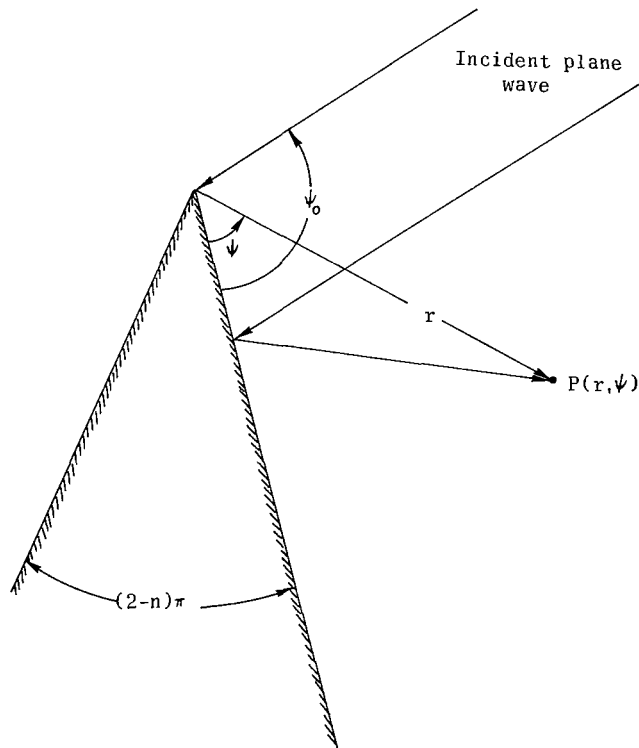


Figure 34.- Diffraction by a wedge of included angle $(2 - n)\pi$.

APPENDIX

The wedge-diffraction function $V_B(r, \psi_{\mp}\psi_0, n)$ for a plane wave has also been determined by Pauli in reference 18.

The form of the diffraction function is defined as

$$V_B(r, \psi_{\mp}\psi_0, n) = I_{-\pi}(r, \psi_{\mp}\psi_0, n) + I_{+\pi}(r, \psi_{\mp}\psi_0, n) \quad (151)$$

where

$$I_{\pm\pi}(r, \psi_{\mp}\psi_0, n) \sim \frac{e^{-j\left(kr + \frac{\pi}{4}\right)}}{jn\sqrt{2\pi}} \sqrt{g} \cot \frac{\pi \pm (\psi_{\mp} \psi_0)}{2n} e^{jkr} \int_{\sqrt{kr}}^{\infty} e^{-j\tau^2} d\tau + \text{Higher-order terms} \quad (152)$$

$$g = 1 + \left[\cos(\psi \pm \psi_0) - 2n\pi N \right] \quad (153)$$

and N is a positive or negative integer or zero which most nearly satisfies the equation

$$\left. \begin{aligned} 2n\pi N - (\psi \pm \psi_0) &= -\pi && \left(\text{for } I_{-\pi} \right) \\ 2n\pi N - (\psi \pm \psi_0) &= +\pi && \left(\text{for } I_{+\pi} \right) \end{aligned} \right\} \quad (154)$$

Equation (152) contains the leading terms plus higher-order terms which are negligible for large values of kr . For large values of kr , equation (151) reduces to the form presented by Pauli (ref. 18) and given by

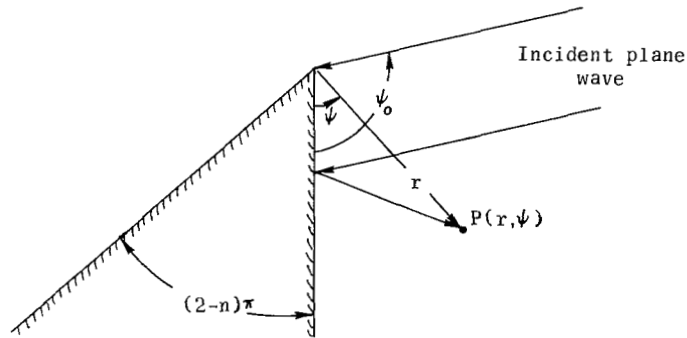
$$V_B(r, \psi_{\mp}\psi_0, n) = \frac{e^{-j\left(kr + \frac{\pi}{4}\right)}}{\sqrt{2\pi}kr} \frac{\frac{1}{n} \sin \frac{\pi}{n}}{\cos \frac{\pi}{n} - \cos \frac{\psi_{\mp} \psi_0}{n}} + \dots \quad (155)$$

The diffracted field of equation (155) is that from which the asymptotic diffraction coefficients of the geometrical theory of diffraction are obtained. (See ref. 10.) This expression is not valid in the shadow boundary because $g = 0$ there. The geometrical optics field E_G is given by equations (5) to (7).

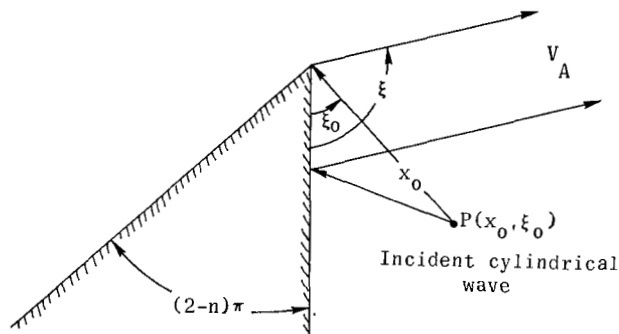
The solution for cylindrical wave diffraction at large distances from the edge can be determined by the use of the principle of reciprocity together with the solution for plane wave diffraction. (See ref. 6.) For plane wave incidence the diffracted field at

APPENDIX

observation point P of cylindrical coordinates (r, ψ) as shown in figure 35(a) is given by $V_B(r, \psi; \psi_0, n)$ of equation (151). Now consider the situation in figure 35(b) in which the wedge is illuminated by a cylindrical wave with its source at (x_0, ξ_0) . By reciprocity the diffracted field V_A in the direction ξ is equal to the diffracted field V_B which is located at the point $(r=x_0, \psi=\xi_0)$ with a plane wave incident from the direction $\psi_0 = \xi$.



(a) Incident plane waves.



(b) Incident cylindrical waves.

Figure 35.- Illustration of reciprocity.

REFERENCES

1. Silver, Samuel; and Saunders, William K.: The Radiation From a Transverse Rectangular Slot in a Circular Cylinder. *J. Appl. Phys.*, vol. 21, no. 8, Aug. 1950, pp. 745-749.
2. Bailin, L. L.: The Radiation Field Produced by a Slot in a Large Circular Cylinder. *IRE Trans. Antennas Propagation*, vol. AP-3, no. 3, July 1955, pp. 128-137.
3. Wait, J. R.: Radiation Characteristics of Axial Slots on a Conducting Cylinder. *Wireless Eng.*, vol. 32, no. 12, Dec. 1955, pp. 316-323.
4. Harrington, Roger F.: *Time-Harmonic Electromagnetic Fields*. McGraw-Hill Book Co., Inc., 1961, pp. 245-254.
5. Wait, James R.: *Electromagnetic Radiation From Cylindrical Structures*. Pergamon Press, 1959, pp. 88-104.
6. Rudduck, R. C.: Application of Wedge Diffraction to Antenna Theory. NASA CR-372, 1966.
7. Ryan, C. E., Jr.; and Rudduck, R. C.: Radiation Patterns of Rectangular Waveguides. *IEEE Trans. Antennas Propagation (Commun.)*, vol. AP-16, no. 4, July 1968, pp. 488-489.
8. Ryan, C. E., Jr.; and Rudduck, R. C.: A Wedge Diffraction Analysis of the Radiation Patterns of Parallel-Plate Waveguides. *IEEE Trans. Antennas Propagation (Commun.)*, vol. AP-16, no. 4, July 1968, pp. 490-491.
9. Rudduck, R. C.; and Yu, J. S.: Higher-Order Diffraction Concept Applied to Parallel-Plate Waveguide Patterns. Rep. 1691-16 (NASA Grant No. NsG-448), Antenna Lab., Ohio State Univ. Res. Found., Oct. 15, 1965.
10. Keller, Joseph B.: Diffraction by an Aperture. *J. Appl. Phys.*, vol. 28, no. 4, Apr. 1957, pp. 426-444.
11. Keller, Joseph B.: Geometrical Theory of Diffraction. *Opt. Soc. Amer.*, vol. 52, no. 2, Feb. 1962, pp. 116-130.
12. Franz, W.; and Deppermann, K.: Theorie der Beugung am Zylinder unter Berücksichtigung der Kriechwelle. *Ann. Phys.*, 6 Folge, Bd. 10, Heft 6-7, 1952, pp. 361-373.
13. Levy, Bertram R.; and Keller, Joseph B.: Diffraction by a Smooth Object. *Commun. Pure Appl. Math.*, vol. XII, no. 1, Feb. 1959, pp. 159-209.

14. Keller, Joseph B.; and Levy, Bertram R.: Decay Exponents and Diffraction Coefficients for Surface Waves on Surfaces of Nonconstant Curvature. IRE Trans. Antennas Propagation, vol. AP-7, Spec. Suppl., Dec. 1959, pp. S52-S61.
15. Levy, Bertram R.: Diffraction by an Elliptic Cylinder. J. Math. Mech., vol. 9, no. 2, Mar. 1960, pp. 147-165.
16. Kouyoumjian, Robert G.: Asymptotic High-Frequency Methods. Proc. IEEE, vol. 53, no. 8, Aug. 1965, pp. 864-876.
17. Sommerfeld, Arnold (Otto Laporte and Peter A. Moldauer, transl.): Optics. Academic Press, c.1954, pp. 245-265.
18. Pauli, W.: On Asymptotic Series for Functions in the Theory of Diffraction of Light. Phys. Rev., second ser., vol. 54, no. 11, Dec. 1, 1938, pp. 924-931.
19. Hutchins, David Lee: Asymptotic Series Describing the Diffraction of a Plane Wave by a Two-Dimensional Wedge of Arbitrary Angle. Ph. D. Diss., Ohio State Univ., 1967.
20. Oberhettinger, F.: On Asymptotic Series for Functions Occurring in the Theory of Diffraction of Waves by Wedges. J. Math. Phys., vol. XXXIV, no. 1, Apr. 1955, pp. 245-255.
21. Senior, T. B. A.; and Goodrich, R. F.: Scattering by a Sphere. Proc. Inst. Elec. Eng. (London), vol. III, no. 5, May 1964, pp. 907-916.
22. Hong, Soonsung: Asymptotic Theory of Diffraction by Smooth Convex Surfaces of Variable Curvature. 7741-2-T (Contract AF 04(694)-834), Univ. of Michigan, Aug. 1966. (Available from DDC as AD 804 916.)
23. Kinber, B. Ye.: Asymptotic Solution of the Problem of Diffraction by a Sphere. Telecommun. Radio Eng., no. 10 (pt. 2, vol. 21), Oct. 1966, pp. 72-80.
24. Ryan, C. E., Jr.: Memorandum on Analysis of Echo Area of Targets Using Geometrical Theory of Diffraction and Creeping Wave Theory. ESD-TR-67-519, U.S. Air Force, July 1967. (Available from DDC as AD 658 469.)
25. Peters, L., Jr.; and Ryan, C. E., Jr.: The Relation of Creeping Wave Phenomena to the Shadow-Zone Geometry. Proceeding of the GISAT II Symposium, Vol. II, Pt. I, M67-14, Mitre Corp., 1967, pp. 315-349. (Available from DDC as AD 839 700.)
26. Ryan, Charles E.: A Geometrical Theory of Diffraction Analysis of the Radar Cross Section of a Sectionally Continuous Second-Degree Surface of Revolution. ESD-TR-68-211, U.S. Air Force, Mar. 1968. (Available from DDC as AD 669 372.)

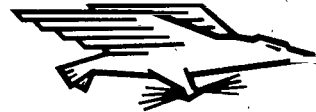
27. Kinber, B. Ye.: Short-Wave Asymptotic Diffraction of Acoustic and Electromagnetic Waves From Surfaces of Revolution. *Telecommun. Radio Eng.*, no. 4 (pt. 2, vol. 20), Apr. 1965, pp. 101-111.
28. Russo, P. M.; Rudduck, R. C.; and Peters, L., Jr.: A Method for Computing E-Plane Patterns of Horn Antennas. *IEEE Trans. Antennas Propagation*, vol. AP-13, no. 2, Mar. 1965, pp. 219-224.
29. Obha, Y.: On the Radiation Pattern of a Corner Reflector Finite in Width. *IEEE Trans. Antennas Propagation*, vol. AP-11, no. 2, Mar. 1963, pp. 127-132.
30. Dybdal, R. B.; Rudduck, R. C.; and Tsai, L. L.: Mutual Coupling Between TEM and TE₀₁ Parallel-Plate Waveguide Apertures. *IEEE Trans. Antennas Propagation*, vol. AP-14, no. 5, Sept. 1966, pp. 574-580.
31. Mikuteit, Siegfried: Mutual Coupling in a Three Element, Parallel Plate Waveguide Array by Wedge Diffraction and Surface Integration Techniques. Ph. D. Diss., Ohio State Univ., 1967.
32. Rudduck, Roger C.; and Tsai, Leonard L.: Aperture Reflection Coefficient of TEM and TE₀₁ Mode Parallel-Plate Waveguides. *IEEE Trans. Antennas Propagation*, vol. AP-16, no. 1, Jan. 1968, pp. 83-89.
33. Burnside, Walter Dennis: The Reflection Coefficient of a TEM Mode Symmetric Parallel-Plate Waveguide Illuminating a Lossless Dielectric Layer. Tech. Rep. 1691-25 (NASA Grant No. Nsg-448), ElectroSci. Lab., Ohio State Univ., May 1, 1968.
34. Jones, J. Earl; Tsai, L. L.; Rudduck, R. C.; Swift, C. T.; and Burnside, W. D.: The Admittance of a Parallel-Plate Waveguide Aperture Illuminating a Metal Sheet. *IEEE Trans. Antennas Propagation*, vol. AP-16, no. 5, Sept. 1968, pp. 528-535.
35. Kraus, John D.: *Electromagnetics*. McGraw-Hill Book Co., Inc., 1953, pp. 446-450.
36. Wu, D. C. F.; and Rudduck, R. C.: Slope Diffraction Analysis of TEM Parallel-Plate Guide Patterns. NASA CR-1326, 1969.

NATIONAL AERONAUTICS AND SPACE ADMINISTRATION

WASHINGTON, D. C. 20546

OFFICIAL BUSINESS

FIRST CLASS MAIL



POSTAGE AND FEES PAID
NATIONAL AERONAUTICS AND
SPACE ADMINISTRATION

7 0000 0000
EX-100 7117

TECHNICAL LIBRARY

POSTMASTER: If Undeliverable (Section 158
Postal Manual) Do Not Return

"The aeronautical and space activities of the United States shall be conducted so as to contribute . . . to the expansion of human knowledge of phenomena in the atmosphere and space. The Administration shall provide for the widest practicable and appropriate dissemination of information concerning its activities and the results thereof."

— NATIONAL AERONAUTICS AND SPACE ACT OF 1958

NASA SCIENTIFIC AND TECHNICAL PUBLICATIONS

TECHNICAL REPORTS: Scientific and technical information considered important, complete, and a lasting contribution to existing knowledge.

TECHNICAL NOTES: Information less broad in scope but nevertheless of importance as a contribution to existing knowledge.

TECHNICAL MEMORANDUMS: Information receiving limited distribution because of preliminary data, security classification, or other reasons.

CONTRACTOR REPORTS: Scientific and technical information generated under a NASA contract or grant and considered an important contribution to existing knowledge.

TECHNICAL TRANSLATIONS: Information published in a foreign language considered to merit NASA distribution in English.

SPECIAL PUBLICATIONS: Information derived from or of value to NASA activities. Publications include conference proceedings, monographs, data compilations, handbooks, sourcebooks, and special bibliographies.

TECHNOLOGY UTILIZATION PUBLICATIONS: Information on technology used by NASA that may be of particular interest in commercial and other non-aerospace applications. Publications include Tech Briefs, Technology Utilization Reports and Notes, and Technology Surveys.

Details on the availability of these publications may be obtained from:

SCIENTIFIC AND TECHNICAL INFORMATION DIVISION
NATIONAL AERONAUTICS AND SPACE ADMINISTRATION
Washington, D.C. 20546